Olav Ragnvaldsen

Characterisation of an aluminium matrix nanocomposite wire manufactured by screw extrusion

June 2019

Master's thesis

Master's thesis

2019

Olav Ragnvaldsen

NTNU
Norwegian University of
Science and Technology

NTNU
Norwegian University of
Science and Technology

NTNU
Norwegian University of
Science and Technology

Characterisation of an aluminium matrix nanocomposite wire manufactured by screw extrusion

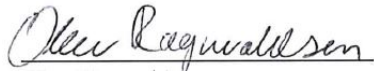## Olav Ragnvaldsen

Norwegian University of Science and Technology
Department of Materials Science and Engineering

I Preface

This master's thesis has been written from January to June 2019, based on research done at the Department of Materials Science and Engineering, NTNU.

I hereby declare that this master's thesis is written independently and in accordance with regulations at NTNU.

Olav Ragnvaldsen
NTNU, Trondheim
June 2019

II   Acknowledgements

I would like to extend my gratitude to the following persons for aiding me greatly in completing my master's thesis.

First, I would like to thank my supervisor Professor Hans Jørgen Roven (NTNU), for being available for fruitful and clarifying discussions, and providing motivation, guidance and enthusiasm to my work. I also want to thank my co-supervisor, Geir Langelandsvik (Sintef) for the extensive transfer of technical and theoretical knowledge, general encouragement and guidance through multiple experiments and preparation procedures.

I want to thank Chief Engineer Pål Christian Skaret (NTNU) for performing tensile testing and providing technical assistance when needed. I want to thank Senior Engineer Yingda Yu (NTNU) for help and guidance with electron microscopy. I also want to thank Dr. Kristian Grøtta Skorpen (Norsk Hydro) for helping with qualitative chemical analysis and answering various questions related to screw extrusion, and Dr. Nicholas Smith (Sintef) for providing literature and knowledge regarding oxidation questions.

And thank you, Ingeborg. For listening, caring and your constant support.

III   Aim

The aim of this master's thesis is to manufacture an aluminium matrix titanium carbide-nanocomposite wire by a metal continuous screw extrusion (MCSE) procedure. The intentional future use of the nanocomposite wire is as a filler wire for welding purposes, specifically for wire arc additive manufacturing. Therefore, it is required that the reinforcing nanoparticles are uniformly distributed, so that they may act as inoculants during welding to achieve grain refinement in the finished welded products. A uniform distribution of nanoparticles will also lead to isotropic mechanical properties. Additionally, to ensure structural integrity after welding, the amount of pores and oxides in the extruded wire should be minimised. To achieve this, different measures were taken both in the preparation of the feedstock material and in the processing conditions during MCSE.

A secondary objective is to investigate the correlation between the microstructure, mechanical properties and processing parameters of the extruded wires.

IV   Abstract

Metal Continuous Screw Extrusion (MCSE) is a novel solid-state manufacturing method which facilitates for the production of metal alloys and composites with new properties. MCSE is developed at the Norwegian University of Science and Technology (NTNU), in collaboration with Norsk Hydro.

In this work, MCSE was used to create two aluminium matrix composite (AMC) wires, consisting of an 5183 aluminium-magnesium (Al-Mg) alloy matrix reinforced with titanium carbide (TiC) nanoparticles. The nanoparticles had a diameter of approximately 50 nm. Two corresponding monolithic (i.e. pure 5183 Al-Mg, without TiC reinforcement particles) wires were also produced. One of the AMC wires was extruded with added carbondioxide (CO_2) gas to the screw extruder chamber, in an attempt to inhibit oxidation of Mg. The same was done for one of the monolithic wires. The pre-treatment procedure of the feedstock materials (5183 granules) was also different between the wires extruded in ambient atmosphere and the wires extruded with added CO_2, in another effort to minimise oxidation of Mg.

The microstructures of the AMC wires were investigated using Scanning Electron Microscopy (SEM). It was found that the TiC nanoparticles were uniformly distributed throughout the material, mainly appearing as small clusters. The content of TiC was fairly low in both wires. It was observed that some TiC nanoparticles agglomerated around Mg-oxide phases, implying that the TiC particles attach to surface Mg-oxides on the 5183-granules during dry coating, before MCSE.

Mechanical testing showed that the AMC wire extruded without CO_2 gas shielding (i.e. in ambient atmosphere) had the highest hardness and tensile strength. A Vickers microhardness of approximately 103 $HV_{0.1}$, yield strength of 233 MPa, tensile strength of 386 MPa and elongation of 22%EL was measured for the AMC wire extruded in ambient atmosphere. The AMC-wire extruded in a CO_2 rich atmosphere had a Vickers microhardness of approximately 95 $HV_{0.1}$, yield strength of 198 MPa, tensile strength of 374 MPa and an elongation of 23%EL. No significant differences in strength or hardness were observed between the two monolithic wires. Thus, it is assumed that the inferior mechanical properties of the AMC wire extruded in the presence of CO_2 gas is due to an unintentional lower TiC content. The ductility of the monolithic wire increased by 6 percentage points when CO_2 cover gas was applied. This is attributed to the inhibited formation of brittle Mg-oxides.

Additionally, it was observed that strain hardening slightly increased during tensile testing for the wires extruded with CO_2 cover gas. The underlying mechanism is assumed to be an increase of Mg content in solid solution, when applying the CO_2 cover gas, which reduces the amount of Mg-oxides formed. The addition of TiC nanoparticles had a negative effect on strain hardening. This might be explained by a significant interparticle spacing between the TiC nanoparticles, hence resulting in large spacing between the dislocation generating Frank-Read sources.

The intended future application for the AMC products are as welding wires in Wire Arc Additive Manufacturing (WAAM). Therfore, it is required that the amount of pores and oxides present in the extruded AMC-wires is minimised.

V   Samandrag

Kontinuerleg skrueekstrusjon av metaller (Metal Continuous Scew Extrusion, MCSE) er ein nyutvikla, fast tilstands produksjonsmetode, som tilrettelegg for framstilling av metallegeringar og komposittar med nye eigenskapar. MCSE er utvikla ved Noregs Teknisk-Naturvitskaplege Universitet (NTNU), i samarbeid med Norsk Hydro.

I denne oppgåva har MCSE blitt brukt til å produsere to aluminium-matrise kompositt (aluminium matrix composites, AMC) trådar, beståande av ei 5183 aluminium-magnesium (Al-Mg) legering som matrise, forsterka med titankarbid (TiC) nanopartiklar. Diameteren til naopartiklane var omtrent 50 nm. To tilsvarande trådar av reint 5183 Al-Mg, det vil seie utan TiC nanopartiklar, vart også produserte på same måte. Ein av AMC-trådane vart ekstrudert med tilsett karbondioksid (CO_2) gass under ekstrudering, i eit forsøk på å motverke oksidasjon av Mg. Det same vart gjort for ein av dei reine 5183-trådane. Rensinga av råmaterialet (5183 granular) vart også tilpassa for å minimere oksidasjon.

Mikrostrukturen til dei produserte AMC-trådane vart undersøkt ved hjelp av eit Scanning Elektron Mikroskop (SEM). Desse undersøkingane viste at TiC nanopartiklane var uniformt fordelte i materialet, hovudsakleg i form av små klyngar. TiC innhaldet i begge trådane var relativt lågt. Nokre av TiC nanopartiklane omkransa Mg-oksid. Dette kan tyde på at TiC partiklar har festa seg til Mg-oksida på overflaten av 5183-granulane under "tørr-coating", før MCSE vart iverksett.

Mekanisk testing viste at AMC-tråden som vart ekstrudert utan bruk av CO_2 gass, altså i luft, hadde høgast hardhet og styrke. Vickers mikrohardhet for denne tråden vart målt til omtrent 103 $HV_{0.1}$, flytespenning til 233 MPa, strekkfasthet til 386 MPa og forlenging til 22%EL. For AMC-tråden som vart ekstrudert i CO_2-rik atmosphere vart det målt Vickers mikrohardet på omtrent 95 $HV_{0.1}$, flytespenning på 198 MPa, strekkfasthet på 374 MPa og forlenging på 23%EL. Dei to reine 5183-trådane hadde omtrent like verdiar for styrke og hardhet. Difor er det antatt at den svakare styrkeaukninga for tråden ekstrudert i CO_2-rik atmosfære, samanlikna med tråden som vart ekstrudert i luft, skuldast eit utilsikta, lågare innhald av TiC nanopartiklar. Duktiliteten for dei reine 5183-trådane auka med 6 prosent poeng når CO_2 gass vart tilført under ekstrudering. Det er antatt at auka i duktilitet skuldast at CO_2 gassen reduserte danninga av sprø Mg-oksid.

Det vart også observert at arbeidsherdinga auka svakt under strekktesting for trådane som vart ekstruderte i CO_2-rik atmosfære. Det er antatt at dette skuldast ei auke i Mg-innhaldet i fast løysing, forårsaka av at CO_2 forhindra danninga av Mg-oksid. TiC nanopartiklane hadde negativ innverknad på arbeidsherdinga til AMC-trådane. Det kan forklarast ved å anta at den betydelege avstanden som vart observert mellom TiC nanopartiklane førte til stor avstand mellom dislokasjonane som vart danna under strekktesting. Dette førte til redusert arbeidsherding. Altså, kan det antakast at TiC nanopartiklane har opptredd som Frank-Read sources, med stor avstand seg i mellom.

Det tiltenkte bruksområdet for dei produserte AMC-trådane er som sveisetrådar i additiv tilverkning. Difor må innhaldet av porer og oksider i dei ferdige trådane haldast på eit minimum.

Contents

1   Introduction

The rapid development within transport, defence industries, space exploration and marine applications requires stronger and lighter materials. In many cases a combination of structural integrity, high strength, resistance against corrosion and wear is sought, combined with low weight and low cost. A promising material class capable of fulfilling these requirements are the aluminium matrix composites (AMCs). AMCs consist of aluminium alloys reinforced with hard (often non-metallic, ceramic) particles or fibres. These materials are intensively researched and continuously developed, as they are of vital importance within multiple engineering industries. Using AMCs for e.g. aerospace and automotive parts improves fuel efficiency and thus reduces the emissions of greenhouse gases [1].

An obstacle for industry-wide application of AMCs, are the energy demanding, complicated and expensive production methods. These often involve melting the unreinforced alloy and then adding the reinforcement particles in the molten metal, or by sintering metallic and ceramic powders [2]. A common challenge in the production of AMCs is to obtain a uniform distribution of the reinforcement particles. This is only obtained to a varying degree for some of the conventional production methods. Additionally, unwanted reaction frequently occur between the matrix and the reinforcement particles in the production methods involving molten aluminium [3][4][5].

A novel method for the production of AMCs is metal continuous screw extrusion (MCSE), developed at **NTNU** (Norwegian University of Science and Technology), in cooperation with **Norsk Hydro**. This solid-state production process provides promising results in the manufacturing of extruded products with unique properties, and has the ability to use various different aluminium materials as feedstock [6][7][8].

An emerging technology predicted to radically change today's manufacturing industries, is the additive manufacturing (AM) of materials. Among the benefits of AM, compared to traditional manufacturing methods, is increased design freedom, a wide variation of processable material types, the ability to produce highly complex and customised parts, and shorter time to market for new designs [9][10]. To further develop new AM-material with high strength and structural integrity, new raw-materials are needed.

2 Litterature review

2.1 Aluminium and its alloys

Aluminium (Al) is the third most abundant element and the most abundant metal in the Earth's crust. Due to the useful inherent properties of aluminium, such as low density ($2.7 \ \mathrm{g\,cm^{-3}}$ vs. $7.9 \ \mathrm{g\,cm^{-3}}$ for steel [11]), good thermal and electrical conductivity, and corrosion-resistance in common environments, aluminium is being produced and applied at a large scale. The main drawback for the use of Al is considered to be the low melting temperature at 660°C [11].

The most common production process for primary Al production today is the electrochemical *Hall-Hèroult* process, in which alumina (Al_2O_3), dissolved in molten cryolite (Na_3AlF_6), is carbothermically reduced to Al on the cathode. Carbon dioxide (CO_2) is produced through consumption of the carbon-anode [12].

More than 60 million tonnes of primary Al is manufactured annually. Figure 1 shows the total tonnage of primary Al manufactured in 2018, as well as the amount produced in different parts of the world (given in thousand metric tonnes) [13].
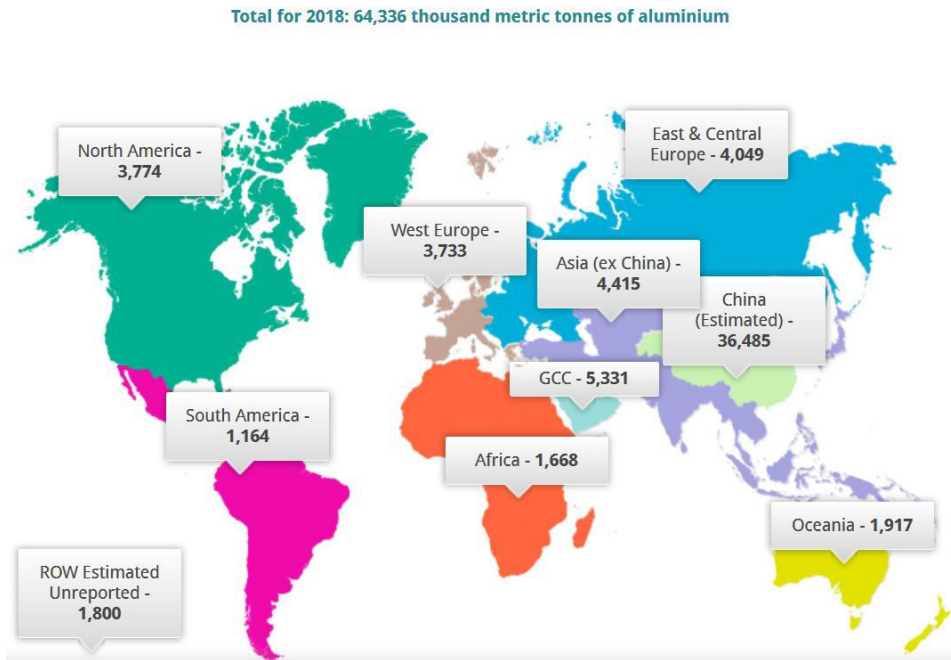

Figure 1: Map showing total primary aluminium global production for 2018. The production numbers for the different geographical sections are given in thousand metric tonnes. From [13].

Al has a face-centred cubic (fcc) crystal structure, in which the internal resistance to dislocation-movement is small [14]. Therefore, pure Al is ductile even at

low temperatures. This facilitates for the use of mechanical processing methods such as rolling, extrusion and drawing, to shape a finished Al-product [11]. The slip plane in the Al fcc crystal structures is the {111} plane and the slip direction is <110>, resulting in 12 different slip systems [11].

The low resistance to dislocation-movement in commercially pure Al (99.5%-99.8% [15]) restrict its uses to packaging and electronics. When high strength or stiffness is required, defects are intentionally introduced into the material either through addition of *alloying elements* or by *cold work* (plastic deformation at ambient temperatures). These defects will hinder the propagation of dislocations induced by external loads, resulting in a mechanically stronger material. The most common alloying elements in Al-alloys include copper, manganese, silicon, magnesium and zinc [14].

Aluminium alloys are designated either as *wrought* or *cast* alloys. Wrought alloys are formed mechanically into the desired shaped by drawing, rolling, extrusion or forging to induce plastic deformation in the materials. This leads to strengthening of the alloy through *strain hardening*. Wrought alloys contain relatively small amounts of alloying elements to ensure low resistance towards plastic deformation, as well as high ductility [14].

Cast alloys are required to have a short solidifying interval and flow smoothly, so that casting conditions are optimal. The only strengthening contribution in cast alloys come from the alloying elements. A combination of high strength and suitability for casting is therefore achieved by adding large (near *eutectic*) amounts of alloying elements to the Al-melt before casting [14].

Both types of alloys may be further differentiated based on the possibility of heat-treating the alloy to achieve higher strength. Strengthening by heat-treating occurs due to the introduction of strengthening phases/particles, occurring as a consequence of thermal treatments, such as quenching, precipitation, solution heat treatment or age hardening. The introduced phases/particles need to be *coherent* (i.e. have continuous atomic-planes across the matrix-phase boundary) to the Al-matrix in order to strengthen the alloy. If the phases/particles are not coherent to the matrix, they might decrease the strength of the alloy. The alloys in which the precipitated phases are densely distributed and contribute to increased strength are known as "Heat-treatable" alloys [14]. If the precipitation occurs to a small degree or if the precipitated phases lead to a decrease in strength, the alloy is "Non-heat-treatable" [16].

Aluminium alloys are classified based on composition by the *American nomenclature*. This designation uses 4 digits for *wrought*-alloys and 3 digits for *cast*-alloys. The first digit indicates the predominant alloying elements as shown in Table 1. The second digit indicates the number of modifications made to the original alloy. So a 3 as the second digit means that this alloy is the third modification of the original alloy, which has a 0 as the second digit. For pure Al (1xxx-series), the two last digits indicates the minimum purity above 99 % Al (so that 43 means minimum 99.43 % Al). For other alloys, the last digits are numbers identifying the specific alloy [14].

Table 1: Classification of aluminium alloys based on the predominant alloying element [17].

Wrought alloys		Cast alloys	
Principal alloying element	Series	Principal alloying element	Series
None (min. 99% Al)	1xxx	None (min. 99% Al)	1xx
Copper	2xxx	Copper	2xx
Manganese	3xxx	Silicon (+copper/magnesium)	3xx
Silicon	4xxx	Silicon	4xx
Magnesium	5xxx	Magnesium	5xx
Magnesium and silicon	6xxx	Unused series	6xx
Zinc	7xxx	Zinc	7xx
Other elements	8xxx	Tin	8xx
Unused series	9xxx	Other elements	9xx

2.1.1 Aluminium-magnesium alloys

Aluminium alloys where magnesium (Mg) is the primary alloying element are designated as 5xxx-alloys, as shown in Table 1. Al-Mg alloys exhibit strong strain-hardening properties, but are not strengthened when subjected to thermal treatment. Thus, Al-Mg alloys are classified as wrought, non-heat treatable alloys [16]. Mg has a density of only $1.7\,\mathrm{g\,cm^{-3}}$, is a relatively cheap alloying element ($\sim$2.2\$/kg vs $\sim$5.9\$/kg for copper [18]) and has a hexagonal close packed (HCP) crystal structure [11]. Alloying Al with Mg results in light and inexpensive alloys, with high *specific* strength (strength to density ratio).

Al-Mg alloys are ductile, exhibiting around 20% elongation (%EL) when homogenised, and show ultimate tensile strengths (σ_{UTS}) between 180 and 300 MPa [14]. Adding Mg to Al reduces the *stacking fault energy*, i.e. the energy increase of introducing a stacking fault in a perfect fcc crystal. This restricts the mobility of the dislocations in the alloy [19].

As seen from the Al-Mg phase diagram in Figure 2, up to 18.9 wt% Mg may be dissolved in Al (at 450°C) to form a solid solution [20]. However, commercial 5xxx-alloys usually do not contain more than 5 wt% Mg, in order to avoid the formation of the brittle β-phase at the grain boundaries. The exact stoichiometry of the β-phase is debated, both Al_3Mg_2 and Al_8Mg_5 are used in literature. In addition to being brittle, the β-phase is anodic (active) relative to the Al-Mg matrix, so both mechanical and corrosion properties worsen with the precipitation of these phases [14].
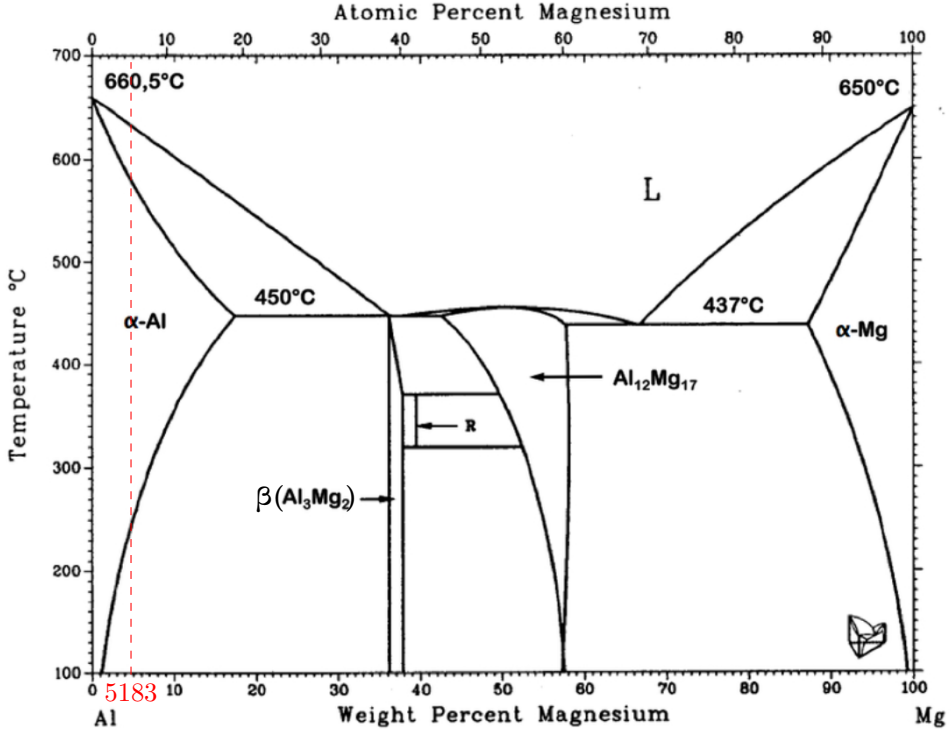
Figure 2: Al-Mg phase diagram, adapted from [20]. The dashed, red line corresponds to the Mg-content of a 5183 Al alloy (≈ 4.5 wt%).

Mg atoms in solid solution contribute to both *solid solution hardening* and *strain hardening* in 5xxx-alloys. Solid solution hardening occurs due to the larger size of the Mg atoms, relative to Al, which induce stress fields in the surrounding matrix. These stress fields will hinder the propagation of dislocations, so that the strength of the alloy is increased [11].

Strain hardening is a consequence of the stress fields forming around dislocations induced to the material under external loads (i.e. plastic deformation). The stress fields in the matrix around these dislocations will (on average) be repulsive towards the propagation of other dislocations, so that the material is strengthened under plastic deformation [11]. The increase in strength, $\Delta\sigma$ due to strain hardening at a certain strain ϵ, may be written as [21]:

$$\Delta\sigma = \sigma_Y \left(\frac{\epsilon}{\epsilon_Y} \right)^n \tag{1}$$

where σ_Y is the yield strength of the alloy, ϵ_Y is the yield strain and n is the strain hardening exponent (around 0.1 for 5183 alloys, depending on mechanical processing [21]). Strain hardening and solid solution strengthening increases with the Mg-content of Mg in Al-Mg alloys [22][23].

6

Manganese (Mn) is often added to Al-Mg alloys to control recovery and recrystallisation. Mn is not solved in the Al-Mg matrix but forms complex precipitates, which may act as nucleation sites for recrystallisation and pin the grain boundaries. These precipitates will also induce point defects in the material which hinder dislocation-movement, and thus increase the strength of the alloy [21][23].

In this work, a 5183 Al-Mg alloy is investigated. A dashed, vertical red line corresponding to the Mg-content in this alloy (≈ 4.5 wt%) is inserted in the phase diagram in Figure 2.

2.2 Portevin-Le Chatelier effect

An interesting phenomenon which may occur when Al-Mg alloys are strained (e,g in a tensile test), is the Portevin-Le Chatelier (PLC) effect [24]. This behaviour, first reported by Portevin and Le Chatelier [25], is not exclusive to Al-Mg systems, but also occurs in other important industry materials like other aluminium alloys (e.g. Al-Cu) and steels [26].

The PLC effect is a consequence of the interactions between mobile solute atoms (like Mg) and dislocations in the (Al-)matrix. Dislocations present in the material will induce an elastic strain energy field in the surrounding lattice. If energetically favourable, the solute atoms will diffuse to the dislocation core, reduce the elastic strain energy and form clusters. These clusters create a drag force which hinders the further movement of the dislocation [21]. Thus, the alloy is strengthened, as the stress necessary for the dislocation to break the cluster and propagate is increased. When this new stress limit is reached, the cluster is broken and Mg atoms will then again diffuse to the tip of the dislocation. This results in another instance of strengthening.

The diffusion of solute atoms from the surrounding solid solution matrix to a dislocation requires a finite time to create the strengthening atomic clusters. This creates a fluctuation in the required stress for propagation of the dislocation, which is lower when no cluster is at the dislocation core and higher when the cluster is present. These dynamic interactions between the Mg atoms in solid solution and the dislocations are termed dynamic strain ageing (DSA)[27], and results in serrated stress-strain curves. The grey stress-strain curve in Figure 3 displays typical serrated PLC behaviour in a low carbon steel at elevated temperatures. The black curve in the same figure shows that PLC effect does not occur for the same steel at ambient temperatures [28].
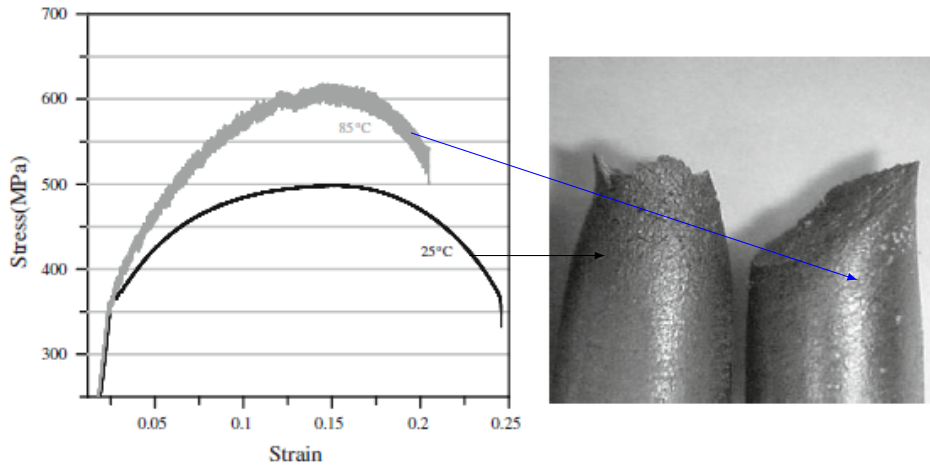
Figure 3: Left: Tensile curves of low carbon steel at different temperatures, showcasing the temperature dependence on the onset of PLC behaviour. The upper, grey curve shows the serrated stress caused by the PLC effect. Right: Tensile samples from the same experiment. The left sample (tested at 25°C) has a typical ductile fracture appearance, the right sample (tested at 85°C) indicates a brittle fracture. From [28].

Figure 3 illustrates that the testing temperature affects the serrated flow. If the temperature is too low (which is the case for the black tensile curve), there is not enough energy present for the diffusion in the DSA mechanism to take place. Figure 3 also shows that materials showing PLC behaviour are more brittle. Therefore, PLC behaviour is an unwanted effect for most materials, as brittle fractures may result in catastrophic failures.

Another parameter determining the occurrence of PLC behaviour, in addition to temperature, is the *strain rate* ($\dot{\epsilon}$) during the tensile test. Figure 4 shows the temperature and strain rate ranges where PLC (serrated flow) occurs for a 5083 Al alloy [29].
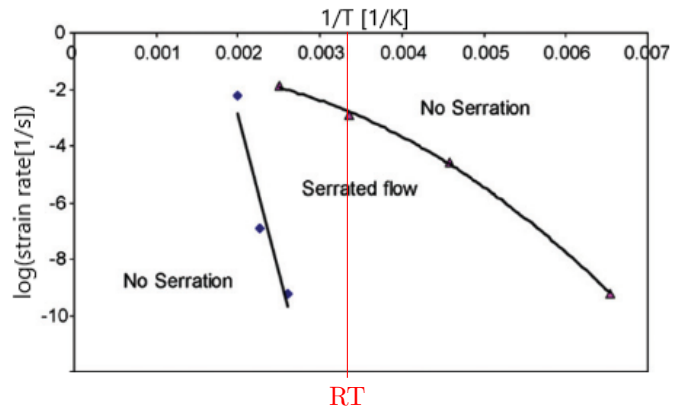
Figure 4: Strain rate and temperature regions in which DSA (and thus serrated flow; PLC) occurs for a 5083 Al-Mg alloy. The inserted, red line corresponds to room temperature (298 K). Adapted from [29].

From Figure 4 it may be seen that to achieve PLC behaviour in a 5083 alloy at room temperature, the logarithmic strain rate should be lower than 10^{-3} s^{-1}.

2.3 Oxidation of Al-Mg alloys

The corrosion properties of pure Al are generally improved when Al is alloyed with Mg. Mg increases the stability of the protective Al_2O_3 oxide film formed on the surface of Al alloys, so that the corrosion resistance in alkaline environments (e.g. marine environments) is enhanced [14]. However, under certain processing conditions (e.g. at elevated temperatures), the oxidation of Al-Mg alloys may become problematic.

A model for the oxidation mechanism of **solid** Al-Mg alloys has been suggested by Wefers [30]. The model is based on gravimetric, microscopic and diffraction analyses of thin Al-Mg flakes, isothermally heated in dry air conditions. A schematic sketch for the suggested mechanism, along with the oxide-thickness evolution (copied with permission from [31], redrawn from [32]) is included in Figure 5.
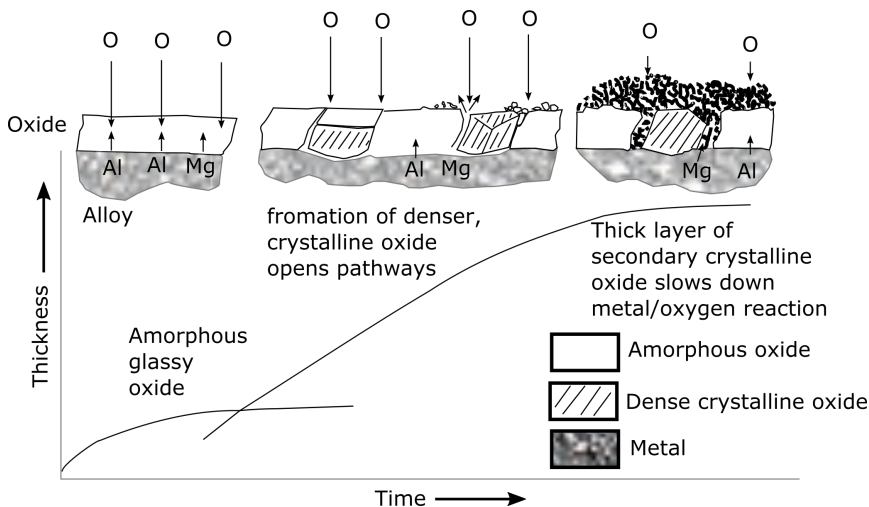

Figure 5: Schematic sketch of the oxidation mechanism and oxide thickness evolution for solid Al-Mg alloys, at a constant temperature above 400°C. Copied with permission from [31], redrawn from [32].

Initially, as for all Al-alloys, an amorphous Al_2O_3 oxide layer is present at the Al-Mg alloy surface, as illustrated in the top left drawing. The oxidation rate at this point is low, and controlled by the diffusion of species through the amorphous layer. This results in a parabolic oxidation rate converging towards a limiting oxide thickness. After heating above 400°C for a certain time period, denser, crystalline oxides occur at the interface between the amorphous oxide layer and the metal, as shown in the top middle drawing. This further leads to cracking in the amorphous layer, creating open pathway channels to the underlying Al-Mg alloy. The oxidation rate increases and the oxide thickness-time curve in Figure 5 changes from parabolic to linear. Now, secondary Mg-oxides are formed in the air-metal-oxide interfaces. These secondary Mg-oxides eventually cover the surface and pathways, as shown in the top right drawing, reducing the oxidation rate. Wefers [30] observed that if the

Al-Mg alloy contains more than 2 to 3 % Mg, Mg will diffuse (preferentially to Al) to the oxide/air interface in the open channels, at temperatures over ≈ 300°C. This results in a duplex film of aluminium oxide adjacent to the metal, and Mg-oxide (MgO or $MgAl_2O_4$) particles are formed on the alloy-surface, as seen to the top right in Figure 5. The formation of Mg-oxides reduces the Mg content in solid solution in the Al-Mg alloy.

The mass gain per area over time, attributed to the formation of oxides, for a 6010 alloy at different holding temperatures in dry air atmosphere is included in Figure 6 [30].
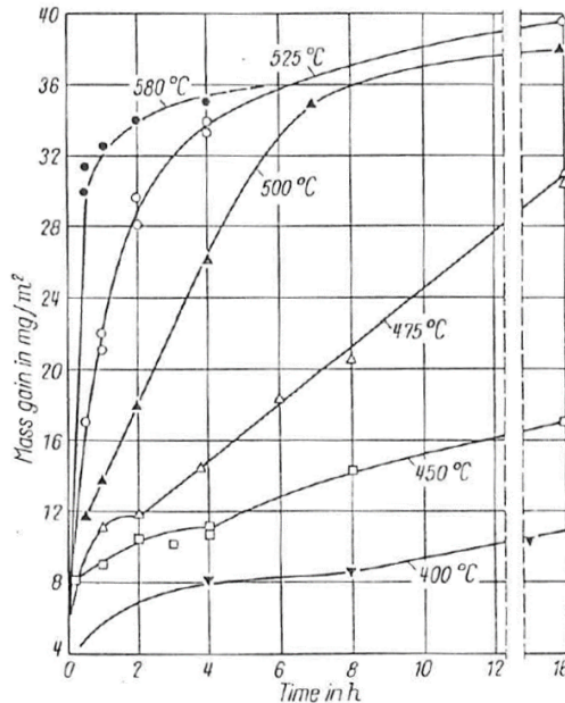

Figure 6: Mass gain per area of an 6010 Al-Mg-Si alloy during oxidation in dry air, at various temperatures. From [30].

From Figure 6 it may be observed that the mass gain per area is increasing rapidly with increasing temperatures.

Lea and Ball [33] confirmed that in solid Al-Mg alloys held at elevated temperatures (350–600°C, i.e. in the alloys common fabrication temperature range), Mg will diffuse from the bulk material to the surface, so that the bulk material is depleted of Mg. If the alloy is heated in vacuum, Mg evaporates from the surface. If it is heated in air, an Mg-rich oxide (MgO or $MgAl_2O_4$) forms at the surface, preferentially to Al_2O_3, due to a lower Gibbs free energy change for the reactions producing Mg-oxides [34].

In short, the formation of Mg-rich oxides will deteriorate the surface properties

(corrosion resistance, wear etc.) of the alloy and is therefore unwanted. The Mg-content in solid solution will also be reduced, leading to decreased solid solution strengthening and strain hardening [23]. Therefore, prolonged exposure to elevated temperatures during production of Al-Mg alloys should be avoided when possible. Dry air storage at 60°C was found to have no significant effect on the formation of Mg-oxides [33].

Historically, the most used method to avoid oxidation during *casting* of Al-Mg melts has been to add small amounts of beryllium (Be) to the alloy melt. Working with Be involves serious health risks (lung and skin diseases) [35]. Therefore, other methods of oxidation inhibition are needed. A summary of different inhibition methods to prolong the breakaway oxidation of **molten** Al-Mg alloys is included in Figure 7 [36].
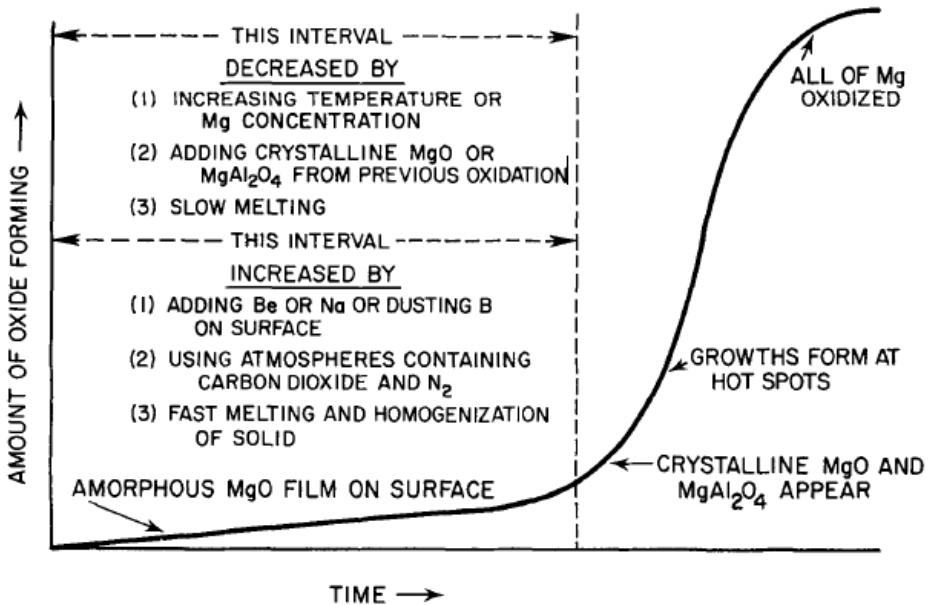

Figure 7: General curve for the formation of oxides during casting in **molten** Al-Mg alloys, showing the sudden increase in the amount of oxides after breakaway oxidation. Different factors which decrease/prolong the time before breakaway oxidation are included. From [36].

As shown in Figure 7, using an atmosphere containing carbon dioxide (CO_2) may increase the time before excessive oxidation of the Al-Mg alloy occurs. A graph of the required percentage of CO_2 (in terms of partial pressures to air) in the atmosphere to achieve this delayed breakaway oxidation condition, as a function of Mg content for Al-Mg **melts** is shown in Figure 8 [36].
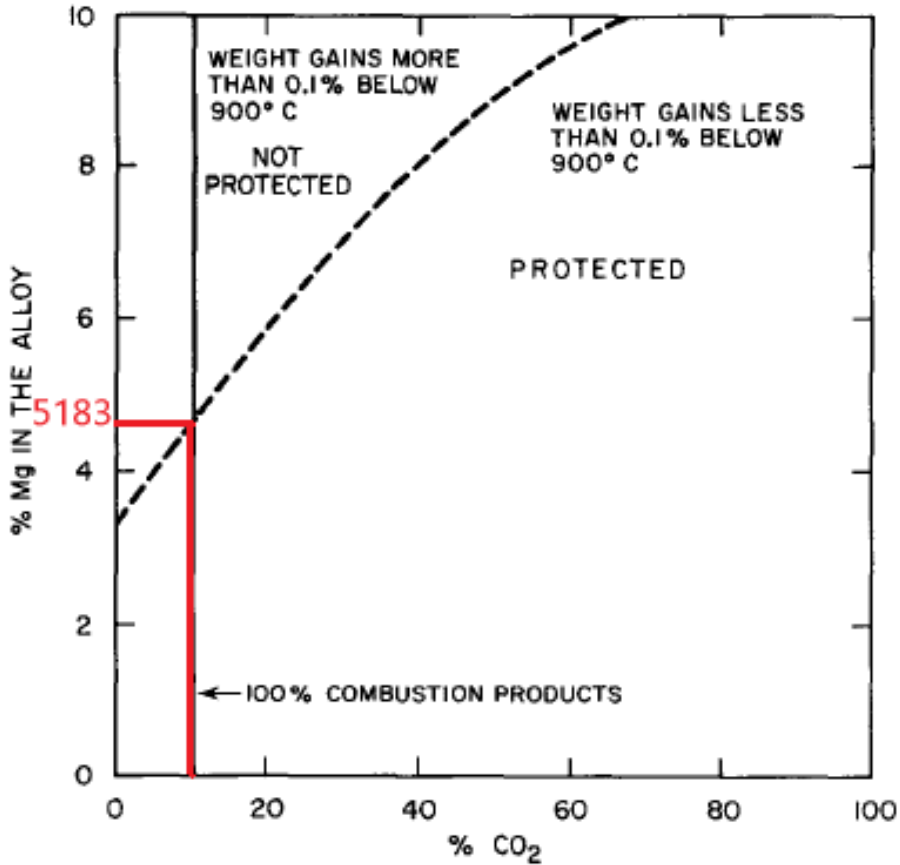

Figure 8: Recuired content of CO_2 in the casting atmosphere, to avoid excessive oxidation of **molten** Al-Mg. The inserted red line corresponds to the Mg-content (4.5 wt%) in the 5183 Al-alloy used in this work. From [36].

The inserted red line in Figure 8 at $\sim$4.5wt%Mg (corresponding to a 5183 Al-Mg alloy), shows that a casting-atmosphere of at least 10 % CO_2 is needed to protect a 5183 alloy against oxidation during casting.

The use of CO_2 gas as an oxidation inhibitor for Al-Mg melts has been further investigated by Nicholas Smith in his PhD thesis *Methods of Oxidation Inhibition for Al-Mg alloys* [31]. This thesis confirmed that oxidation of molten Al-Mg alloys at elevated temperatures may be reduced by applying a CO_2 rich atmosphere (5-50

13

% CO_2) during casting. The proposed mechanism is that CO_2 acts as an oxidation inhibitor by diffusing from the atmosphere and inwards in the MgO oxide layer, which is formed at the alloy surface. The oxide layer continues to grow around the CO_2 molecules, resulting in decreased oxygen partial pressure. CO_2 then further reacts with Mg and forms a Mg-O-C phase, structurally different from the MgO phase formed in ambient atmospheres. The carbon-rich granular oxide layer will act as a protective "cap" at the surface, slowing down further out-diffusion of Mg. Smith et al. found that even a small presence of CO_2 (5% to air, in terms of partial pressures) decreased oxidation significantly [37].

It is assumed that the same principles are transferable to the oxidation of **solid** Al-Mg alloys.

2.4 Composite materials

By combining different materials, unique and tailored products may be manufactured. Artificially made materials of different phases with distinct properties are known as *composites*. In most cases, composites consists of two phases; a continuous (ductile) *matrix* phase, surrounding a discrete reinforcing (hard) *dispersed phase*. The resulting characteristics of the composite is usually given by the properties of the matrix, the dispersed *reinforcement* phase and the amounts of each phase. Usually, the mechanical properties will lie in between the inherent values of the parent materials [11].

Composites are classified either based on the characteristics of the dispersed reinforcement phase or of the matrix material, as shown in Figure 9.
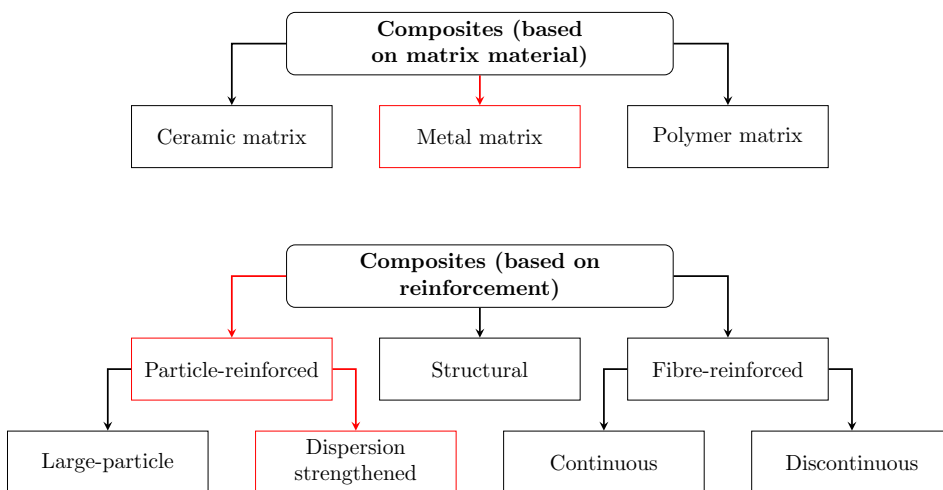

Figure 9: Classification of composites, based on matrix material (top) or reinforcement (bottom). The red boxes and arrows indicate the composites of interest in this thesis.

The composites classes of interest in this thesis are the *particle-reinforced metal matrix composites* (MMCs), indicated with red boxes and arrows in Figure 9. Common matrix materials for MMCs are copper, aluminium, titanium, magnesium and superalloys [11]. Particle reinforced matrix composites exhibit strong creep and fatigue resistance, as well as increased tensile/yield stress compared to their *monolithic* (pure matrix) alloys. The strain hardening rate in particle reinforced MMCs has been found to be larger than in comparable monolithic alloys, and to increase with the weight fraction of reinforcement particles [38]. However, Chawla and Shen [39] argue that this is mainly a consequence of the lower matrix volume achieved by the addition of reinforcement particles, and not necessarily due to an improvement in strain hardening properties from the addition of ceramic reinforcement particles.

As shown in Figure 9, particle-reinforced composites may further be divided into two groups; *Dispersion strengthened* and *Large Particle* composites, based on the nature of the matrix-particle interactions.

Dispersion strengthened composites contain small reinforcement particles (diameters between 10 and 100 nm). The particle-matrix interactions may be described on the atomic or molecular level. The small particles introduce compressive strains in the matrix phase, similar to the mechanism of *precipitation hardening* known to occur in many common metallic alloys (e.g. in the 2xxx and 6xxx series of Al alloys) [11].
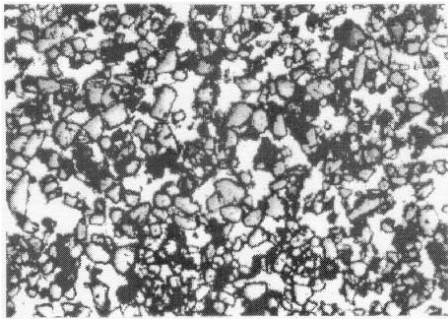
Large Particle composites are reinforced with particles of a diameter larger than $100\,\mathrm{nm}$. For large-particle composites, continuum mechanics are used to describe the particle-matrix interactions. The reinforcing particles hinder the movement of the matrix phase and thus makes the composite material stiffer and stronger than the matrix itself [11].

In all particle reinforced composites, a uniform distribution of the particles is a crucial requirement for obtaining sufficient structural integrity, and for exploiting their full strengthening potential [2]. A large volume fraction of the reinforcement phase results in a brittle, but hard material (ceramic-like properties), while a low volume fraction gives a ductile and soft material (matrix-like properties). If the particles agglomerate, the mechanical properties will vary throughout the material. Some parts will be brittle, some will be ductile, depending on the distribution of the reinforcement particles [39]. Additionally, if the particles are to be used as nucleation sites for *heterogeneous nucleation* (discussed in subsection 2.6), a uniform distribution is required to obtain fine, equiaxed grains in the material after solidification [40].

A popular class of metal matrix composites are the **aluminium matrix composites (AMCs)**. AMCs are interesting for several applications due to their low weight/strength ratio compared to commercial aluminium alloys, and low cost and weight compared to other metal matrix composites. AMCs may be tailored to fit various purposes within different engineering sectors [1].

The reinforcing phases in AMCs are usually ceramics, such as silicon carbide (SiC), titanium carbide (TiC) or alumina (Al_2O_3), with a volume fraction corresponding to the desired properties of the AMC. Based on the geometry of the reinforcing phase, AMCs may be classified into the following four groups; Particle-

reinforced AMCs, Whisker- or short fibre-reinforced AMCs, Continuous fibre-reinforced AMCs or Mono filament-reinforced AMCs. Composites with more than one type of reinforcement are known as Hybrid AMCs [1]. Images of AMCs reinforced with different reinforcement types are shown in Figure 10 [1].
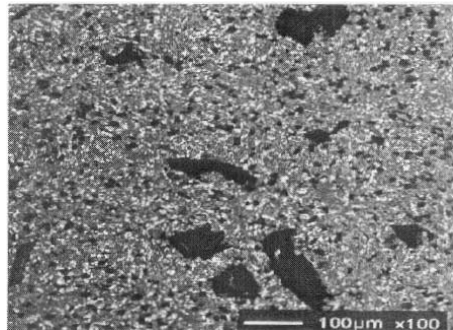

(a) Particle-reinforced cast aluminium matrix composite, with a 40 vol% SiC.
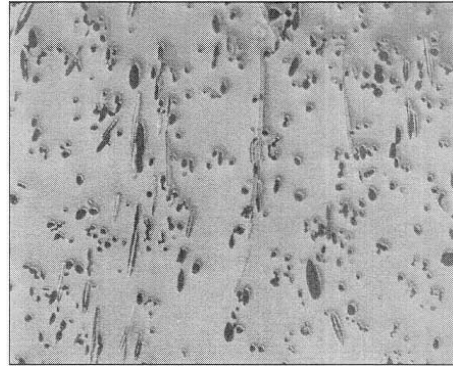
(b) Short fibre-reinforced aluminium matrix composite.
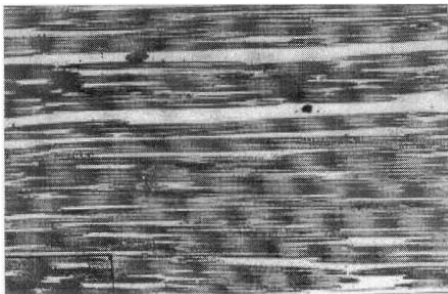
(c) Aluminium matrix composite reinforced with continuous Al_2O_3 fibres.

(d) Hybrid aluminium matrix composite, with 10 vol% SiC particles and 4 vol% larger graphite particles.

Figure 10: Optical microscopy images showing the microstructures of aluminium matrix composites with different types of reinforcement. Information on the percentage of reinforcement in (b) and (c), and the reinforcement material in (b) was not given in the reference [1]. The scale bar in image (d) may be used for all images. The Al matrix is the white phase, while the reinforcement phases are seen as dark particles or fibres. From [1].

Reinforcing an aluminium alloy with uniformly distributed ceramic particles produces an AMC with higher density, hardness, compressive strength and toughness, compared with the *monolithic* (unreinforced) alloy. Porosity should be avoided, as it may adversely affect the material properties. Tensile and flexural strength of the composite will scale with the fraction of ceramic particles added, but only up

to a certain amount. Exceeding this threshold leads to lower tensile and flexural strength [41].

Due to their excellent mechanical, tribological and corrosion properties, AMCs are being extensively researched and are replacing their corresponding monolithic alloys in the automobile, aviation and marine industry [1].

In this work, an AMC consisting of a 5183 Al-Mg matrix reinforced with TiC nanoparticles (with a diameter of approximately 50 nm) was manufactured and investigated.

2.5 Strengthening mechanisms in nanoparticle reinforced AMCs

In general, the strength of a material is viewed as its ability to restrict the movement of dislocations induced in the material under external loads. Strength is commonly determined by performing tensile tests on standard specimen samples. The strength is often given as either ultimate tensile strength (σ_{UTS}) or yield strength (σ_Y). σ_{UTS} is the largest tensile stress (load per area, unit: MPa = $\mathrm{N\,mm^{-2}}$) endured by the material during tensile testing. σ_Y is the stress required to induce plastic (irreversible) deformation in the material [11]. To increase the strength of a material, i.e. to increase the resistance against dislocation movement by slip, different approaches may be taken.

A well-known strengthening mechanism in polycrystalline materials is strengthening by grain size reduction. Grains usually have different crystallographic orientations and will therefore force a propagating dislocation to change its direction of motion. The smaller the grains, the more frequently a dislocation will be hindered. Grains will also impose atomic disorder around the grain boundary region, which results in a discontinuity of slip planes between the grains. These two effects will hinder the movement of dislocations in the material, and thus increase its strength. The relationship between yield strength and grain size is for most metals given by the Hall-Petch relationship [11]:

$$\sigma_Y = \sigma_0 + k\frac{1}{\sqrt{d}} \tag{2}$$

where σ_0 the lattice friction stress, k is the Hall-Petch coefficient given for the material and d is the average grain diameter.

When the size of the grains in a material decreases, its yield strength and toughness will increase [11]. If the grains are small, the total grain boundary area will be large and the dislocations will be hindered to a larger extent. The increase in yield strength due to grain refinement ($\Delta\sigma_{GR}$) can be written as:

$$\Delta\sigma_{GR} = k\frac{1}{\sqrt{d}} \tag{3}$$

Ceramic nanoparticles may act as *inoculants* during casting or welding of particle reinforced AMCs, during the solidification of molten Al. TiC reinforcement particles have been shown to produce fine grain sizes through *heterogeneous inoculation* (discussed in subsection 2.6) in several experiments [42][43][44]. The fine grain struc-

ture achieved after solidification will increase the yield strength of the composite, as according to Equation 3.

An additional mechanism for grain refinement in particle reinforced AMCs is *Zener pinning*. In *Zener Pinning*, second phase particles (e.g. ceramic nanoparticles) situated on the grain boundaries hinder grain growth at elevated temperatures by exerting a *Zener drag* against the movement of the grain boundaries [45]. Zener pinning results in an upper limit for the diameter of the solidified grains, d_Z, given by the *Zener equation* [46]:

$$d_Z = \frac{4\gamma d_p}{3V_p} \tag{4}$$

Where γ is a proportional constant, d_p is the average reinforcement particle diameter and V_p is the volume fraction of reinforcement particles. From Equation 4 it may be observed that the smaller the reinforcement particles are, the smaller will the resulting grain size. Nanosized particles are therefore ideal to achieve a large strengthening contribution from grain size reduction (through Zener pinning).

The different properties of the phases present in composites will also affect the yield strength. The matrix phase and the reinforcing phase will have unique coefficients of thermal expansion (CTE, unit: K^{-1}). When cooled from elevated temperatures, the different phases will contract to a varying degree based on the magnitude of their inherent CTE. This "thermal mismatch" will result in residual plastic strain, which increases dislocation density around the reinforcement particles. If the material is cooled rapidly (i.e. quenched), the dislocations will remain around the ceramic particles when the material reaches ambient temperatures. The increase in yield strength due to CTE-mismatch in AMCs containing ceramic nanoparticles may be estimated by the following equation [47][48]:

$$\Delta\sigma_{CTE} = \alpha G b \left(\frac{12\Delta T \Delta C V_p}{b d_p}\right)^{1/2} \tag{5}$$

Where α is a material constant, G is the shear modulus, b is the Burgers vector, ΔT is the difference in manufacturing temperature and tensile testing temperature, and ΔC is the difference between the CTEs of the matrix and particles.

A difference in the elastic modulus (EM, also called Young's modulus) of the phases present in composites will also contribute to strengthening. In particular during tensile testing of the AMC where an EM-mismatch will contribute to the formation of dislocations around the ceramic nanoparticles, and thus increase the material strength. In AMCs, stiff ceramic particles will have a higher EM than the soft matrix. The strengthening effect, $\Delta\sigma_{EM}$ (in general, since EM-mismatch not only increases yield stress), of an EM-mismatch may be estimated by the following equation [46]:

$$\Delta\sigma_{EM} = \sqrt{3}\alpha G b \left(\frac{6V_p}{\pi d_p^3}\epsilon\right)^{1/2} \tag{6}$$

Where ϵ is the uniform deformation in the material (increases during tensile testing).

Using nanoparticles to reinforce AMCs, as opposed to microsized particles, leads to a comparably larger interfacial area with the matrix so that the total area of increased dislocation density (e.g. as a result of different CTEs or EM) is increased.

In dispersion-strengthened composites, the small reinforcing particles strengthen the material by introducing compressive strains in the lattice, increasing the dislocation density so that the movement of other dislocations is hindered [11]. For closely spaced, hard particles, this strengthening mechanism is known as *Orowan strengthening*. Propagating dislocations are pinned when they encounter non-shearable ceramic reinforcement nanoparticles in the composites. To further propagate, the dislocations must bow or glide around the nanoparticles. After the dislocations have passed, *Orowan dislocation loops* are created around the nanoparticles [49].

The effect of Orowan strengthening is commonly larger in nano-composites than in composites containing microparticles, because microsized particles are coarse and have large interparticle spacing [50]. A large interparticle spacing will reduce Orowan strengthening and have a negative effect on the mechanical properties of the composite [51].

Zhang et al. [50] found that particles with diameter smaller than 100 nm will be situated closer together and effectively hinder the propagation of dislocations, so that yield strength for nanoparticle reinforced composites is increased by $\Delta\sigma_{Orowan}$ [47][52]:

$$\Delta\sigma_{Orowan} = \frac{0.81 M G b}{2\pi(1-\nu)^{1/2}} \frac{\ln(d_p/b)}{d_p\left(\frac{1}{2}\sqrt{\frac{3\pi}{2V_p}} - 1\right)} \tag{7}$$

Where M is the Taylor factor and ν is the Poisson ratio of the material. A more general equation for the strength increase due to the Orowan mechanism (τ_{Orowan}), as a function of interparticle spacing λ is [51]:

$$\tau_{Orowan} = \frac{Gb}{\lambda} \tag{8}$$

In AMCs reinforced with larger particles, a *load transfer* between the soft matrix and the hard particles will contribute to strengthening. This effect of the load transfer is expected to have a small contribution on the strengthening of nanoparticle reinforced composites, since the required amount of particles for strengthening is lower [53].

For AMCs reinforced with small particles (≤ 50 nm in diameter), the most important strengthening contributions come from the interface between the nanoparticles and the Al-matrix, due to CTE mismatch and Orowan strengthening [2][54]. From Equation 5 to Equation 7, it may be seen that the CTE-mismatch, EM-mismatch and Orowan strengthening contributions are all increasing with the volume fraction of particles (V_p) in the composite and decreasing with the size of the particles (d_p).

Fattahi et al. [47] have made vital contributions in determining the effect of the different strengthening mechanisms for nanoparticle-reinforced welds. In their experiments, they used titanium dioxide (TiO_2), Al_2O_3 and TiC nanoparticles as

reinforcement and an 1100 Al alloy (commercially pure Al) as the matrix phase to create AMC fillers for Gas Tungsten Arc Welding (GTAW). The fillers were manufactured using Accumulative Roll Bonding (ARB, discussed in subsection 2.8).

To summarise the increase in yield strength ($\Delta\sigma_Y$) caused by the above mentioned mechanisms, researchers suggest different summation models. Fattahi et al. [47] found that the quadratic summation model (Equation 9) provided the best fit for their yield-strength measurements of welds produced with nanoparticle/Al composite fillers.

$$\Delta\sigma_Y = \sqrt{(\Delta\sigma_{GR})^2 + (\Delta\sigma_{CTE})^2 + (\Delta\sigma_{Orowan})^2} \qquad (9)$$

The estimated yield strength, $\sigma_{Y(est)}$ of the material may then be written as:

$$\sigma_{Y(est)} = \sigma_0 + \Delta\sigma_Y \qquad (10)$$

The main results from the calculations and welding experiments done by Fattahi et al., are presented in Table 2. The upper four values (average nanoparticle diameter, d_p, to grain size) were determined experimentally, while the remaining values were calculated using the corresponding equations mentioned above.

Table 2: Mechanical properties, grain size and relative contributions of the individual strengthening mechanisms to the yield strength of nanoparticle reinforced 1100 aluminium welds [47].

	Unreinforced	0.5vol% TiO$_2$	0.5vol% Al$_2$O$_3$	0.5vol% TiC
d_p [nm]:	-	50	40	60
σ_{UTS} [MPa]:	97	126	121	134
$\sigma_{Y(est)}$ [MPa]:	-	91.8	80.1	87.5
$\sigma_{Y(exp)}$ [MPa]:	46	71	65	78
Grain size [µm]:	93	54	46	37
$\Delta\sigma_{GR}$ [MPa]:	-	5.4	5.9	6.6
$\Delta\sigma_{CTE}$ [MPa]:	-	**56.1**	**46.2**	**52.5**
$\Delta\sigma_{Orowan}$ [MPa]:	-	**22.5**	**15.3**	**19.4**

As seen from Table 2, Fattahi et al. estimated that CTE mismatch ($\Delta\sigma_{CTE}$) and Orowan strengthening ($\Delta\sigma_{Orowan}$) had the largest effect on the yield strength for the nanoparticle reinforced 1100-Al welds. The estimated effect of grain size reduction ($\Delta\sigma_{GR}$) was not be of the same extent, despite the fine grain size achieved by adding the nanoparticles, due to the low Hall-Petch coefficient of Al ($=0.04\,\mathrm{MPa}\sqrt{\mathrm{m}}$) [47]. The experimental results indicated that the addition of TiC gives the strongest weld, both in terms of tensile strength (σ_{UTS}) and yield strength ($\sigma_{Y(exp)}$). According to Fattahi et al., the good mechanical properties of the composite welds were caused by the strong interfacial bonding and good "wettability" (discussed in subsection 2.7) between the molten aluminium and reinforcement particles, and the homogeneous distribution of the reinforcing particles [47].

In another article by Fattahi et al. [55], it was reported that the yield and tensile strength of welds increased with the weight fraction of TiC added to the 4043 Al-alloy filler wire, while the ductility decreased. The stress-strain curves from these experiments are presented in Figure 11.
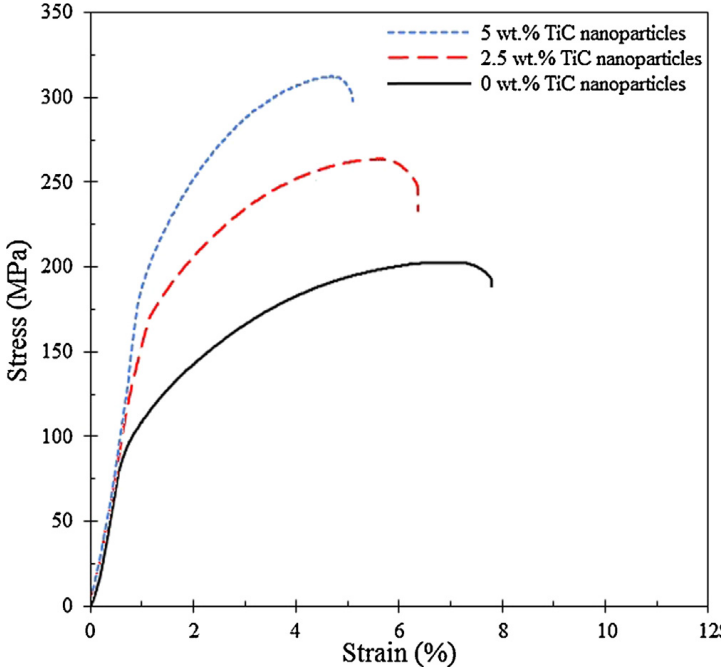
Figure 11: Measured stress vs. strain for joints welded using a 4043Al-TiC nano-composite filler material. From [55].

The behaviour showcased in Figure 11 above, illustrates the typical trend of increasing strength and brittleness with increasing the fraction of reinforcement particles in composites. The reinforcement particles acts as dislocations barriers, so increasing their numbers (i.e. higher volume/weight fraction) will increase the strength of the composite. But as a result, the volume of the plastic matrix acco-modating the deformation will decrease, leading to reduced ductility [56][57].

According to all the expressions for the strengthening of nano-AMCs discussed in this section (Equation 3 – Equation 7), reducing the reinforcement particle dia-meter (d_p) leads to larger strengthening contribution. Using equivalent relations, Casati and Vedani [2] calculated the strengthening contribution from each mech-anism (and the total strengthening contribution; $\Delta\sigma$TOT) as a function of the reinforcement particle size d_p in a 2wt% Al_2O_3 reinforced pure Al matrix compos-ite. Their results are shown in Figure 12.
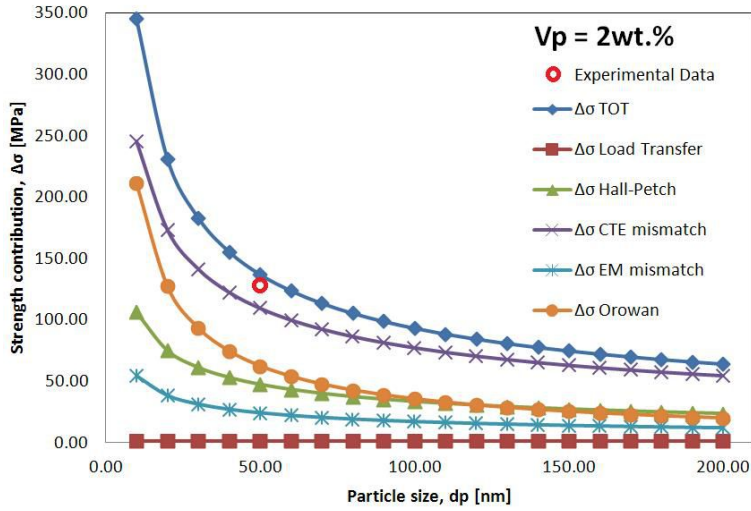
Figure 12: The effect of reinforcement particle size on the strengthening mechanisms in a 2wt% Al_2O_3 reinforced AMC. From [2].

Figure 12 shows that small reinforcement particles gives stronger composites, and that the contribution from load transfer is low for nanoparticle reinforced AMCs. Another incentive for the use of nano-sized reinforcement particles is that small particles are distributed more homogeneously (compared to larger particles) and do not fracture themselves, leading to both increased yield strength and ductility of the reinforced material [58].

Decreasing the size of the reinforcing particles will also have a positive effect on the hardness of composites. Kaftelen et al. [42] compared Al-Cu matrix composites reinforced with TiC particles in two different size ranges (0.6–3.5 µm and 0.8–5.6 µm) and found that the smaller reinforcement particles produced harder composites.

In summary, nanoparticle reinforced AMCs are highly promising composite materials, with a low weight and high strength compared to monolithic Al-alloys and microparticle reinforced AMCs, suitable for numerous applications. A critical requirement for reinforcement effect is that the nanoparticles are uniformly dispersed in the composite. If the particles agglomerate this will adversely affect the mechanical properties [41][47].

2.6 Heterogenous nucleation by the use of inoculants

In metal melts, heterogeneous nucleation is normally the process by which solidification occurs [59]. When the melt temperature is beneath the alloys liquidus temperature, the first solid nuclei form at inhomogeneities in the melt and are further transformed into larger solid particles as more and more nuclei solidify. When the phase transformation is complete, a solid grain structure will be formed [11]. Since the grains grow outwards from the initial solidification point, an inoculant particle is expected to be present in the middle of each grain if heterogeneous nucleation by inoculation has occured [40].

In casting or welding, a thorough understanding of the nucleation process is crucial to ensure strong mechanical properties in the produced material. To achieve high strength, a fine grain size is desired, as shown by the Hall-Petch relationship in Equation 2. A fine grain size also leads to other improvements in the produced alloy, such as a reduction in porosity, and reduced probability for hot tearing and cracking during casting or plastic deformation processing [40]. It is also often desired that the grains are equiaxed to create a material with isotropic physical properties on the macro scale and thus have satisfactory structural integrity in all directions.

By adding inoculant particles to the melt before solidification, the number of inhomogeneties at which heterogeneous nucleation may take place increases, so that many solid particles are formed in the melt at the same time. When these solid grains meet, the solidification stops and the grains do not grow further. If the inoculant particles are uniformly distributed in the melt, an alloy with a fine, equiaxed grain structure will be formed.

Grain refinement in casting of Al alloys is usually achieved by adding *Master alloys* (solid rods of e.g. Al-Ti-B or Al-Ti-C) to the Al-melt. These rods dissolve into inoculant particles (e.g. titanium boride (TiB_2) or TiC), which facilitate for nucleation of α-Al during solidification [40]. The effect of inoculation on the resulting grain structure of a cast aluminium alloy is shown in Figure 13 [40][60]. Here, three different micrographs are shown to illustrate the resulting grain structure of an Al-Mg alloy, with and without the addition of inoculants.
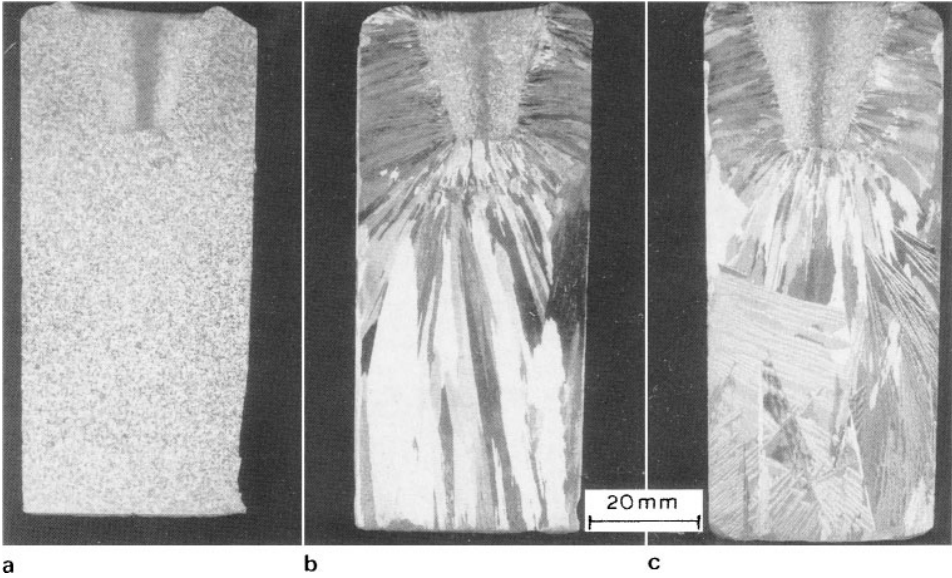
Figure 13: Optical macrographs of grain structures in solidified castings of aluminium alloyed with 2.5wt% Mg. Image from [40], re-given from experiments by McCartney [60]. **a**: Inoculant added; fine, equiaxed grain structure; **b**: No inoculant added; coarse, columnar structure; **c**: No inoculant added; coarse, twinned columnar grains.

Heterogeneous nucleation may be described theoretically by the *Spherical-cap* model. In this model, the solidified nucleus is represented by a "spherical-cap" forming on a solid substrate (e.g. an inoculant). This solid spherical-cap induces surface energies at the interfaces between the substrate, the spherical-cap (an α nucleus in the case of Al melts), and the molten metal. These surface energies are denoted σ, with the subscripts L for the liquid metal, α for the sperical cap and S for the substrate. The interfacial energies in the system determine the contact angle (Θ) between the solid-liquid interface and the substrate interface by the following equation [40]:

$$\cos\Theta = \frac{\sigma_{Ls} - \sigma_{\alpha L}}{\sigma_{\alpha s}} \tag{11}$$

When the contact angle Θ is low (below 90°), the solid particle is said to have high *wettability* with the liquid melt. High wettability indicates that the liquid-solid α interface energy ($\sigma_{\alpha s}$) is low. The solid inoculation particles will then be prevented from clustering together as they collide in the melt [44]. The *Spherical-cap* model is illustrated in Figure 14.
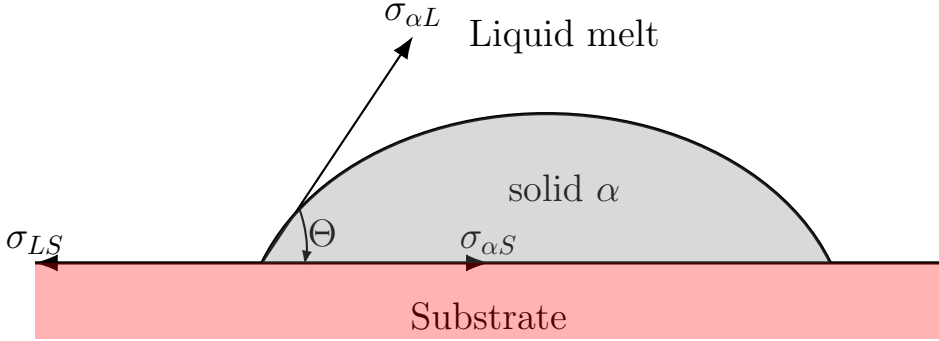
Figure 14: Solid "spherical cap" α-nucleus formed by heterogeneous nucleation on a substrate (i.e. an inoculant particle). The interfacial energies are indicated as σ, with a subscript designating the interface between the phases (L for the liquid melt, α for the solid grain and s for the substrate). Θ is the "contact angle" between the substrate and the solid α-nucleus. Redrawn from [60].

By considering the free energy during the nucleation, equations for a critical nucleus radius (r^*) and a thermodynamical energy barrier for heterogeneous nucleation (ΔG_{het}^*) may be derived. The critical radius is given by [11]:

$$r^* = -\frac{2\sigma_{\alpha L}}{\Delta G_v} \tag{12}$$

Where ΔG_v is the volume free energy.

When the radius of the solid nucleus is below r^*, the nucleus is not stable and may re-dissolve into the melt. The energy barrier for heterogeneous nucleation is given by [11]:

$$\Delta G_{het}^* = \left(\frac{16\pi\sigma_{\alpha L}^3}{3\Delta G_v^2}\right)S(\Theta) = \Delta G_{hom}^* \cdot S(\Theta) \tag{13}$$

Where ΔG_{hom}^* is the energy barrier for homogeneous nucleation (i.e. nucleation in the melt without the aid of a solid surface) and $S(\Theta)$ is a function only of the contact angle Θ, with a numerical value between zero and unity. The energy barrier of heterogeneous nucleation will thus always be equal to or less than the energy barrier of homogeneous nucleation.

An expression for the nucleation rate, $\dot{N}$, during solidification is given in Equation 14 (adapted from [11]).

$$\dot{N} = K\left[exp\left(-\frac{\Delta G_{het}^*}{kT}\right)exp\left(-\frac{Q_d}{kT}\right)\right] \tag{14}$$

Where K is a constant accounting for the number of solid nuclei formed and the number of atoms on a nucleus surface, k is the Boltzmann constant, T is temperature and Q_d is the activation energy for diffusion.

As the contact angle Θ decreases, so does the energy required to create a stable solid on the substrate, ΔG_{het}^*. The nucleation rate will then increase with decreasing Θ, as according to Equation 14. A small contact angle with the α-Al spherical

25

cap (i.e. high wettability) is therefore an important requirement of potent inoculants. This means that the interface energy between the inoculant particle and the α-nucleus, ($\sigma_{\alpha s}$) should be low. If this is the case, the driving force for nucleation is large. That is, the undercooling below the melting temperature required for solidification to occur is small, less than 1 K for potent inoculants [40].

2.7 TiC as inoculation particles in AMCs

TiC particles are used extensively for reinforcing aluminium matrix composites, and may also function as inoculants in Al melts [43][44].

Contreras et al. [61] have investigated the wetting of Al-Mg alloys on TiC-substrates. In their *sessile drop* experiments, it was found that the contact angle between the solidified Al-Mg cap and the TiC substrate stabilised below 60° for 1wt%Mg Al-alloy, and below 40° for the Al-alloy with 20wt% Mg. It is reasonable to assume that the contact angle for a 4.5wt% Mg Al-alloy will stabilise between 40 and 60°. The results of Contreras et al. are given in Figure 15.
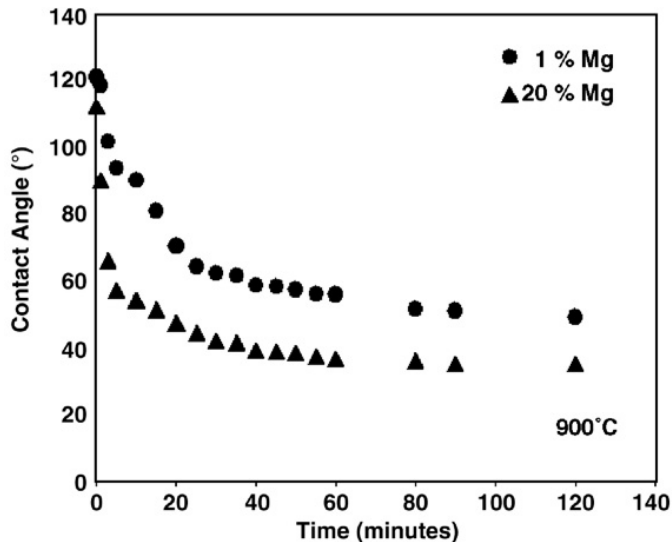
Figure 15: Time development of the contact angle between a TiC substrate and two different Al-Mg alloys. From [61].

Since the contact angle between the TiC substrate and the α-Al cap is small (less than 90°), TiC is said to have high wettability with the Al-Mg melt. High wettability prevents the TiC particles from clustering, so that a uniform distribution of particles in the Al-matrix is obtained. This results in a fine grain structure in the aluminium alloy after solidification. Kennedy et al. have investigated the grain-refining properties of TiB_2 and TiC. The effect of these inoculants on the grain structure in a cast pure Al alloy is shown in Figure 16 [44].

(a) Un-reinforced.

(b) Reinforced with 5 vol% TiB_2.

(c) Reinforced with 5 vol% TiC.
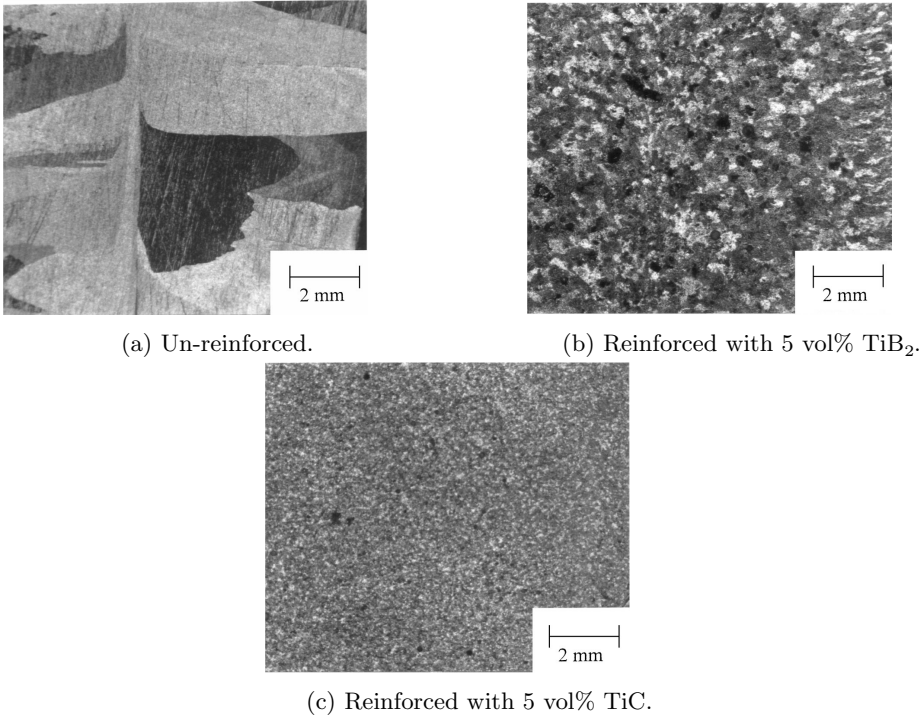
Figure 16: Optical macrographs of a cast commercially pure Al alloy, showing the grain structure with and without inoculants. The grain refining effect is larger for the TiC inoculants, compared with the TiB_2 inoculants. From [44].

It can be seen from Figure 16 that the resulting grain structure in TiC-reinforced composites (Figure 16c) is finer than in the pure alloy (Figure 16a) and in the TiB_2-reinforced composite (Figure 16b). Small-scale clustering of the TiB_2 particles was observed, while the TiC particles were more distributed uniformly. A proposed explanation for the distribution difference was that the molten Al wets the TiC particles better than the TiB_2 particles, leading to less agglomeration of TiC particles. Kennedy et al. suggested that this small-scale clustering explains why the grain structure of the TiB_2 reinforced composite was coarser than the TiC composite [44].

Kennedy et al. also found that the TiC-reinforced composite had higher stiff-

ness, strength and ductility than the composite reinforced with TiB_2, which was attributed to the stronger interfacial bonding between the reinforcement TiC particles and Al-matrix in the Al-TiC system [44].

2.8 Manufacturing of nanoparticle reinforced MMCs

The main challenge related to the manufacturing of metal matrix nano-composites (MMnCs) is to achieve a uniform distribution of the reinforcement particles. This is a crucial requirement for producing strong composite materials [2].

Casati and Vedani present various manufacturing techniques in their review on the production of bulk nanoreinforced MMCs [2]. The different techniques are divided into liquid, semi-solid and solid production methods.

In composites manufactured by the conventional liquid-casting metallurgical approach, many ceramic nanoparticles will cluster together due to low wettability with the molten metal matrix, high surface-to-volume ratio and high viscosity. This results in an heterogeneously reinforced material. To avoid clustering in liquid-state processes, high intensity ultrasonic waves may be used to create collapsing micro-bubbles in the melt, which break up the nanoparticle clusters. The nanoparticles are then dispersed evenly in the liquid metal [2].

Liu et al. [4] mixed potassium aluminium fluoride $KAlF_4$ salts and TiC nano-particles to effectively manufacture Al-TiC nanocomposites with a uniform particle distribution, through a solidification process. The molten Al was mechanically stirred to avoid clustering of the TiC nanoparticles. An overview of this salt-assisted solidification method is shown in Figure 17.
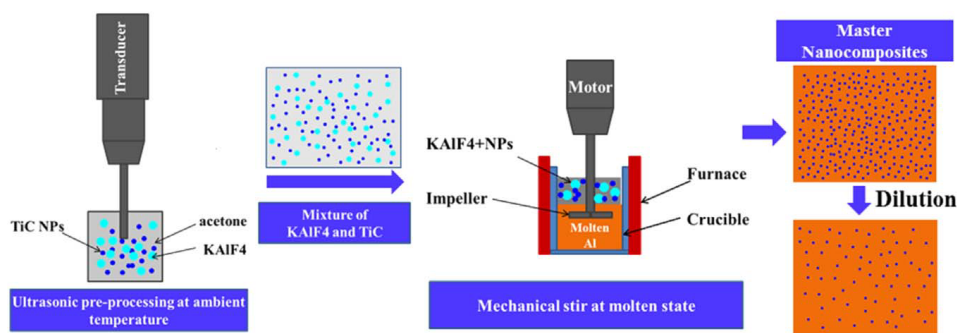
Figure 17: Salt assisted solidification method, used to produce uniformly reinforced Al-TiC nanocomposites by introducing TiC nanoparticles to molten Al. The molten Al is stirred to avoid clustering. Ultrasound is used in pre-processing to mix the TiC nanoparticles and the salt ($KAlF_4$). From [4].

Other liquid state MMnC-manufacturing processes processes include disintegrated melt deposition, in-situ processing, selective laser melting and melt stirring [2]. A disadvantage with the liquid state processing methods is that the high temperatures may result in the formation of unwanted reaction products (as shown in subsection 2.9).

A semi-solid MMnC-production method is *rheocasting*. In rheocasting, pre-heated nanoparticles are added to a semi-sold metal slurry under vigorous stirring to achieve uniform distribution. The slurry is then squeezed to a solid form, using a hydraulic press. Semi-solid casting is another promising method, shown to produce composites with the same strength as ultrasound-assisted cast MMnCs, but with higher ductility [2].

Solid state methods often use metallic and ceramic powders as starting materials to produce MMnCs. A common solid-state technique is *mechanical alloying*. In this method, powders are repeatedly cold welded, fractured and re-melted in a high energy ball mill, in order to produce a powder mixture with a uniform distribution of ceramic nanoparticles. The powder mix is further pressed to a compact material, through a variety of different hot or cold pressing/extrusion techniques (in some cases sintering is also used) [2].

Fattahi et al. used a solid-state spray technique known as accumulative roll bonding (ARB), to produce ceramic nanoparticle/Al composite filler wires for use in Gas Tungsten Arc Welding [47]. The ceramic nanoparticles used were TiO_2, Al_2O_3 and TiC. An image showing the process steps in ARB is shown in Figure 18 [47].
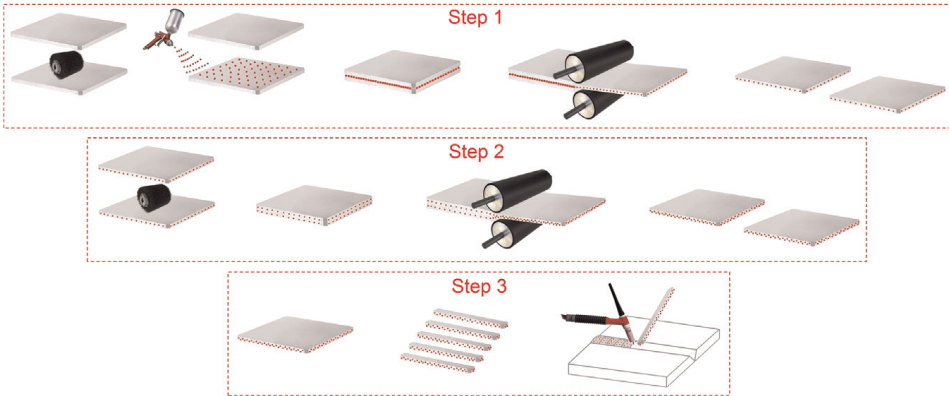
Figure 18: The processing steps in the accumulative roll bonding technique used by Fattahi et al. to manufacture a nanoparticle/Al composite filler wire. From [47].

The ARB method is an iterative process, with the starting point of a powder-layer of nanoparticle ceramic particles "sandwiched" in between two aluminium metal plates. This "sandwich" was rolled and cut into two equally sized rectangular rods, which were then rolled again. After a satisfactory number of rolling steps, the plate was cut into thin plates which were used as fillers in welding of two 6061 Al plates. Fattahi et al. reported that a uniform distribution of nanoparticles in the fillers was achieved through ARB [47].

2.9 Instability of TiC in AMCs

There are some difficulties involved with the use of TiC as reinforcement in AMCs, mainly related to the instability of TiC at elevated temperatures. Kennedy et al. [5] found that titanium aluminide ($TiAl_3$) precipitates and brittle aluminium carbide (Al_4C_3) blocks form at the TiC-matrix interface when held at higher temperatures (600-900°C) for extended periods (over 48 hours). These precipitates will deteriorate the mechanical properties of the composite, therefore their formation should be avoided. The following reaction was suggested:

$$13\,Al(l/s) + 3\,TiC(s) \longrightarrow 3\,TiAl_3(s) + Al_4C_3(s) \tag{15}$$
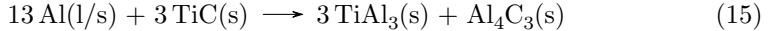
The reaction above occurred in molten Al above 600°C, but also in solid Al-TiC composites at 600°C. At 900°C, TiC was found to be stable [5].

When using Al-Mg alloys as the matrix in AMCs, it is crucial to consider the interfacial reactions that may occur between the Al-Mg matrix and TiC at elevated temperatures (e.g. during manufacturing). Pure Mg does not form thermodynamically stable carbides, but will react with oxygen (O) to form MgO. The Al_2O_3 oxides present on the surface of Al-alloys, which are stable in pure Al, may react in the presence of Mg and O to form $MgAl_2O_4$ [62].

Contreras et al. [3] studied the reactions that occur between molten Al-Mg alloys and TiC. This was done by wetting solid, dense TiC substrates with a drop of Al-Mg, at temperatures between 750 and 900°C. The holding time was 120 minutes. After the Al-Mg drop had solidified, the chemical composition of the interface between the TiC substrate and the Al-Mg drop was analysed. Both Al_4C_3 and $TiAl_3$ was detected, presumably formed by the reaction in Equation 15. Contreras et al. include the possibility that $TiAl_3$ could also have formed as a consequence of a TiO_2 oxidation layer at the TiC substrate, through the following reaction:

$$13\,Al(l) + 3\,TiO_2(s) \longrightarrow 3\,TiAl_3(s) + 2\,Al_2O_3(s) \tag{16}$$
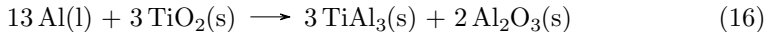
Lee et al. [63] also detected reaction products in a TiC reinforced Al-Mg matrix composite, fabricated by the *Pressureless infiltration technique*. Temperatures in the range of $700 - 1000$°C were used, and the holding time was 1 to 5 hours. Many different compounds were found near the interface between TiC particles and the Al-Mg matrix, among those Al_4C_3 and $TiAl_3$.

To avoid the formation of deteriorating reaction products, temperatures during manufacturing of TiC-reinforced AMCs should be kept below 600°C. If higher temperatures must be used, the holding time should be minimised.

2.10   Screw extrusion

Screw extrusion is a continuous manufacturing process, applying an "Archimedes" type screw to create an extruded profile. Feedstock material is introduced to the system as solid granules or pellets, in a feed hole at the rear end of the screw. As the screw rotates, material is pushed forwards in a chamber, compacted and then forced through an orifice in the die at the front of the machinery, as a forward pushing pressure gradient evolves. Thus, an extruded profile is made.

Screw extruders with one rotating screw are referred to as *Single-screw extruders*. It is also possible to use multiple screws for increased mixing and compounding of the solids. Screw extruders with two screws are known as *Twin-screw extruders*, and screw extruders with three or more screws are known as *Multiple-screw extruders* [64].

The geometry of the rotating screw may also be tailored to suit different purposes. Screws are commonly designated either as single flight (SF) or double flight (DF) screws. SF screws have one thread running along the screw stem in a spiral motion, while DF screws have two symmetric threads on opposite sides of the screw stem. Sketches of the two screw types are shown in Figure 19a [65]. A schematic side-view drawing of a screw extruder is shown in figure 19b [65].
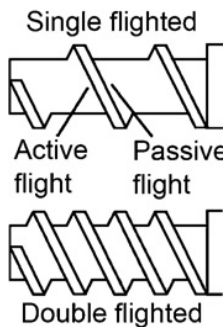
(a) Types of screws and their geometries.   (b) Designation of essential parts.
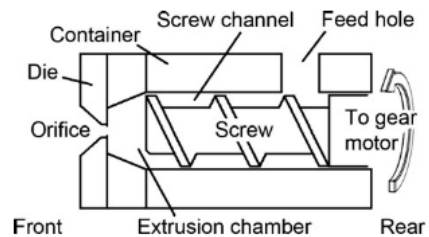
Figure 19: Schematic drawing of a screw extruder. From [65].

The *active* flight of the screw is the side of the thread that participates in pushing the material forwards when rotating. This side will be subjected to large pressure forces. The *passive* flight does not push the material, but rotates around in front of it.

Screw extruders are fundamental processing tools in the polymer industry. Since the 1950s, screw extruders have been used to manufacture various rubber and plastic products such as films, construction materials and polymer pipes. Because screw extrusion is a continuous process, with a range of different processable polymer materials, it is one of the most popular production methods for polymers [64]. The raw materials are polymers in the form of solid granules or pellets (as shown in Figure 21). From the rotation of the screw, a friction force occurs between the screw, the solid granules, and the barrel wall. The friction will increase the tem-

perature in the system, but in some cases external heaters are also applied. Due to the low melting point of polymers, the solid granules are transformed into a low-viscous melt even at moderate temperatures. This melt is pushed forward by the rotational motion of the screw [66].

2.11   Metal Continuous Screw Extrusion

The use of screw extruders is no longer limited to the polymer industry. Due to recent research advances, screw extrusion of metals is now possible. The technology facilitating for **solid-state** screw extrusion of metals is known as Metal Continuous Screw Extrusion (MCSE), and is developed at **NTNU** (Norwegian University of Science and Technology), in collaboration with the aluminium production company **Norsk Hydro** [67].

A model of the developed single-screw extruder used for MCSE is shown in Figure 20 [6].
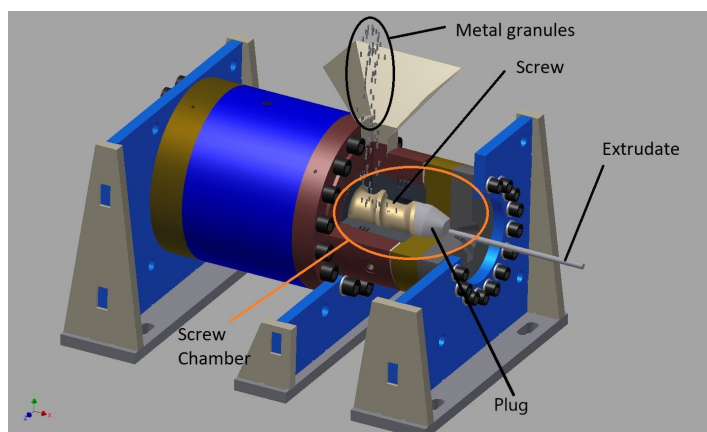
Figure 20: 3D model of the metal continuous screw extruder developed at NTNU, in cooperation with Norsk Hydro. From [6].

As seen in Figure 20, solid granules are added through a feed hole at the rear end of the screw. The granules trickle downwards in the extruder and land at the bottom of the screw chamber. Due to the friction which arises between the granules and the tooling surfaces in the machine, the rotating screw will push the granules forwards in the screw chamber. To achieve efficient forward material flow in the extruder, the friction between the granules and the internal walls of the screw chamber should be large, while the friction between the granules and the screw itself should be low [65]. Figure 21 shows a sketch of the different stages for the added material during MCSE, as described in the original patent by Werenskiold et al. [67].
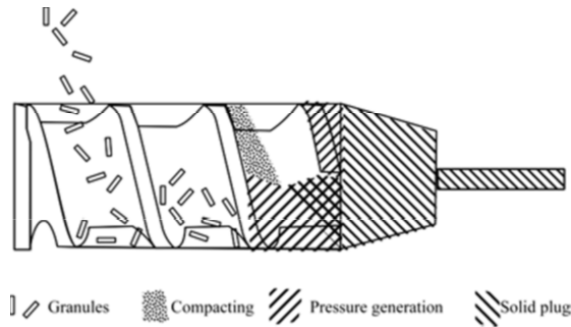
Figure 21: Illustration of the different process stages during MCSE. From [67].

As more and more granules are added, a solid plug will form in the extrusion chamber at the screw front, and a pressure build-up will commence. The material is consolidated due to the high pressure and temperature in the system, and the large shear strains caused by the rotation of the screw [65]. The pressure in the screw chamber continues to increase until it is high enough to push the solid material out of the chamber, through the die orifice at the front of the extruder. This creates an extruded profile. As long as the screw rotates, the temperature is controlled and granules are added, a solid profile will be continuously extruded.

The process of screw extruding highly-viscous materials, such as aluminium, poses different challenges compared to polymer screw extrusion. MCSE is also a fully solid-state process, unlike polymer screw extrusion, and the forces required to deform and extrude solid metal are, naturally, larger than for polymer melts. Therefore, a more powerful engine to rotate the screw is necessary for MCSE. Additionally, the operating temperature for metal screw extrusion is higher than for polymer extrusion, since the energy demand for decreasing the viscosity is larger. To ensure sufficiently low viscosity of the consolidated material, and prevent cracking from thermal stresses, the steel-machinery used in MCSE is heated with an induction coil in front of the screw extruder. The induction heating is applied before and during screw extrusion [6].

If the temperature in the rear part of the screw extruder (near the feeding hole) exceeds a certain level ($\sim 280°C$), compaction and sticking friction may occur [6]. The consolidated material will then extend backwards along the screw, leading to an excessive load on the gear motor. The rotation of the screw will then stop (by a failsafe mechanism), and the steel barrel and the screw will both be stuck in the aluminium. The backwards (with respect to the extrusion direction) propagation of heat is avoided by cooling the extrusion chamber with compressed air, through cooling ribs in the container barrel. The cooling medium also aids in achieving stable temperature conditions for each experiment. The temperature during MCSE is measured and logged using thermocouple wires at different positions in the extruder.

MCSE may use recycled aluminium scrap as feedstock, facilitating for solid-state recycling of aluminium. Solid state recycling of Al uses less than 7% of the

energy required for state-of-the-art remelting routes [68]. When compared to other solid state recycling routes for Al, Duflou et al. [69] found that screw extrusion had the smallest environmental impact per kg material, measured in the dimensionless energy consumption unit milipoints [mPt]. Their results are included in Figure 22.
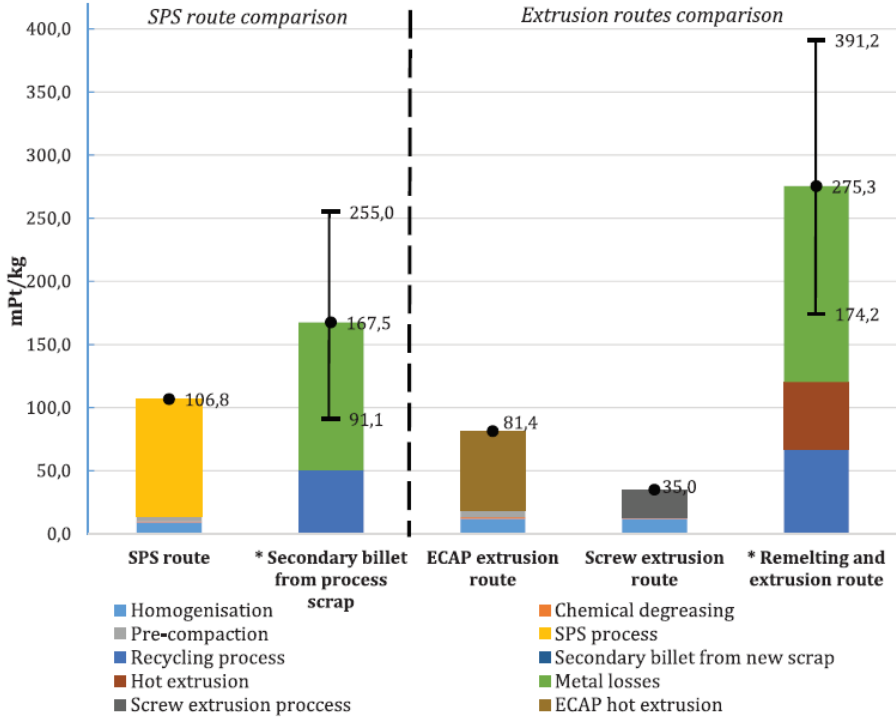
Figure 22: Environmental impact of different recycling processes of aluminium. From [69].

As a novel processing method, MCSE is expected to produce materials with unique properties, that may be applicable in many industrial sectors. In this work, MCSE is used to produce a TiC-nanoparticle reinforced (5183-)AMC wire. Normally, the manufacturing of MMCs (including AMCs) involve at least two steps; consolidation or synthesis (introducing reinforcement into the matrix) and shaping [11]. Using MCSE, both consolidation and shaping (by extrusion) is achieved in a single processing step.

Further information on MCSE may be found in the PhD thesis: *Screw extrusion of light metals: development of materials, characterization and process analysis* by Kristian Grøtta Skorpen [6].

2.11.1 Flow during MCSE

An important aspect to consider in screw extrusion is the material flow through the screw chamber. The flow will affect the resulting microstructure and properties of the extruded material, as well as the effectiveness of the extrusion. Widerøe and Welo [65] used materials with different etching properties (a 6060 Al-alloy and Al alloyed with 1.8 wt% copper) to illustrate metal flow during screw extrusion. The 6060 alloy was extruded first, then the Cu-rich alloy was added. After extrusion was completed, the aluminium plugs (remaining inside the screw extruder) were cut along the transversal and longitudinal plane, and etched in concentrated NaOH. The Cu-rich alloy develops a black colour under etching, while the 6060 alloy keeps its metallic (white) appearance. This colour difference displays the metal flow in front the screw, in longitudinal and transversal direction.

Photos of two screw plugs are shown in Figure 23. Plug **a** was retrieved after 30 s of feeding the dark contrast material (Cu-rich Al-alloy), plug **b** after 60s. The photos are created by merging one photo of the longitudinal plane of the plug and one photo of the transverse plane.
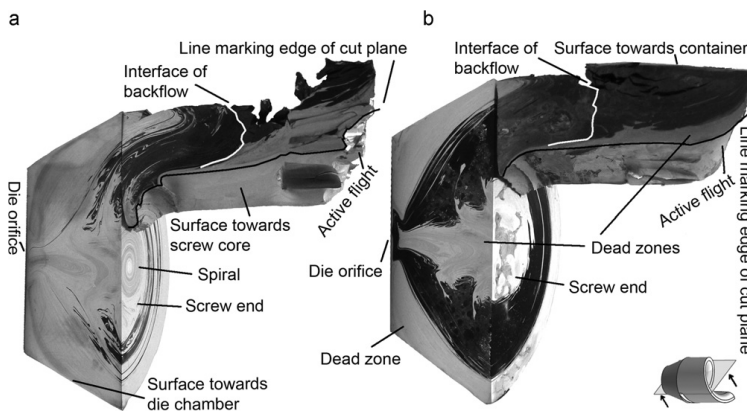
Figure 23: Etched aluminium plugs from screw extrusion using a single flight screw, illustrating the material flow. (a): after 30 s of contrast material feeding; (b): after 60s. From [65].

As seen from Figure 23, the new material (Al-Cu, black) and the old material (6060 Al-alloy, white) are in some areas mixed, resulting in an alternating black and white spiral pattern. In other areas, near the middle and at the edge, the white material still dominates. These areas are so-called dead zones, were the material does not move within the screw channel. In between the middle and the edge of the plugs, the new, black material predominates after 60 s. This is due to a higher sticking friction along the chamber walls, slowing down the material flow near the edges of the plug. The central zones have no restricting friction [65].

Figure 23 **a** illustrates that asymmetric material flow occurs in single flight screw extrusion, since the spiral core is located slightly below the centre of rotation. This is a consequence of the material only being pushed forward by the active flight,

which produces an unsymmetrical product. A more symmetrical flow path may be seen in Figure 24, which shows the screw plugs from a double flight screw extrusion experiment.
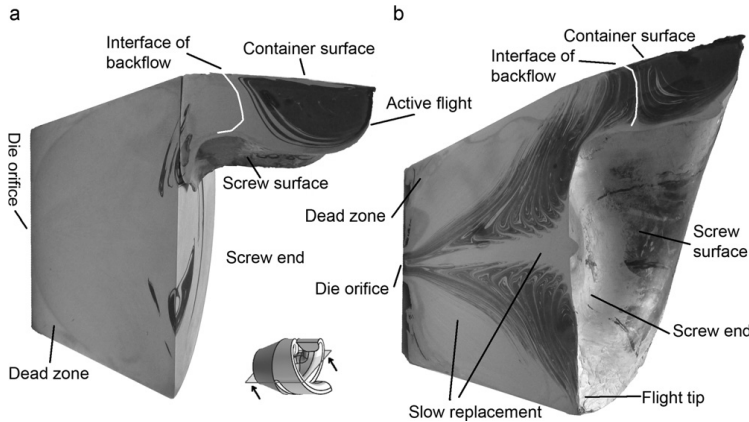
Figure 24: Etched aluminium plugs from screw extrusion using a double flight screw, illustrating the material flow. (a): after 30 s of contrast material feeding; (b): after 60s. From [65].

The double flight screw pushes the material forwards at two points simultaneously, since there are two active flights across from each other. This results in a more symmetric material flow.

In summary, the typical flow pattern in the screw channel during extrusion may be illustrated as shown in Figure 25 [65].
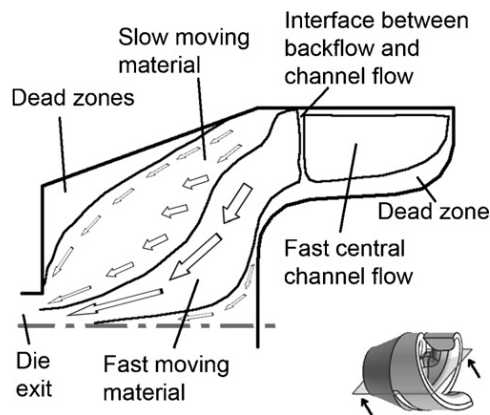
Figure 25: Typical material flow pattern in the screw channel during extrusion, from [65].

2.12 Improving weldability of Al-alloys using nanoparticles

The incorporation of ceramic nanoparticles to metallic alloys may improve other material properties than strength and grain size; the weldability may also be greatly enhanced. The aluminium alloy 7075 is traditionally known to be non-weldable, as hot cracking occurs during welding. Sokoluk et al. [70] recently found that by incorporating 1.7vol% 40–60 nm diameter TiC nanoparticles to 7075 welding filler rods, the formation of hot cracks was minimised. The filler rods were fabricated using the salt-assisted liquid state incorporation method [4], discussed in subsection 2.8 and illustrated in Figure 17. Images documenting the macroscopic effect of the TiC nanoparticles on hot crack formation during Gas Tungsten Arc Welding (GTAW), are shown in Figure 26.
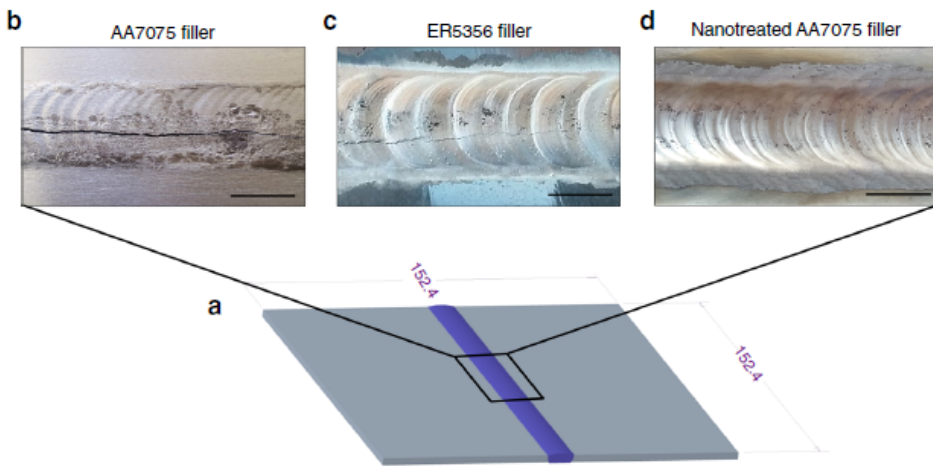
Figure 26: Weld appearance after Gas Tungsten Arc Welding of two 7075 Al-alloy sheets. **a**: Dimensions of the two 7075 Al plates welded together. **b** and **c**: Hot cracks formed during the welding using, respectively, 7075 and 5356 Al alloy as fillers. **d**: Bead melting zone of the 7075TiC weld, showing no macroscopic signs of cracking. The scale bar in all images is 10 mm. From [70].

From the images above, it may clearly be seen that the incorporation of TiC nanoparticles (shown to the right, figure **d**) to the welding rods have prevented the formation of hot cracks during GTAW. Thus, by adding TiC nanoparticles to the 7075 alloy, the non-weldable alloy became weldable.

Additionally, it was found that the TiC particles gave a fine-grain structure in the weld which in turn gave exceptional post-weld tensile strength (UTS≈ 525 MPa) compared to other common Al-filler materials (see e.g. Table 2). It is expected that the same nanoparticle-treatment may give similar results for other hot crack susceptible metal alloys.

2.13 Wire Arc Additive Manufacturing

Additive Manufacturing (AM) technologies are manufacturing methods being introduced to automotive, aerospace and biomedical industries at a rapid pace. AM methods provide increased design freedom and possibilities for fast prototyping, in addition to high cost and resource efficiency, compared with traditional manufacturing methods [71]. AM-products are created as layer-by-layer three-dimensional (3D)-structures, with the possibility of using both polymers and metals as feedstock. A division of AM into 7 different categories (based on deposition technique), showcasing the variety of materials suitable for AM, is included in Figure 27 [9].
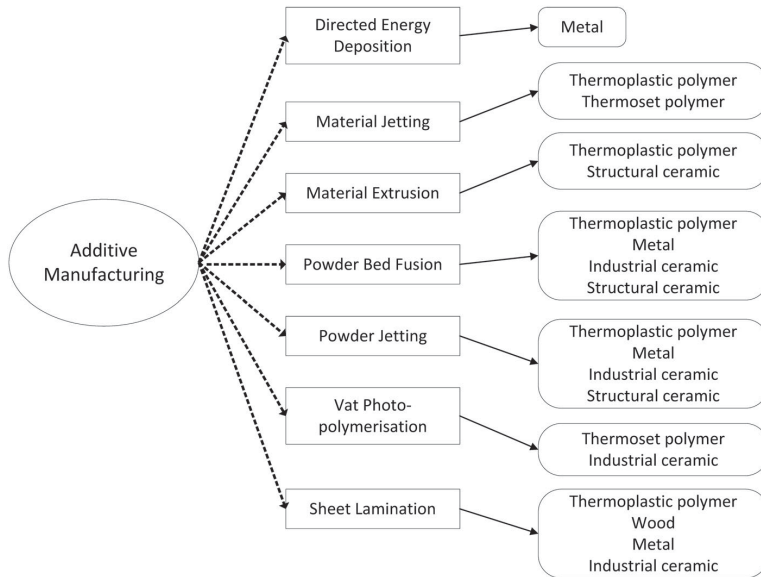
Figure 27: Classification of different additive manufacturing technologies, based on deposition technique. The materials which may be used for each process are written in the blocks to the right. From [9].

From Figure 27 it is seen that four of the seven different AM-processes may be used to create metal products. Among these four, directed energy deposition (DED) is one of the most common for AM of metals. The different categories of DED are shown in Figure 28 [9].
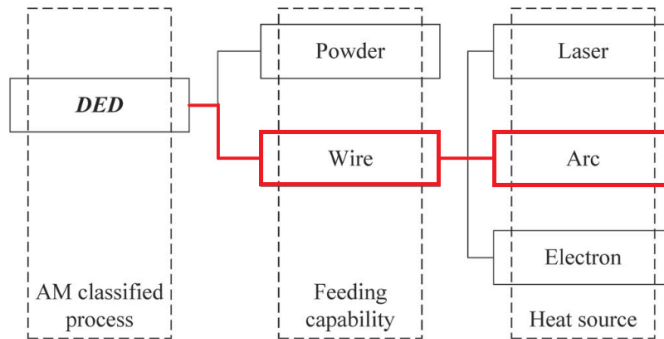
Figure 28: Classification of the different Directed Energy Deposition techniques, from [9]. The red lines indicate the wire arc additive manufacturing (WAAM) process.

The path shown by the red lines in Figure 28 indicates the method known as Wire Arc Additive Manufacturing (WAAM). In WAAM, a metal wire is heated beyond its melting point by an electric arc. The molten metal is then deposited on an underlying metal structure and quickly solidifies, forming a new layer of material. The underlying metal also melts and solidifies, so that a metallic bond is formed between the metal layers. A wire-feeding mechanism pulls more wire into electrical contact with the arc, facilitating for continuous deposition of new material. A positioning system moves the weld gun around to create a 3D structure. In principle, this process is the same as conventional arc-welding, combined with a positioning system.

A WAAM-setup used by researchers at Technische Universität Darmstadt is shown in Figure 29a [72]. The fundamental parts of a WAAM system are illustrated in Figure 29b [73].

(a) Image taken during a wire arc additive manufacturing (WAAM) experiment at Technische Universität Darmstadt, showing a typical WAAM-setup. From [72].
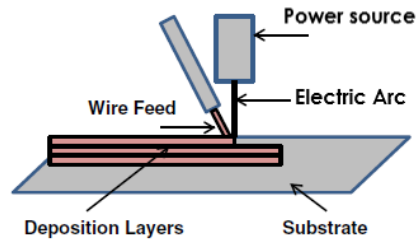
(b) Sketch of the fundamental components of a WAAM system. Adapted from [73].

Figure 29: The WAAM system.

The advantages of WAAM, compared to other AM methods, are high deposition rates, low material and equipment costs and good structural integrity [74].

Using wire as the starting material, compared to powder, lowers the cost and increases the possible size of the manufactured product. The dimensions of structures produced by powder-processes are limited by the size of the surrounding chamber required to provide an inert atmosphere [73]. Most WAAM-products may be manufactured in an ambient atmosphere, with a local gas shielding of the weld arc. Thus, the dimensions of WAAM products are not limited by a chamber size. Powder-bed processes are suitable for complex parts demanding high resolution, but the deposition rate is one order of magnitude lower than for WAAM [74]. For simple to medium complex parts, WAAM is the most suitable AM method [73].

Since the WAAM-process may use conventional welding wires, there is already a wide range of starting materials available. Still, these wires have potential for improvement. Martin et al. [10] found that by introducing nanoparticle nucleants to Al powders for powder-additive manufacturing, the resulting 3D-printed products had crack free, equiaxed grains and thus high structural integrity. It is believed that the introduction of nanoparticles will also benefit structures produced by the WAAM method. The work done by Fattahi et al. [55] indicates that introducing ceramic nanoparticles to wires used for WAAM will give products with increased hardness and yield strength, compared to the use of unreinforced metal wires.

WAAM is particularly suited for AM of Al-alloys, compared to using powder-feedstock, as Al-powders have a large surface area and therefore larger amounts of oxides than wires. These oxides are difficult to remove due to their thermodynamic stability. Another disadvantage of using powders for AM of Al is that the low

melting point of Al (at 600°C) makes it difficult finding a suitable binder-material, which is needed for the selective laser melting approach [75]. Thus, WAAM is the most promising candidate for AM of Al-alloys.

3 Experimental procedures

In this section, the characteristics of the raw-materials, the utilised equipment and methods are presented. First, flow charts summarising the experimental procedures are presented. A flow chart illustrating the experimental pre-treatment procedure before MCSE, and experimental conditions during MCSE, is shown in Figure 30.
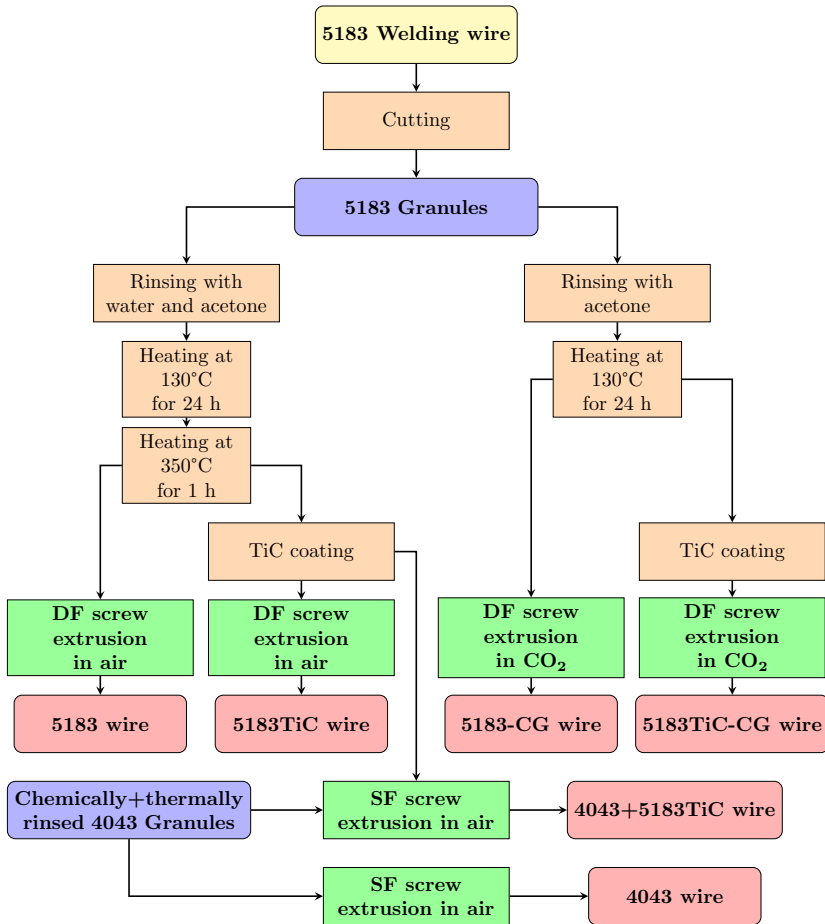
Figure 30: Preparation and screw extrusion procedure for produced wires. The **4043** granules were rinsed using the same procedure as for the **5183** granules (cutting, rinsing in water and acetone, heating at 130°C for 24 h and 350 °C for 1 h). The abbreviations SF (single flight) and DF (double flight) indicate screw geometry.

A flow chart illustrating the sample preparation and investigation methods applied after MCSE is shown in Figure 31.
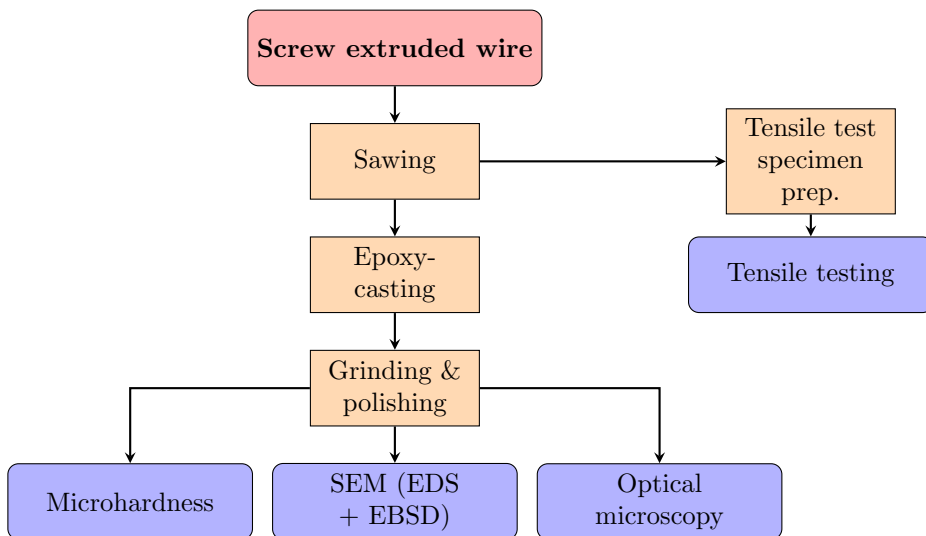
Figure 31: Sample preparation and characterisation methods.

The experimental procedure and sample preparation methods are written in more detail in the following subsections.

3.1 Chemical analysis and preparation of materials

Granules of the commercial aluminium alloy 5183 were used as the starting material for MCSE. The 5183 aluminium alloy was produced by **Safra**, and delivered as a 1.2 mm diameter welding wire. To measure the chemical composition of the provided material, the wire was cut into granules, which were cast to a disk sample and sent to **Hydro Sunndalsøra** for Optical Emission Spark Analysis (OES). The composition was estimated from the average values of four sparks. The results from the OES analysis are given in Table 3. The composition as according to the datasheet provided by **Safra** (included in section A in the appendices), is shown for comparison.

Table 3: Measured chemical composition of 5183 welding wire, compared with values from the datasheet supplied by the producer Safra. The datasheet may be found in section A in the appendices.

Element	Content [wt%]	
	OES	Datasheet
Al	Balance	Balance
Mg	4.65	4.3-5.2
Fe	0.12	<0.40
Ti	0.11	<0.15
Cu	0.01	<0.05
Mn	0.66	0.6-1.0
Si	0.15	<0.25
Zn	0.01	<0.25
Cr	0.09	0.05-0.25

From the table above, it may be observed that the OES measured values fall well within the given composition values given by the supplier, **Safra**.

To transform the welding wire into granules suitable for MCSE, wire pieces were bent by hand into approximately 40 cm long bundles (shown in Figure 32a). These bundles were then inserted into the rotating knife apparatus (Figure 32b) to produce 5–15 mm long granules (shown in Figure 32c).

A parallel batch of 4043 (Al-5wt%Si) granules was prepared using the same procedure as for the 5183 granules.
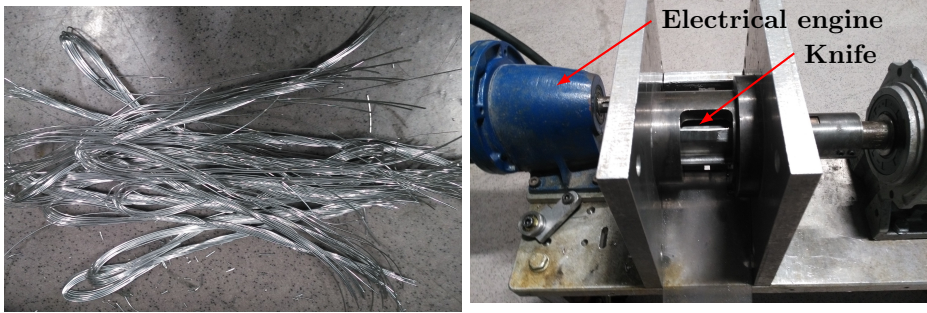
(a) Bundles of 5183 welding wire.

(b) Rotating knife apparatus.
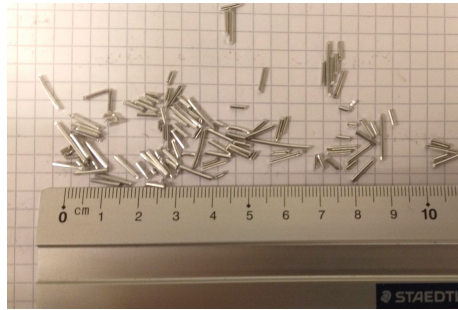
(c) 5183-granules

Figure 32: Materials and equipment in the granule preparation procedure.

A total of six wires were made, differing in granule material, preparation procedure and screw extrusion conditions (as shown in Figure 30). The motivation for the variations in the experimental conditions was to investigate if the pre-treatment procedures affect the presence of oxides in the screw extruded wire, as well as the influence on the mechanical properties. The mixed 4043+5183TiC wire was produced in an attempt to illustrate flow conditions in the SF screw extruded wire.

Table 4 shows the details regarding the different screw extruded wires. The different wires and the corresponding granules are hereon referred to by their alloy designation, with **"TiC"** added at the end for the composite wires. The wires produced with CO_2 as a cover gas during the screw extrusion, and from granules not rinsed with water or thermally rinsed at 350 °C to inhibit oxidation of the Al-Mg alloy, are additionally designated with **"-CG"** (abbreviation for cover gas). Table 4 also summarises the pre-treatment method of each wire. All extruded wires had a measured diameter of ≈ 9.8 mm ± 2 mm. The reason for the large deviation in wire diameter was that the screw extruder die was been damaged/worn in earlier experiments, as shown in Figure 36. This resulted in irregular, elliptical transversal cross-sections of the wires, shown in Figure 52 in the results section (section 4). Some variation may also be attributed to the varying screw extrusion speeds, which depends on granule feeding rate, temperature and screw rotation speed.

Table 4: Material, pre-treatment and screw extrusion conditions for the different wires/granules. The abbreviations for the screws are: SF=single flight, DF=double flight. All wires had a diameter of $9.8\,\mathrm{mm} \pm 2\,\mathrm{mm}$.

Designation	Chemical cleansing	Thermal cleansing	Atmosphere	Screw
5183	Acetone+Water	130°C - 24 h. 350°C - 1 h.	Air	DF
5183TiC	Acetone+Water	130°C - 24 h. 350°C - 1 h.	Air	DF
5183-CG	Acetone	130°C - 24 h.	CO_2-rich	DF
5183TiC-CG	Acetone	130°C - 24 h.	CO_2-rich	DF
4043	Acetone+Water	130°C - 24 h. 350°C - 1 h.	Air	SF
4043 +5183TiC	Acetone+Water	130°C - 24 h. 350°C - 1 h.	Air	SF

The 4043 and 4043+5183TiC wires were produced in the same screw extrusion session, by first adding 4043 granules, and then adding 5183TiC granule after some 4043 had been extruded. Thus, wire 4043+5183TiC was produced as a mixture of the two alloys. The first part of the wire was pure 4043, the rest a 4043+5183TiC mixture.

For the wires produced in ambient atmosphere, compressed air was used continuously to cool the screw extruder during extrusion. When the extrusion was performed in the CO_2-rich atmosphere, no cooling air was used until high temperatures deemed it necessary. This was another measurement made to prevent the formation of oxides.

3.1.1 Chemical cleansing

A chemical cleansing procedure was implemented to remove dirt and grease from the granule surfaces. The granules were poured into a large (approx. 10 L) bottle containing some (approx. 1 dL) acetone. The bottle was shaken by hand for about 1 min, before the content in the bottle was poured into a sieve to remove the acetone. At this point, the chemical cleaning for the granules intended for screw extrusion using CO_2 cover gas was stopped to avoid oxidation and minimise the amount of oxides and hydroxides in the "-CG" wires, which could form through surface reactions between the granules and water (producing e.g. aluminium hydroxide, $Al(OH)_3$). The other granules were further rinsed with tap-water in the same bottle.

3.1.2 Thermal cleansing

Residue from the chemical cleaning step was removed by heating the granules according to the following procedure:

1. Heating at 130 °C to remove acetone (and eventual water) from all granules. The heating was done in a *Termaks* heating cabinet.

2. Degreasing at 350 °C of the granules intended for wires 5183, 5183-TiC, 4043 and 4043+5183TiC. This was done in a *Nabertherm* P300 thermical convection oven.

Both the *Termaks* heating cabinet and the *Nabertherm* P300 thermical convection oven were operated in an ambient air atmosphere. The temperatures for the pre-treatment were chosen based on the observations made on the pre-treatment of materials for screw extrusion in the PhD thesis *Solid state recycling of aluminium scrap and dross characterisation* by Jirang Cui [68].

3.1.3 Coating with TiC-nanoparticles

After thermal cleansing, the preparation of the granules intended for the manufacturing of the monolithic 5183 wires was finished. The granules intended for the production of the 5183TiC composite wires were further dry coated with TiC. This was done by mixing the granules and TiC nanoparticle powder in cylindrical containers, which were further placed on top of a rotating roller mixer (*IKA Roller 10 Digital*, shown in Figure 33a). The weight ratio of TiC to Al for all the coated granules was 3/100, i.e 3wt% TiC. During storing and extrusion, some of the TiC particles dusted off the granules, so the fraction of TiC is most likely below 3wt% TiC in the extruded wires.

The coating-treatment was done by Sintef Industry. The roller rotation speed was 60 RPM (rounds per minute) and the treatment duration was 5 days. An image of the wire-granules without TiC-coating (left) and with TiC-coating (right) is included in Figure 33b.

(a) *IKA Roller 10 Digital* rotating roller mixer, used to cover the 5183 wire granules with TiC coating.
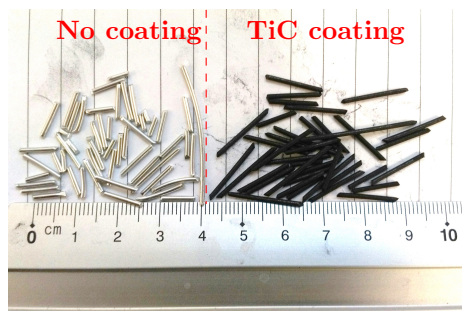
(b) 5183 granules without coating are shown to the left, the 5183 granules with black TiC-coating are shown to the right.

Figure 33: Equipment used in TiC-coating procedure, and appearance of the non-coated/coated 5183 granules.

The TiC-nanoparticles were produced by **US Research Nanomaterials Inc.**, and had diameters around 50 nm. Scanning electron microscopy (SEM) images of the coated granules may be found in section B in the appendices.

3.2 Equipment and Methods

3.2.1 Screw extrusion

A laboratory prototype metal continuous screw extruder (patent: [67]), was used to produce the different wires. The screw rotates counterclockwise, and extrudes the wire horizontally out at its front. A photograph of the screw extruder, with inserted part designations, is included in Figure 34.
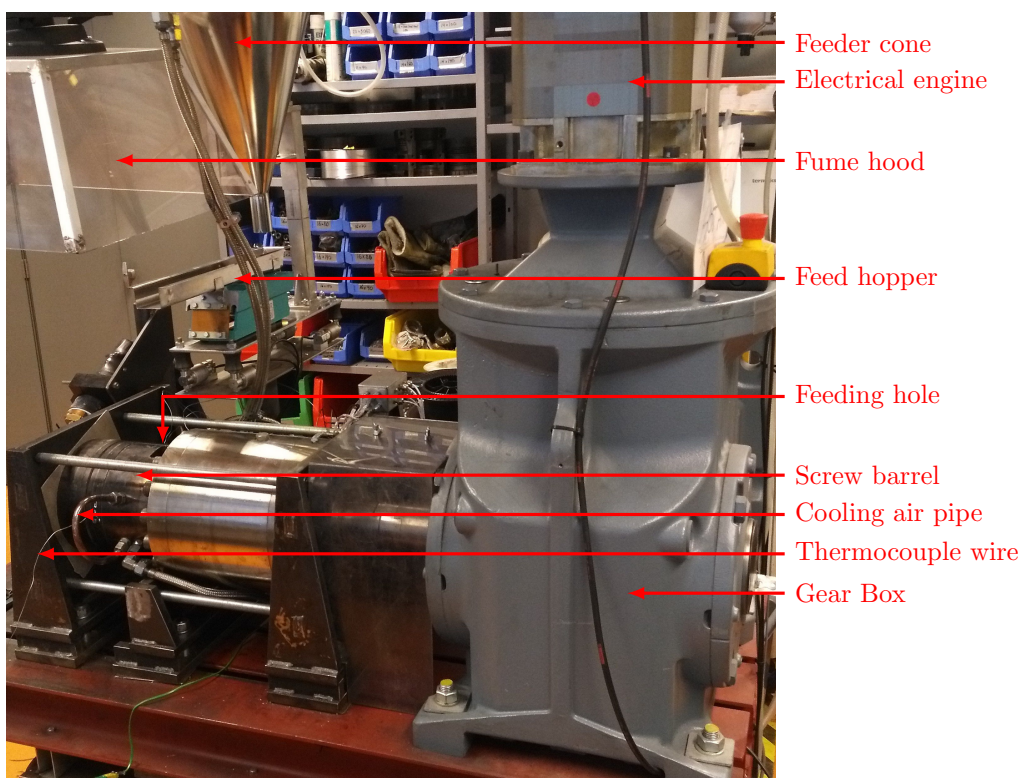
Figure 34: Side view of screw extruder.

An image of the screw extruder front (during screw extrusion) is shown in Figure 35.
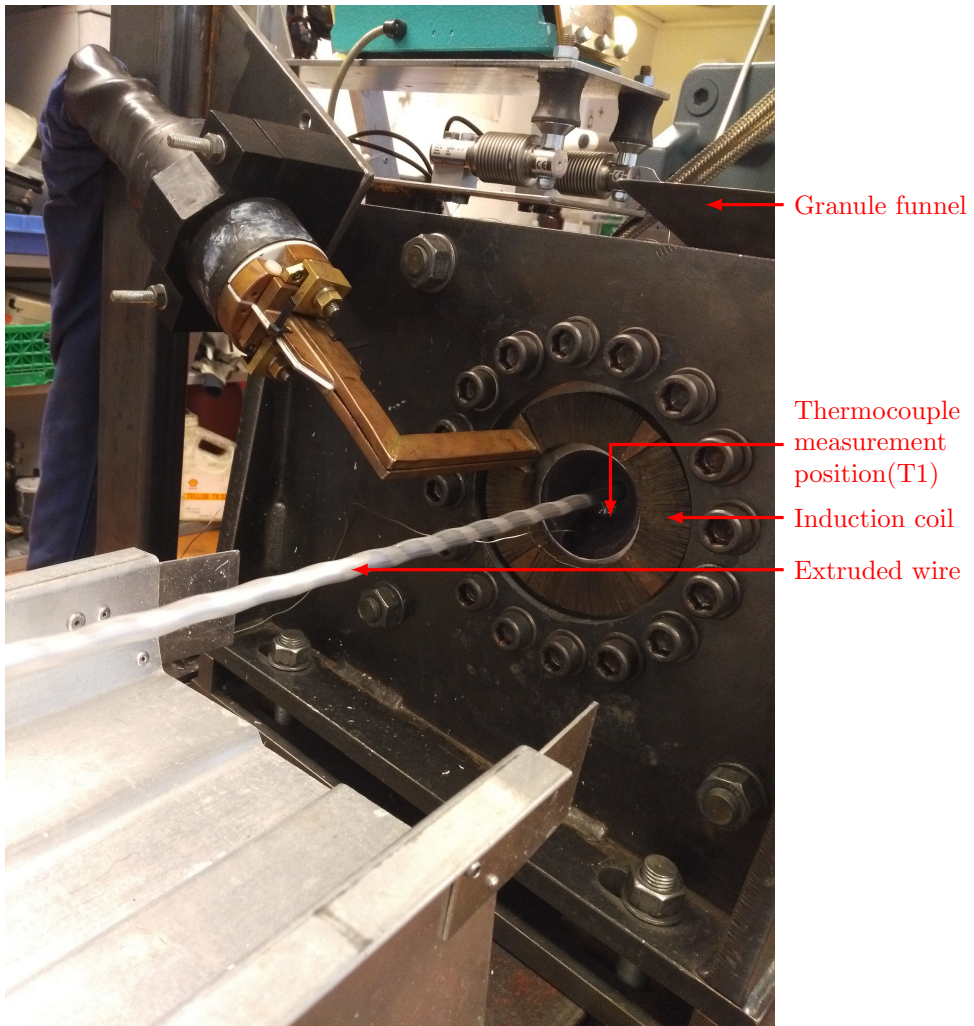
Figure 35: Close-up image of the screw extruder front during extrusion of the approx. 9.8 mm 4043+5183TiC wire, using a single flight screw.

The internal die opening was measured to be ≈ 10 mm in diameter. The internal tooling diameter (diameter of the metal plug at the front of the screw) was measured to be ≈ 34 mm for the 4043 and 5183TiC+4043 wires. For the other wires, the internal tooling diameter was increased to ≈ 43 mm due to accidental damages inflicted to the die in other experiments, while the internal die diameter remained ≈ 10 mm. A photograph of the damaged die, after it had been mechanically restored (using a lathe), is included in Figure 36.
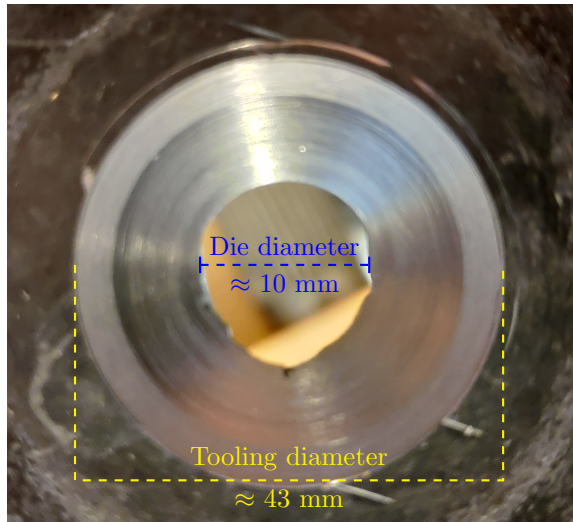
Figure 36: Photograph of the damaged, non-circular screw extruder die. As indicated by the glossy surface, an attempt to mechanically restore the die was made, by the use of a lathe.

Ideally, the die opening should be circular to avoid anisotropic properties in the extruded material. The damages also resulted in some scratches and defects along the surface of extruded wires. As seen in the image above, the die opening is larger in the vertical direction, than in the horizontal direction. The extruded wire will have the same, "elliptical" cross sectional shape.

The extrusion ratio (ER) during MCSE may be estimated as the cross sectional area of the internal tooling divided by the cross sectional area of the die opening, and gives an indication of the reduction in area which occurs through the die. Since the die diameters varies for the different wires, two distinct extrusion ratios are estimated. For the 4043 and 4043+5183TiC wires, which were screw extruded using the single flight screw, the extrusion ratio (designated as ER_{SF}) is given as:

$$ER_{SF} = \frac{\pi \cdot \left(\frac{34}{2}\right)^2}{\pi \cdot \left(\frac{10}{2}\right)^2} = \frac{34^2}{10^2} \approx 12 \tag{17}$$

Since the die used to produce the other wires was not circular (as shown in Figure 36), the diameter is not constant. The smallest diameter measured ($\approx 10\,\text{mm}$) is chosen for the estimation of the die diameter, as this gives the largest reduction in area. For the remaining wires, which were screw extruded using the double flight screw, the extrusion ratio (designated as ER_{DF}) is:

$$\text{ER}_{\text{DF}} = \frac{\pi \cdot \left(\frac{43}{2}\right)^2}{\pi \cdot \left(\frac{10}{2}\right)^2} = \frac{43^2}{10^2} \approx 18 \tag{18}$$

A slowly rotating drum, shown in Figure 37, was used to collect the extruded wire.
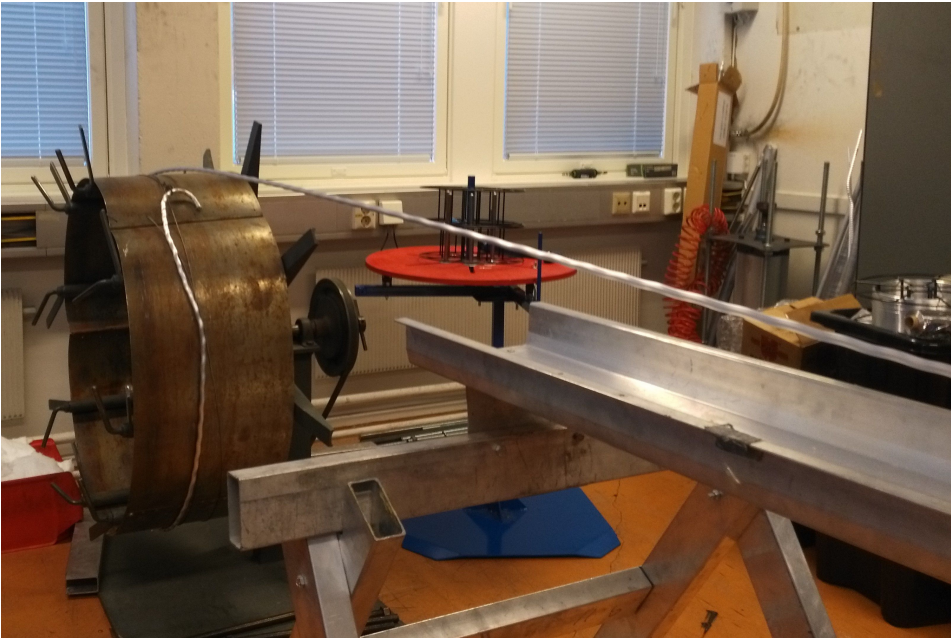
Figure 37: Drum used to collect extruded wire. The wire in this image is the 4043 wire, produced with a single flight screw.

An important parameter during screw extrusion is the temperature in the screw extruder system. The temperature was logged using a total of six thermocouples wire at different positions in the screw extruder. The designation and position of each thermocouple (T1 – T6) is presented in Figure 38.
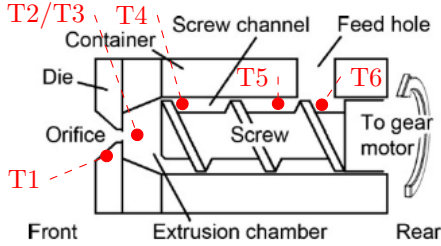
(a) Side-view schematic drawing of the screw extruder, including the designation of essential parts (black) and the placement of the thermocouples (red). Figure from [65].

(b) Placement of the temperature sensors in the screw extruder.

Temperature sensor	Placement
T1	Die
T2	Extrusion chamber left
T3	Extrusion chamber right
T4	Screw channel front
T5	Screw channel rear
T6	Screw stem

Figure 38: Position and designation of temperature sensors in the screw extruder.

Before extrusion could start, the screw extruder was pre-heated to avoid thermal cracking. The heating was done by placing a copper induction coil at the front of the screw (as shown in Figure 35), close to, but not in contact with the die. The effect of the coil was adjustable, but was mostly kept in the range 2-6 kW, depending on temperatures conditions.

In an attempt to avoid oxidation of the Al-Mg wire, chemically pure CO_2 gas from a bottle at 3 bar pressure was introduced to the screw chamber for the extrusion of the 5183-CG and 5183TiC-CG wires. This was done by flushing CO_2 through a tube connected to the hopper feeder of the extruder module (see Figure 39). Since CO_2 is $\approx$ 1.5 times denser than air [76], it was believed that the CO_2 gas would settle at the bottom in the screw chamber, create a CO_2 rich (but still containing air) atmosphere and thus reduce the oxidation of the Al-Mg wire during screw extrusion.
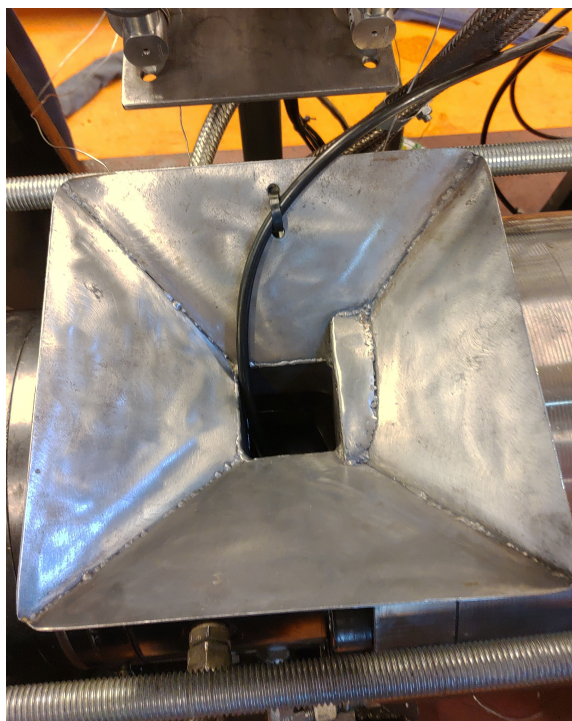
Figure 39: CO_2 transporting tube, connected to the granule funnel of the screw extruder. The tube flushed CO_2 gas (from a bottle at 3 bar) into the rear end of the screw chamber.

When CO_2 was used, the compressed cooling air (at 4.5 bar) was not applied until deemed necessary, which was when the rear temperatures (T5 and T6 in Figure 38) reached around 280°C. Although the compressed air passes through cooling ribs separated from the screw extruder chamber, it was omitted in an attempt to minimise turbulent airflow within and around the screw extruder chamber and thus keep the CO_2 gas in the screw chamber.

Important process parameters (temperature, screw momentum, screw rotation speed, air-pressure and approximate feeding rate, etc.) were measured and logged using the software `Labview`. In an attempt to obtain fast, but stable extrusion, the granule feeding rate, the effect of the induction coil and the rotation speed of the screw were adjusted accordingly throughout the experiment.

After the experiments were stopped, the screw extruder module was disassembled, the metal plug remaining at the front of the screw was removed and the parts which contained Al residue were etched in a basic sodium hydroxide solution.

An overview of the complete screw extrusion experimental procedure is included in Figure 40 [65].
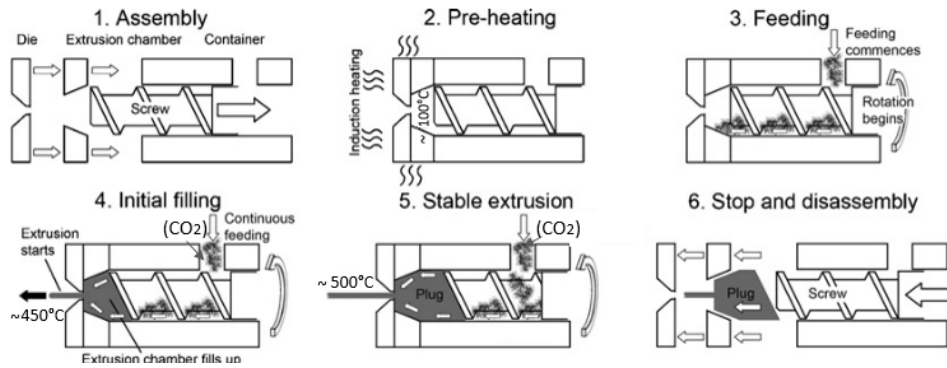
Figure 40: Illustration of the different experimental steps in the screw extrusion procedure, showing the approximate temperatures in selected processing steps. When producing the 5183-CG and 5183TiC-CG wires, CO_2 gas was added through a transporting tube attached to the granule funnel in the feeding hole. Modified from [65].

3.2.2 Sample preparation

To measure the microhardness and observe the microstructure of the extruded wires, multiple samples of each wire were prepared as described in this section.

About 12 cm long pieces from each extruded wire were cut using a bolt cutter. Using a *Struers Labotom-5* water-cooled saw, the pieces were further cut into 1-3 cm long pieces. The wire pieces were then cast in *Epofix* epoxy-resin. To remove air bubbles from the resin, the samples were held at 0.3 bar for five and a half minutes in a *Struers Citovac* vacuum chamber, before the resin was allowed to harden for a minimum of eight hours.

The planes of interest in the samples are the transverse cross sections and the longitudinal cross sections of the wires, as indicated in Figure 41.
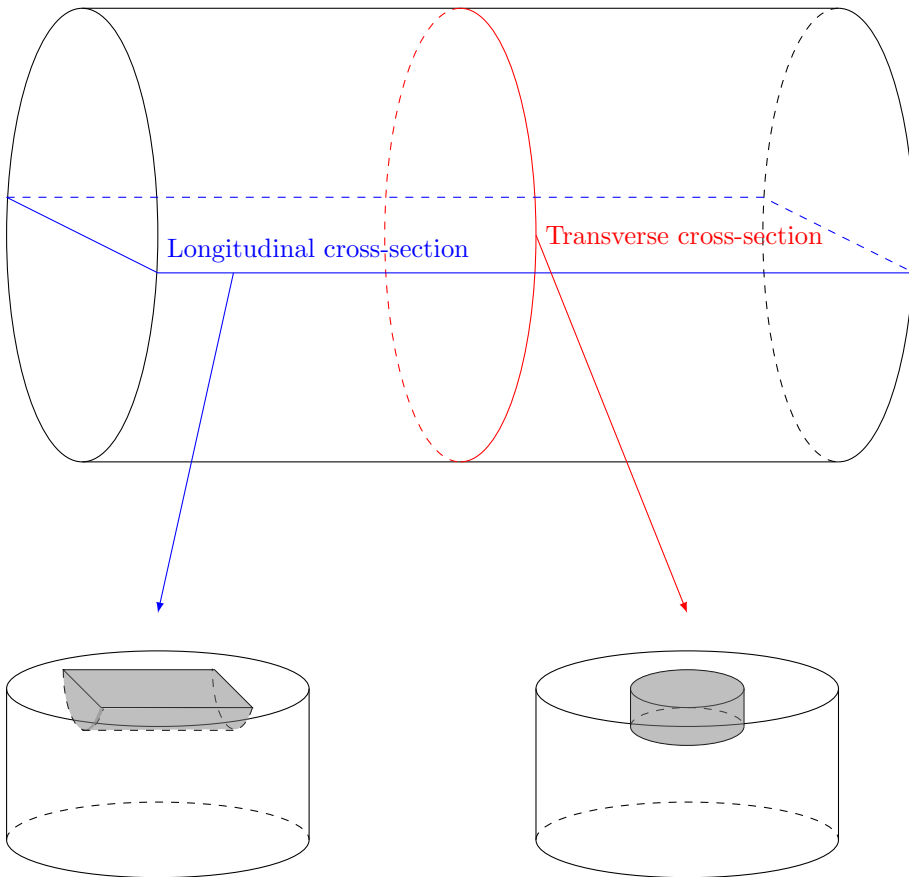
Figure 41: Sketch of the investigated wire planes and corresponding mounting/cast geometries.

To reach the longitudinal and transversal cross sections shown in Figure 41, the samples were grounded and polished using the procedure shown in Table 5:

Table 5: Polishing procedure. The duration of each step varied from sample to sample, depending on visual observations.

Step	Surface	Suspension/Lubricant
1	SiC FEPA#320	Water
2	MD-Largo 9µm	Diapro All/Lar.
3	MD-mol 6µm	Diapro Mol
4	MD-mol 3µm	Diapro Mol
5	MD-NAP 1µm	Nap-B/NAP-R (depending on availability)

The initial polishing was done using a semi-automatic combined polisher (*TegraPol-31*) and load applier (*TegraForce-5*). The polishing machine is shown in Figure 42a. The two different sample holders used, referred to as sample holder 1 and 2 are shown in Figure 42b and Figure 42c, respectively.

(b) Sample holder 1.

(c) Sample holder 2.

(a) *Struers TegraPol-31/TegraForce-5.*
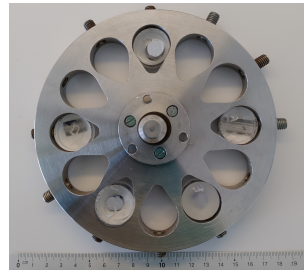
Figure 42: Equipment used for sample preparation.

The 5183TiC+4043 and 4043 wires were polished using sample holder 1, the remaining wires with sample holder 2. The different sample holders resulted in no visual differences in the appearance of the samples. To achieve a flat polishing plane on the samples, dummies of pure resin were placed in each empty position around sample holder 1, while the samples in sample holder 2 were placed around the holder as shown in Figure 42c.

Before each polishing step, the sample holder (and samples for holder 2) was cleaned in the *Strues Lavamin* ultrasonic water-cleaner (Figure 43a), while the sample and the dummies in sample holder 1 were rinsed with tap-water and cleaned in the *VWR Ultrasonic cleaner* (seen in Figure 43b, filled with distilled water).

(a) *Strues Lavamin.*

(b) *VWR Ultrasonic cleaner.*

Figure 43: Ultrasonic cleaners.

After the polishing procedure in Table 5 was finished, the samples were further polished using a *Vibromet 2* vibratory polisher (produced by *Buehler*, seen in Figure 44a). Samples were mounted in a holder (shown in Figure 44b), weighing $400\,\mathrm{g}$, which pushed the sample down towards the vibrating plate) and polished for one to two hours in a colloidal *Buehler MasterMet 2* suspension, containing $0.02\,\mu\mathrm{m}$ SiO_2 particles. After 1 hour in the vibratory polisher, the samples were taken out and washed with water and ethanol, then dried using a hairdryer. This procedure produced a plane sample surface, free of scratches and deformations.
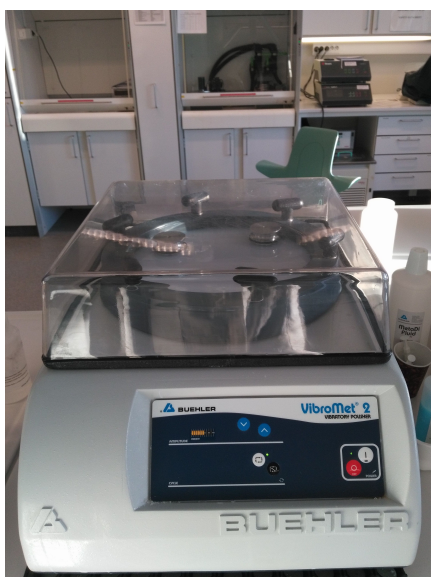
(a) *Buehler Vibromet 2* vibratory polisher.

(b) Sample holder for vibration polishing, weighing 400 g, containing a longitudinal 4043 single flight-wire sample.

Figure 44: Vibration polising equipment.

Investigation of the sample surfaces in the scanning electron microscope revealed that some of the SiO_2 particles from the vibration polishing suspension remained on the surface. In an attempt to remove these particles, some of the 5183TiC and 5183TiC-CG samples were vibration polished in distilled water for one hour, before they were rinsed in an ethanol solution in the *VWR Ultrasonic cleaner* for 30 minutes. This was determined to be successful only for the 5183TiC wire, as the other 5183TiC-CG wire samples were surface contaminated by Cu clusters through this procedure. It is believed that the presence of Cu on the samples was a result of tap-water contamination of the polishing pad used in the vibratory polisher.

The samples intended for scanning electron microscopy (SEM) examination were required to have electrical conductivity from the metallic wire-surface to the backside of the epoxy sample, so that electrons which do not contribute to the imaging are led away. This will minimise charging effects in the image. To achieve conductivity to the backside of the samples, two different approaches were taken. One approach was to ground the backside of the sample with coarse SiC-paper (first #120, then #320) until the rear end of the wire-piece in the epoxy cast was reached. This approach was used for the transversal cross-section samples of the DF screw extruded wires. To illustrate this procedure, a transversal SEM sample of the 5183 wire is shown before and after grinding in Figure 45.
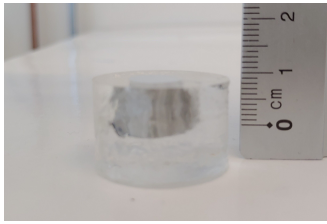
(a) Before.
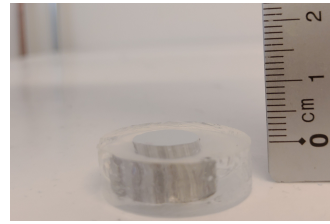
(b) After

Figure 45: Grinding of transversal cross-section SEM sample of 5183 wire.

The second approach was to cover the samples with aluminium foil, so that electrical conductivity was achieved from the wire surfaces to the backside of the epoxy sample. The longitudinal cross-section samples (as well as the transversal cross-section samples of wires 4043 and 4043+5183TiC) were covered by aluminium foil from top to bottom, as shown in Figure 46.

The SEM samples were kept in a heating cabinet at 65°C for degassing at least 12 hours before each SEM session. Based on availability, two different SEM sample platforms were used. Figure 46a shows a transverse cross-sectional sample on a sample platfrom, Figure 46b shows a longitudinal cross-sectional sample in a SEM sample cup holder.
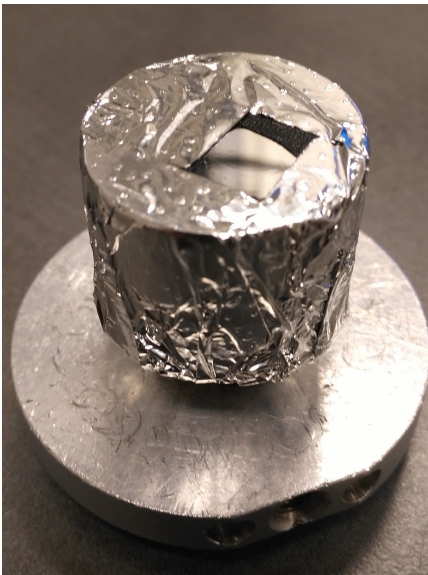
(a) Transverse cross-section sample of wire 4043+5183TiC, on SEM sample platform.
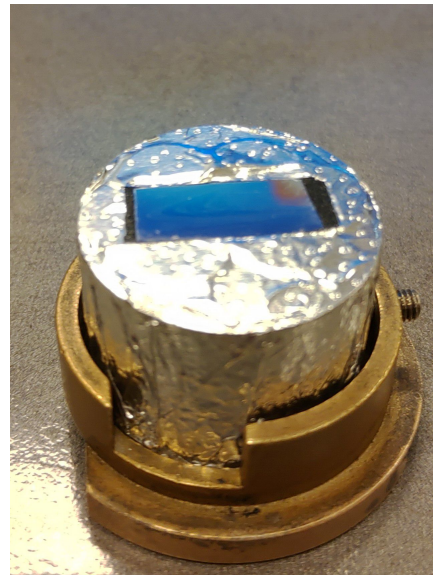
(b) Longitudinal cross-section sample of wire 4043+5183TiC, in SEM sample cup holder.

Figure 46: Samples of wire 4043+5183TiC wire, prepared for SEM imaging.

The purpose of the sample holder is to ensure electrical conductivity from the sample to the SEM stage, so that excess electrons which do not contribute to imaging the sample are led away from the sample surface. The use of different sample holders did not result in observable differences in the observed image quality.

3.2.3 Microscopy images

Electron microscopy images were taken using a *Zeiss Supra 55-VP* low vacuum field emission scanning electron microscope (LVFESEM). This microscope is equipped with secondary and backscattered electron detectors. The samples were qualitatively analysed using energy dispersive X-ray spectroscopy (EDS) in the same microscope, with an *EDAX* EDS unit and the software `EDAX Team`.

Unfortunately, the backscattered electron detector in the *Zeiss Supra 55-VP* was out of order for the duration of this work. Therefore, all SEM images were taken with the secondary electron detector. Secondary electrons only image the surface of the sample since they are emitted from the surface and only slightly beneath it, i.e they have low emission volumes. Since the emission volume of EDS-signals and backscattered electrons match better than EDS-signals and secondary electrons, the EDS analysis throughout this work was not optimal with regards to the comparison between EDS-signals and electron imaging.

Optical microscopy images were mostly taken using a *Zeiss AXIO* inverted microscope and post-processed using the software `Zen Core`. Low magnification microscopy images at 10X magnification) were taken using *Leica CTR6000*, by stitching together approximately 140 images at 100X magnification. The software `Leica Application Suite (LAS) Core` was used to stitch the images together.

3.2.4 Electron back scatter diffraction

Electron backscatter diffraction (EBSD) analysis of was done using the *Zeiss Ultra 55* SEM. The sample stage was inclined at 70°, the working distance was ≈ 25 mm and the acceleration voltage was 25 kV.

The electron backscatter diffraction patterns were collected using the software `NORDIF` developed by Prof. Jarle Hjelen (NTNU), indexed and mapped using `OIM Data collection 7` and analysed using the software `TSL OIM Analysis™` (both developed by *EDAX*).

3.2.5 Microhardness measurement

The Vickers microhardness ($HV_{0.1}$) of each a transversal sample of each wire was measured using the *Leica VMHT MOT* hardness measurement device (seen in Figure 47a). An indentation force of 100 grams, and a dwell time of 15 seconds was used. To avoid faulty measurements, a distance between the indents was at least 6 times the mean indent-diagonal (corresponding to 200-300 µm) was used. The indents were applied along the diameter of the transversal cross-sectional samples, from top to bottom (relative to the screw extruder). Approximately 25 indentations were used for each wire. The indentation force for all measurements was 0.98 N.

The results from the microhardness testing were post-processed using `Microsoft Excel`.

3.2.6 Tensile testing

Tensile tests were performed using a **Multipurpose servohydraulic universal testing machine** (series LFV 100 kN), produced by *Walter + Bai AG*. The tensile testing machine is shown in Figure 47b. A strain rate of $1.8\,\text{mm}\,\text{min}^{-1}$ (corresponding to $10^{-3}\,\text{s}^{-1}$) was applied. The extensiometer (produced by *Epsilon technology*), had a gage length of $25\,\text{mm}$ for all tensile tests.

The tensile data was gathered with the software `DION 7`, developed by *Walter+Bai AG*, and post-processed using `Python`.
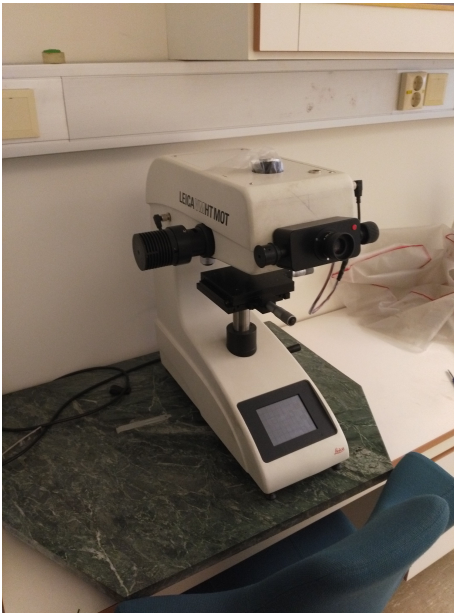
(a) *Leica VMHT MOT* microhardness measurement device, used to measure the Vickers microhardness ($HV_{0.1}$) of the different wire samples.

(b) *Walter + Bai* Universal Testing Machine, used for tensile testing of wire samples.

Figure 47: Equipment used for microhardness measurements and tensile testing of the extruded wires.

The tensile "dogbone" samples were obtained by machining approximately 10 cm long wire pieces cut off the extruded wires. The tensile load was thus applied parallel to the extrusion direction. The dimensions of the samples depended on the geometry of the extruded wire. The 4043 and 4043+5183TiC wires were wave-like due to the asymmetric pressure generation caused by the single flight screw material. Therefore, these "wavy" single flight tensile samples had smaller dimensions than the "straight" double flight tensile samples, since more material had to be removed to create straight samples. The dimensions for the single flight (4043+5183TiC and 4043) and double flight (others) tensile specimens are included in, respectively, Figure 48a and Figure 48b.
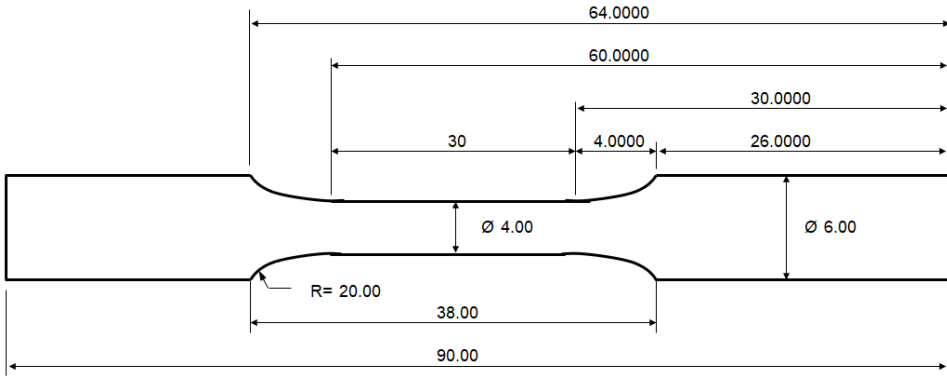
(a) Single flight.
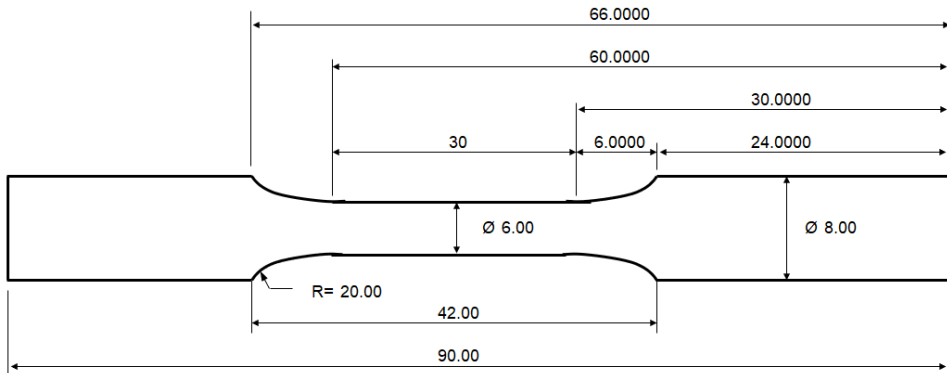
(b) Double flight.

Figure 48: Tensile test specimen dimensions. All numbers are in mm.

As seen in Figure 48, the diameter of the investigated samples was either 4.0 or 6.0 mm, so that surface defects and pores present in the extruded ≈ 9.8 mm wires were not likely to affect the outcome of the tensile tests. The strain measurement length was 30 mm for all samples.

Typical appearances of two single flight wires and one double flight wire are shown in, respectively, Figure 49a and Figure 49b. Figure 49a also shows the macroscopic difference between single flight wires extruded at low and high extrusion speed.
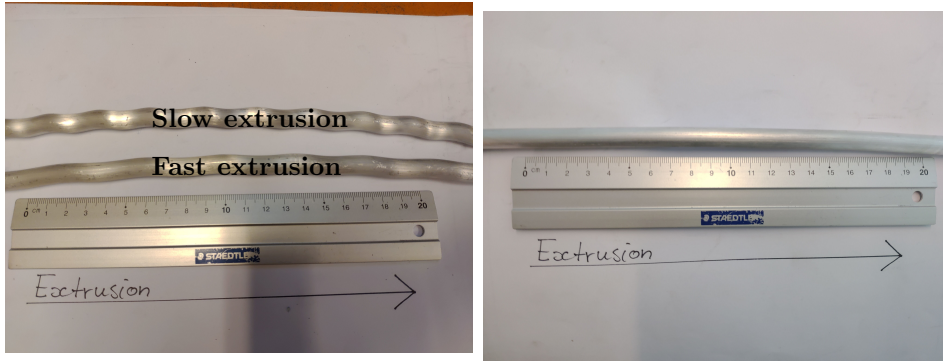
(a) Single flight 4043+5183TiC wire pieces. The lower wire piece was extruded at a higher extrusion speed than the upper wire piece.

(b) Double flight pure Al wire.

Figure 49: Typical appearance of extruded wires, showcasing the difference between wires extruded by single and double flight screws.

As seen from Figure 49 above, wires produced using double-flight screws are more straight than the ones produced using single-flight screws. The double-flight wires are therefore more suitable for further processing (rolling and drawing).

The samples for the tensile tests of the 4043+5183TiC and 4043 wires were prepared by Finmekanisk verksted at NTNU. The other, double-flight samples were prepared by Sintef Industry.

Unfortunately, the elongation under tensile loads was measured precisely only for some of the specimens, due to connectivity issues between the extensiometer and the software used. Therefore, the tensile results presented in subsection 4.7 only shows the measurements of representative samples, i.e samples that fractured within the extensiometer measuring range, had similar behaviour to the other samples and for which the strain was accurately measured.

4   Results

The measured temperatures during screw extrusion, results from microstructural SEM and EBSD analysis, and the measured mechanical properties of the double flight (DF) screw extruded wires, i.e. the 5183, 5183TiC, 5183-CG and 5183TiC-CG wires, are presented in this section. Results from the investigations of the single flight (SF) screw extruded wires (4043 and 4043+5183TiC) may be found in section C in the appendices. The DF wires differ in presence of TiC, atmosphere during screw extrusion (air/CO_2) and pre-treatment of granule raw material (with or without water rinsing), as shown in Figure 30 and Table 4 in the experimental procedures (section 3).

4.1 Temperature during screw extrusion

An important parameter to consider when investigating the microstructure and mechanical properties of the extruded wires is the processing temperature during screw extrusion. The measured temperatures during double flight screw extrusion wires are shown in this section.

The temperature evolution during screw extrusion of wires 5183 and 5183TiC, produced from water-rinsed granules and extruded in ambient atmosphere, is presented in Figure 50.
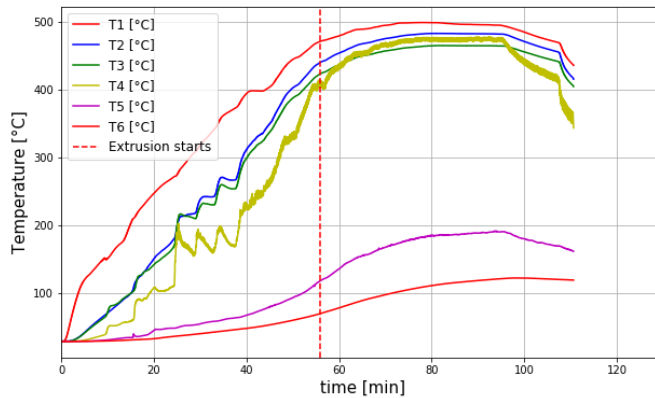
(a) 5183 wire.
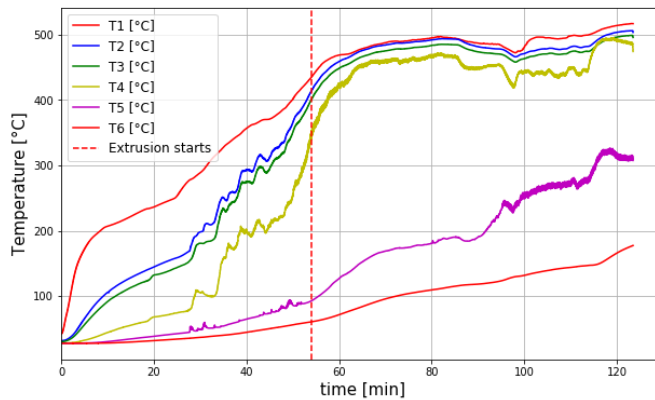
(b) 5183TiC wire.

Figure 50: Temperature evolution during screw extrusion in ambient atmosphere. The dashed, red, vertical line indicates the start of the extrusion. The different temperatures correspond to thermocouple measurement in the following positions: T1: Die T2: Extrusion chamber left T3: Extrusion chamber right T4: screw channel front T5: Screw channel rear and T6: Screw stem.

The position of each temperature measurement (T1 – T6) may be found in Figure 38.

The temperature evolution during screw extrusion of wires 5183-CG and 5183TiC-CG, produced from 5183-granules not rinsed in water and extruded in CO_2 atmosphere, is presented in Figure 51.
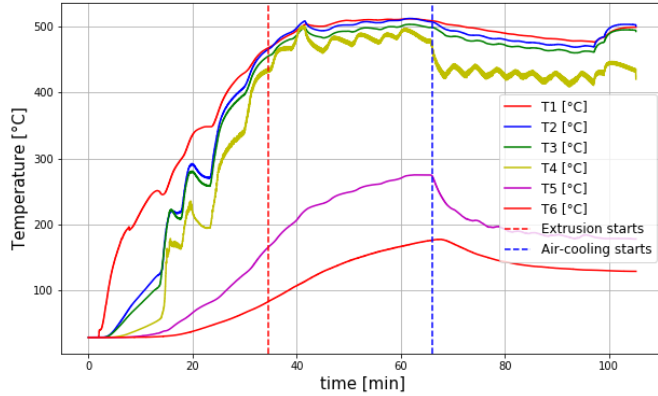
(a) 5183-CG wire.
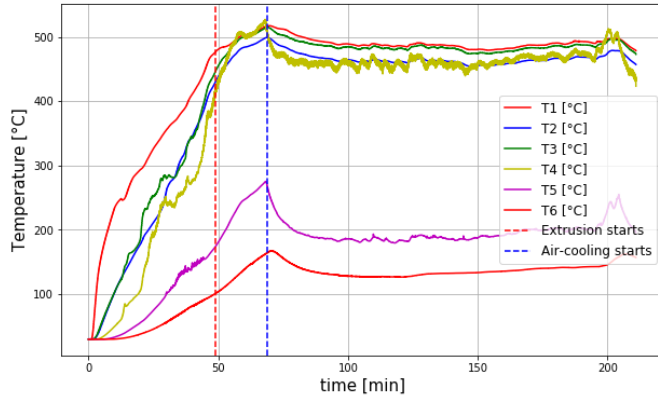
(b) 5183TiC-CG wire.

Figure 51: Temperature evolution during screw extrusion in CO_2 atmosphere. The dashed, red line indicates when screw extrusion started, the dashed, blue line indicates when cooling (by compressed air flow) was initiated. Note that the horizontal time-axes in the two plots differ. The position of the temperature measurements are as follows: T1: Die, T2: Extrusion chamber left, T3: Extrusion chamber right, T4: screw channel front, T5: Screw channel rear, T6: Screw stem.

From Figure 50 and Figure 51, it may be observed that the extrusion of all wires started at T1≈450°C.

4.2 Optical microscopy images

In this section, optical images of the cross-section wire-samples are presented.

Optical microscopy images of the transversal cross sections of each wire are shown in Figure 52.
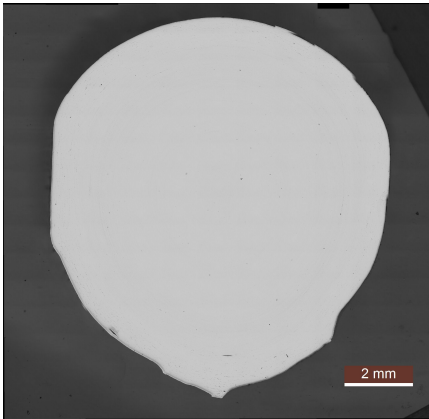
(a) 5183.
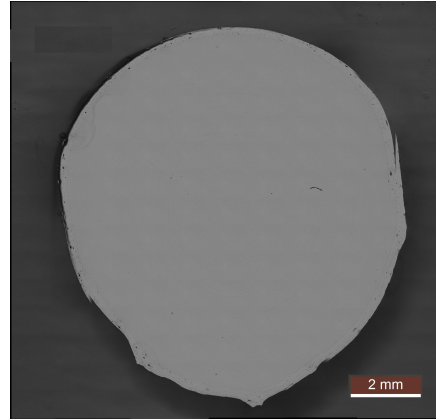
(b) 5183TiC.
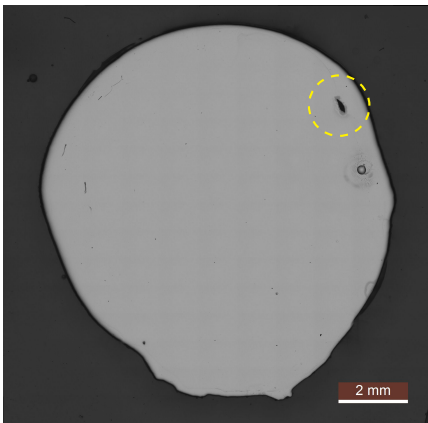
(c) 5183-CG.
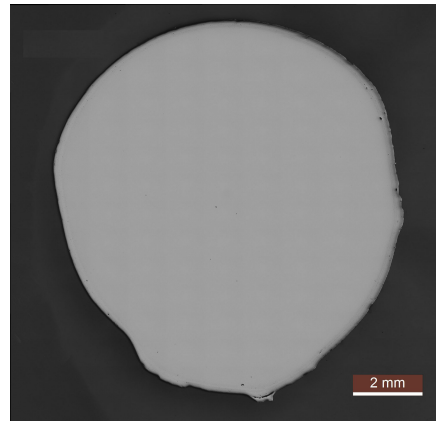
(d) 5183TiC-CG.

Figure 52: Optical microscopy overview images of the transversal cross sections of each wire, showcasing the irregular elliptical shape of the extruded wires caused by the damaged extrusion die (see Figure 36). Some pores may be seen around the circumference of all wires. The large crack inside the dashed yellow circle in (c) is most likely a consequence of insufficient compaction in the screw extruder.

The irregular cross-sectional shape of the wires is caused by the damages in the die opening. The damaged die may be seen in Figure 36.

Optical micrographs of the longitudinal cross section samples of the wires extruded in ambient atmosphere (produced from granules rinsed with water and heat-treated at 130°C and 350°C) are presented in Figure 53.
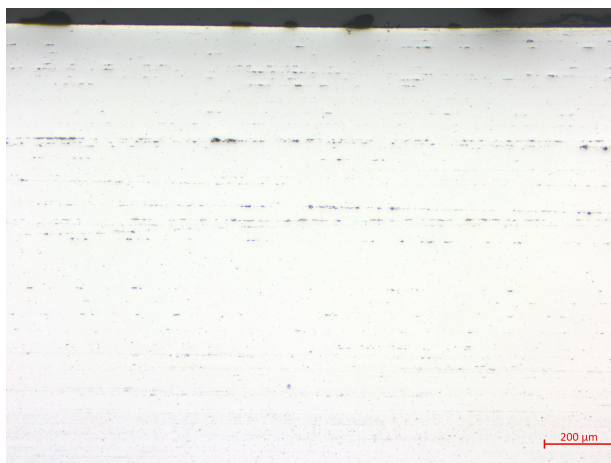
(a) 5183.
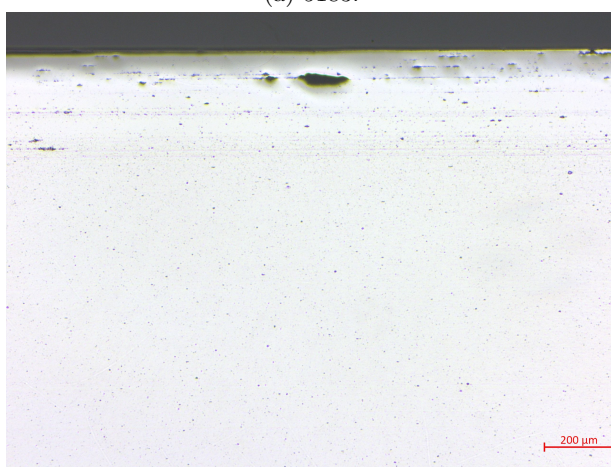
(b) 5183TiC.

Figure 53: Optical microscopy images of the longitudinal cross section of wires extruded in ambient atmosphere. These wires were produced from granules rinsed with acetone and water, and heat treated at 130 and 350 °C.

Corresponding images for the wires extruded in a CO_2-rich atmosphere (produced from granules not rinsed with water and heat-treated only at 130°C) are shown in Figure 54.

(a) 5183-CG.
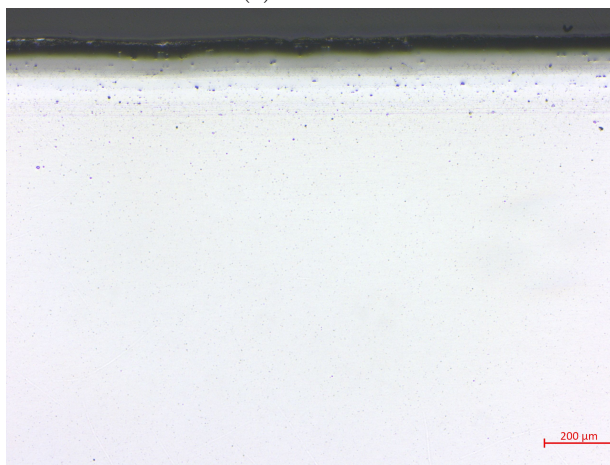
(b) 5183TiC-CG.

Figure 54: Optical microscopy images of the longitudinal cross section of the wires extruded in a CO_2-rich atmosphere. These wires were produced from granules heat treated only at 130°C and rinsed without water.

By comparing Figure 53 with Figure 54, it may be seen that the porosity (pores are visible as dark spots of varying sizes) is significantly higher in the surfaces of the 5183 and 5183TiC wires, than in the 5183-CG and 5183TiC-CG wires. The 5183 and 5183TiC wires were produced from acetone and water-rinsed granules, which were heat-treated at 130 and 350 °C, and extruded in ambient atmosphere. The 5183CG and 5183TiC-CG wires were produced from aceton-rinsed granules, which were heat-treated only at 130 °C, and extruded in a CO_2-rich atmosphere. The different pre-treatment and screw extrusion procedures for the wires shown in the image above are shown in Figure 30. Some pores were found in the surfaces of all the wires, but the different pre-treatment parameters and/or use of a CO_2 cover gas has a clear effect, for both the composite TiC-wires and the monolithic alloys.

The porosity difference is also clearly visible in optical microscopy images of the transversal cross-section samples of the composite wire, shown in Figure 55.
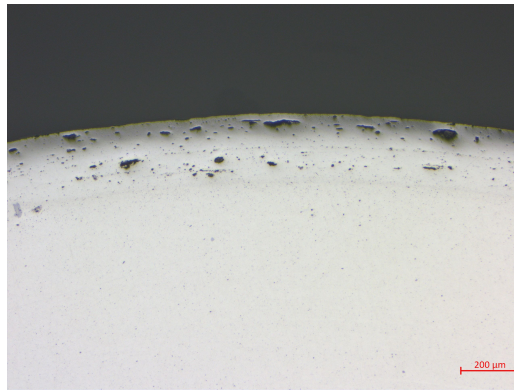
(a) 5183TiC.
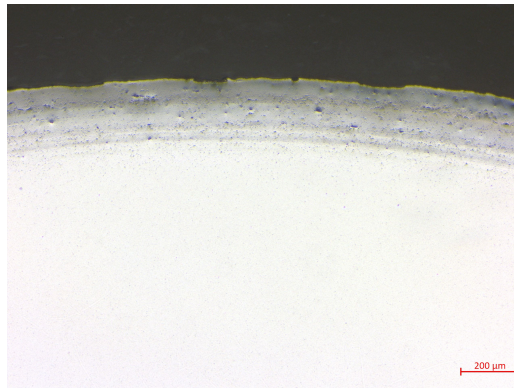
(b) 5183TiC-CG.

Figure 55: Optical microscopy images of the transversal cross section samples of the TiC-AMC wires, showing a cross-section of the wire surface. It may be observed that the 5183TiC wire is significantly more porous than the 5183TiC-CG wire.

70

4.3 Investigation of cracks and pores in extruded wires

The SEM images in this section present cracks and pores found near the surfaces of the extruded wires. It was observed that deep cracks were present in both the 5183TiC and the 5183TiC-CG wire. Two similar cracks from the 5183TiC and the 5183TiC-CG wires are shown, respectively, in Figure 56a and Figure 56b.
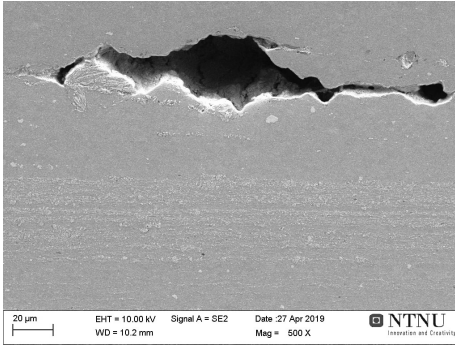
(a) 5183TiC.
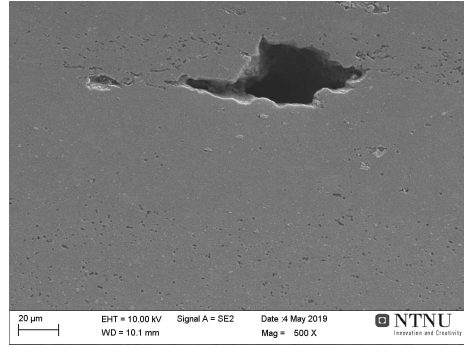
(b) 5183TiC-CG.

Figure 56: Secondary SEM micrographs showing pores near the surface of the longitudinal TiC-nanocomposite wire samples. The samples are oriented so that the extrusion direction is horizontal in the images.

The alternating grey-layer structure seen in the lower parts of Figure 56a was found to consist of oxides, as shown in section D in the appendices.

A crack of the same appearance was also found in the transversal 5183TiC wire sample shown in Figure 57a. The more shallow pore to the right in Figure 57a is imaged at higher magnification in Figure 57b.
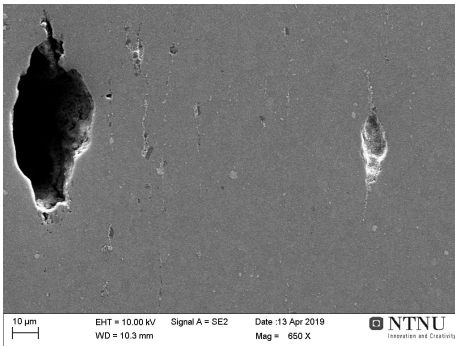
(a) Transversal 5183TiC sample.
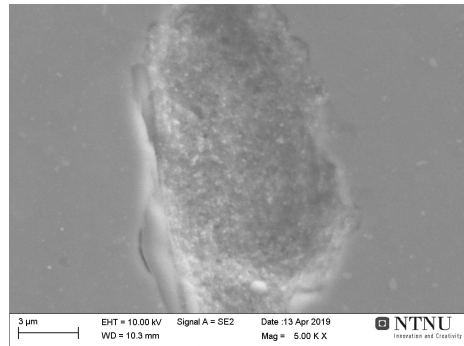
(b) Higher magnification image of shallow pore.

Figure 57: Secondary SEM images from transversal cross section sample of 5183TiC wire, showing two different surface defects.

71

The results from the EDS mapping of the pore in Figure 57b are shown in Figure 58.
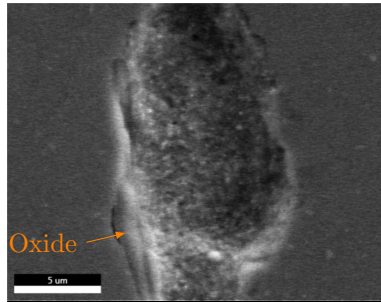
(a) Shallow pore in 5183TiC wire.
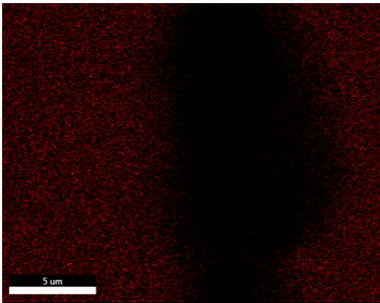
(b) Al EDS signals.
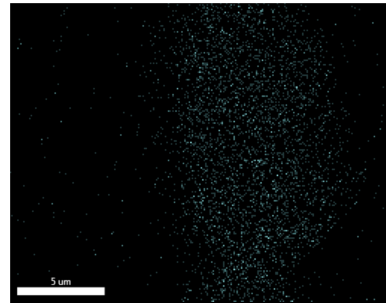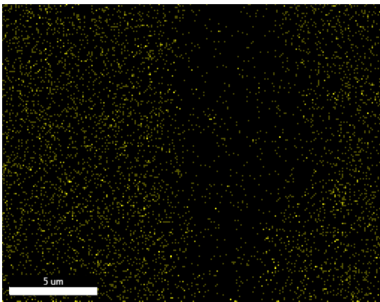
(c) Ti EDS signals.
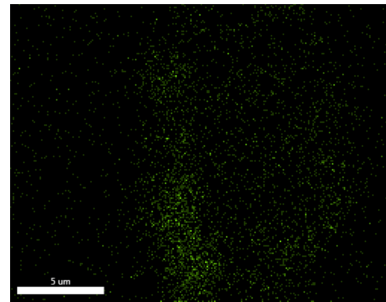
(d) Mg EDS signals.

(e) O EDS signals.

Figure 58: SEM and EDS analysis of pore near the surface of the 5183TiC wire.

Figure 58c shows that Ti signals agglomerate from within the pore shown in Figure 58a. It may also be noticed that characteristic O signals are emitted from the lower left edge of the pore, along with Mg signals. This implies the presence of a magnesium oxide (MgO or $MgAl_2O_4$).

4.4 Surface oxide in 5183TiC-CG wire

Oxides were also observed near the surface of the 5183TiC-CG wire. One of these surface-oxides are shown in Figure 59a, along with the EDS signals for Al, Ti, Mg and O (Figure 59b–Figure 59e).
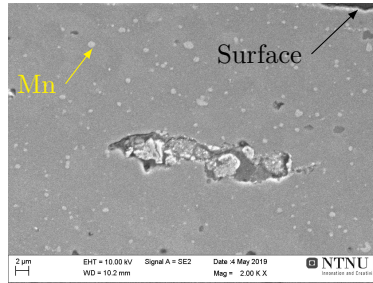
(a) Oxide near surface.
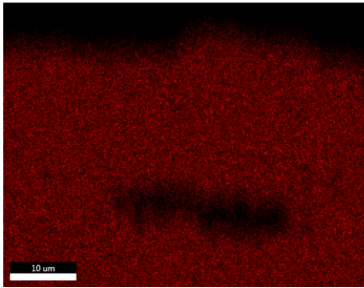
(b) Al EDS signals.
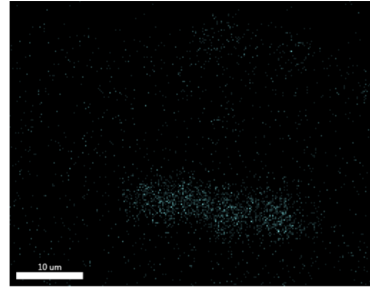
(c) Ti EDS signals.
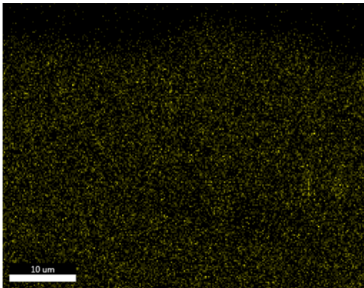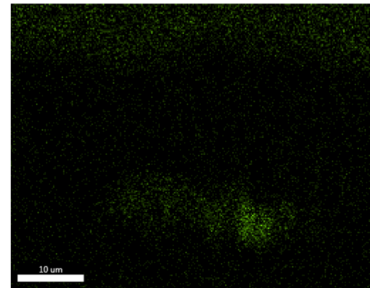
(d) Mg EDS signals.

(e) O EDS signals.

Figure 59: SEM and EDS analysis of an oxide phase in the 5183TiC-CG wire. The edge surface of the wire is visible in the upper right corner in (a). The grey phases in (a) bear resemblance to Mn precipitates.

Since no characteristic Al signals (seen in Figure 59b) are emitted from the phase in the centre of Figure 59a, while Mg signals in Figure 59d are, it may be assumed that this phase is mainly MgO. From Figure 59c and Figure 59e, it may be seen that Ti signals agglomerate in the same area as the O signals, indicating TiC particles within the oxide.

4.5 Distribution of TiC nanoparticles and oxides

SEM images of the 5183TiC and 5183TiC-CG wires, showing the distribution and morphology of the TiC nanoparticles and Mg-oxides present in the 5183-Al matrix, are included in the following subsections. EDS point analysis was used to confirm the identity of the different phases observed. The EDS spectra from this analysis may be found in section E in the appendices. It is assumed that there is no difference in TiC-distribution between the transversal and longitudinal cross-section samples, as they will both give a representative illustration of the cross-sectional the microstructure in the wires. All SEM images in this section are taken of areas close to the centre of the wire, so it may be assumed that they are representative for the microstructure of the bulk material.

4.5.1 5183TiC wire

A sample of the 5183-TiC wire (extruded without CO_2 cover gas) is imaged in this section. The sample was prepared as indicated in subsubsection 3.2.2, including vibration polishing in distilled water and ultrasonic rinsing in ethanol in order to remove residual SiO_2 from earlier vibrational polishing steps. A secondary SEM image of the matrix in the longitudinal cross section of the 5183TiC-wire is presented in Figure 60.
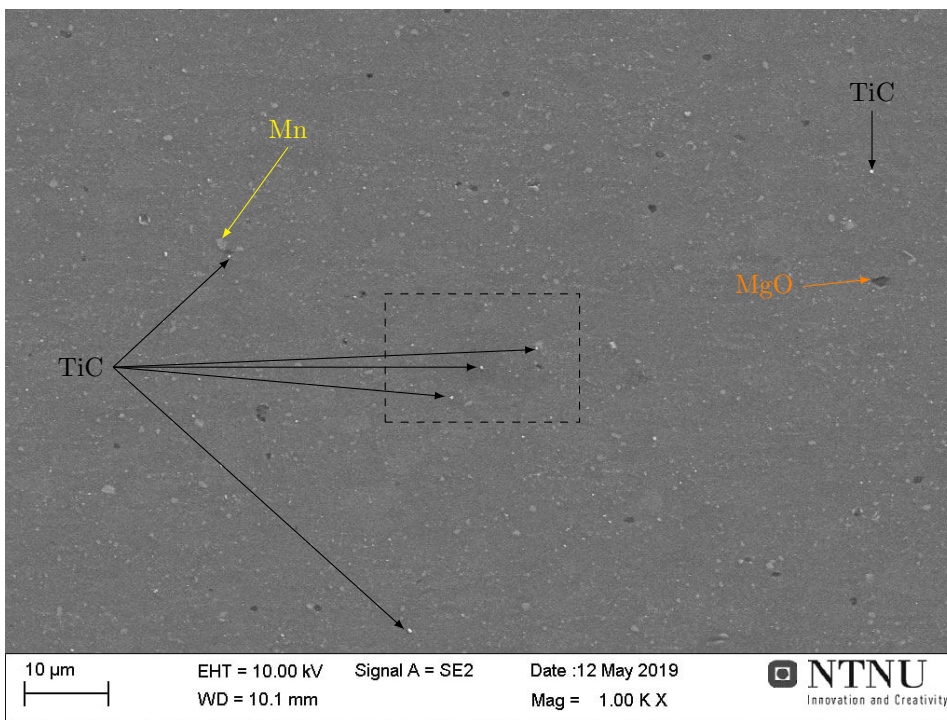
Figure 60: Secondary electron image of the 5183TiC wire (longitudinal cross section), showing the Al-matrix near the centre of the longitudinal cross-section sample. The inserted arrows show which phases were identified using EDS (see subsection E.1 in the appendices). The bright, white particles are TiC clusters, the light grey irregular shaped phases are Mn precipitates and the dark phases are MgO. The area within the dashed box is examined at higher magnification, shown in Figure 61.

As seen from Figure 60, multiple phases are present in the 5183TiC-wire. The inserted arrows indicate the phases which were identified using EDS, as shown in subsection E.1 in the appendices. The dark phase in the center right area of the image, indicated by an orange arrow, was confirmed to have a composition corresponding with MgO. The light grey phase in the center left of the image, indicated by a yellow arrow, was confirmed to be a Mn precipitate. The bright spots indicated by the black arrows are TiC nanoparticle clusters.

Phases and particles in the image with similar appearance to those indicate by the arrows, may be assumed to be of the same identity. Thus, all the small, bright particles seen in Figure 60 may be assumed to be TiC. It is clear that TiC is evenly (but rather scarcely) distributed in the area imaged in Figure 60, indicating that a uniform distribution of the nanoparticles was achieved through MCSE.

The area in the inserted, dashed box in the centre of Figure 60 is imaged at higher magnification in Figure 61.
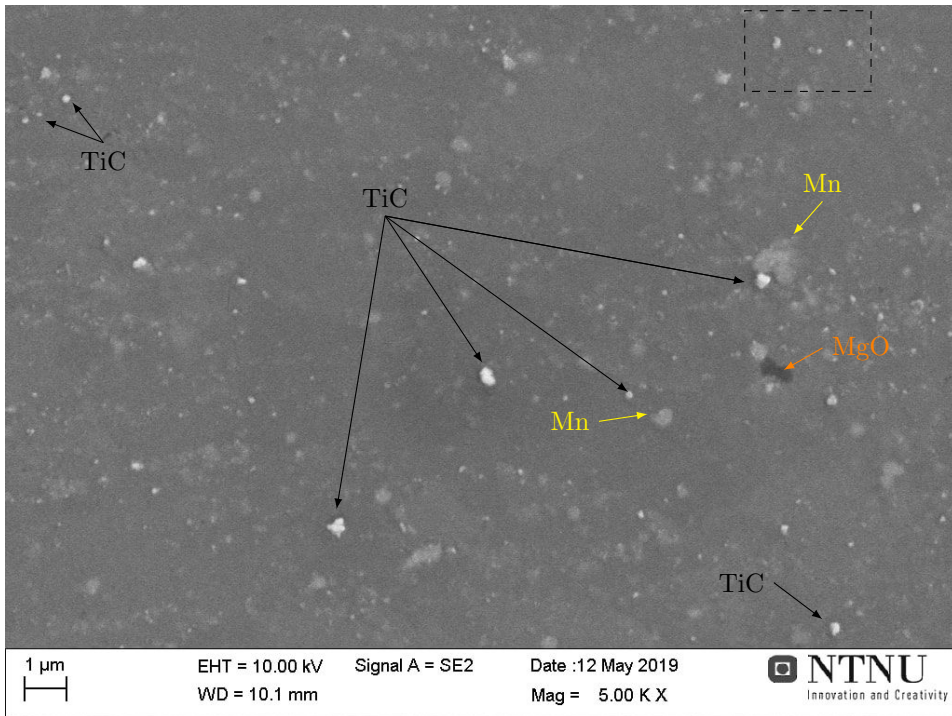

Figure 61: Secondary electron image of the longitudinal cross section 5183TiC wire sample, showing the Al-matrix in the centre of the longitudinal cross-section sample. The arrows show the identity of the different phases, confirmed by EDS analysis. The bright particles are TiC-clusters, the light grey phases are Mn-precipitates and the dark phase is MgO. The area within the dashed box is imaged at higher magnification in Figure 62.

Several smaller TiC particles were found in the area imaged in Figure 61, as shown by the black arrows, as well as additional Mn and MgO phases.

The area inside the dashed box in the top right corner of Figure 61, is imaged at higher magnification in Figure 62 to further investigate the appearance of the TiC particles.
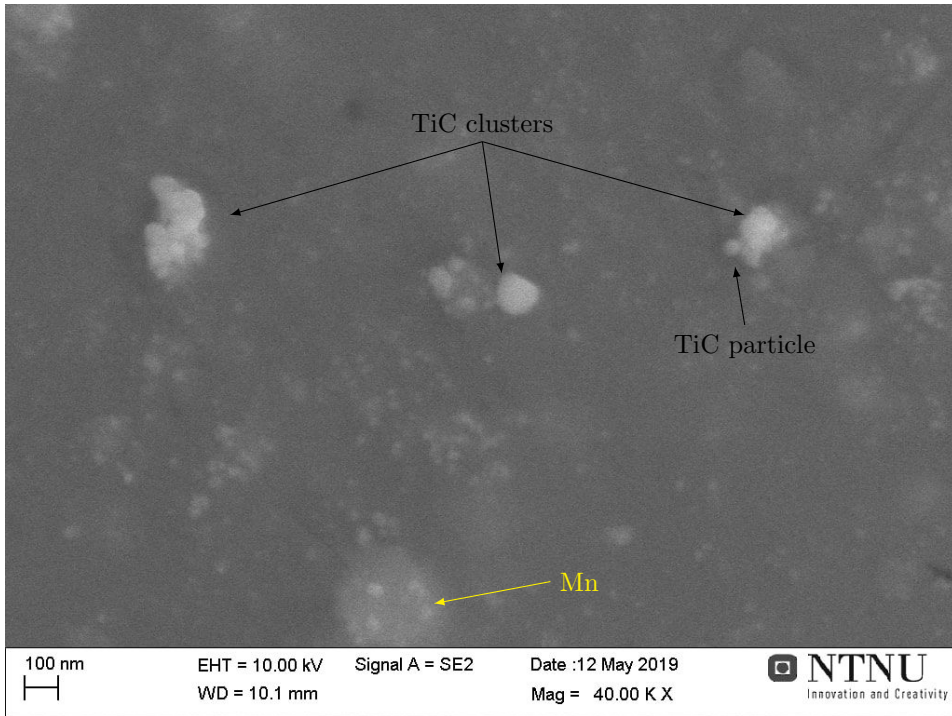
Figure 62: Secondary electron image of the longitudinal cross-section 5183TiC wire sample, showing TiC clusters and particles, and a Mn precipitate. The EDS spectra confirming the identity of each phase may be found in Figure 107 in the appendices.

The EDS spectra confirming the identity of each phase in Figure 62 may be found in Figure 107 in the appendices.

Figure 62 shows that TiC is present both as clusters of nanoparticles and as single nanoparticles. The diameter of the single particle is approximately 50 nm in diameter. The clusters are around 100 nm in diameter, while not completely equiaxed. The clusters in Figure 62 above are on average smaller than the clusters shown in Figure 61. This indicates a variation in the number of TiC nanoparticles in each cluster.

From Figure 60 through Figure 62, it is seen that the TiC particles were uniformly distributed in the composite, mainly present as small clusters ($\approx$ 100 nm to 200 nm in diameter), but in some cases as single nanoparticles. The small diameter of the single particles makes it difficult to observe their distribution in the wire, as they are barely visible even at high magnifications (as in Figure 62).

It may also be observed that the area fraction of TiC particles in the images

is quite low, even when assuming all bright particles in Figure 60 are TiC. The interparticle spacing (i.e. the distance between the TiC-particles and clusters) is observed to be quite high, several micrometers separate some of the TiC clusters in Figure 61.

Several other high magnification SEM images of TiC particles and clusters in the 5183TiC wire, and their EDS spectra, may be found in subsection E.1 in the appendices.

4.5.2   5183TiC-CG wire

The 5183TiC-CG wire sample (extruded with CO_2 cover gas) imaged in this section was also prepared as according to subsubsection 3.2.2, but this sample was not vibration polished in distilled water and rinsed in ethanol. The sample thus contains some SiO_2 residual particles from the vibration polishing in silica suspension. The EDS point analysis confirming the presence of TiC, MgO, Mn and SiO_2 particles in this wire may be found in subsection E.2 in the appendices.

A secondary SEM-image of the matrix in the transversal cross-section of the 5183TiC-CG wire is shown in Figure 63.
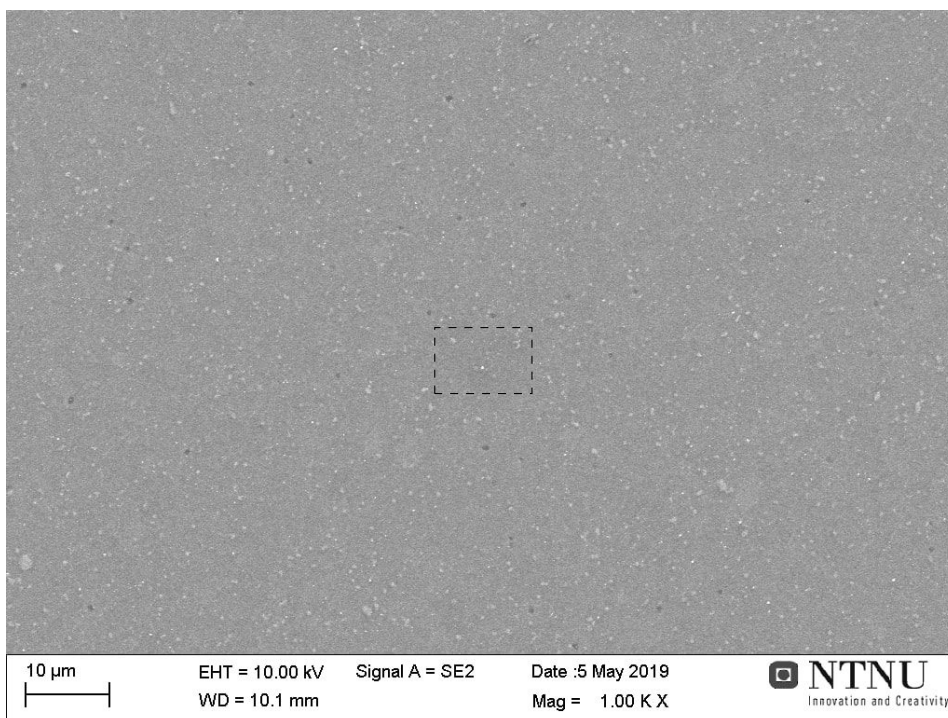
Figure 63: Secondary SEM image of the 5183TiC-CG wire, showing the Al-matrix in the centre of the transversal cross-section wire. The area inside the dashed box is imaged at higher magnification in Figure 64.

78

The light grey phases (some seen in the lower left corner of Figure 63) may be assumed to be Mn precipitates, the dark spots are most likely MgO phases and the bright particles may be assumed to be TiC or SiO_2, given their similar size and morphology.

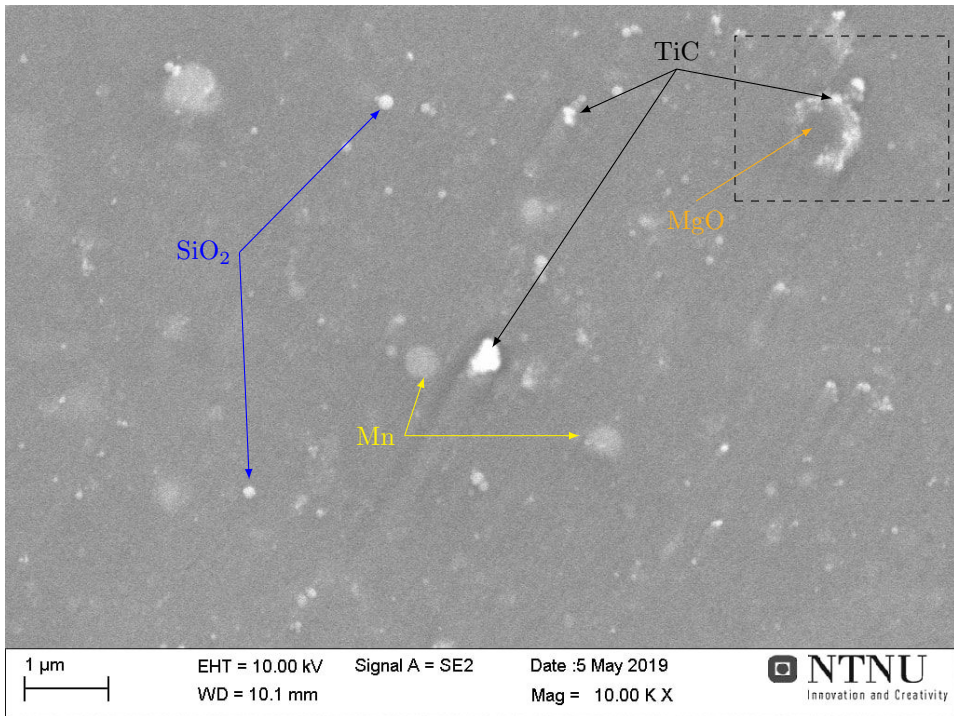The area in the dashed black box in Figure 63, is further imaged at higher magnification in Figure 64.

Figure 64: Secondary SEM image of the central section of the 5183-CG wire, transversal cross-section sample. The arrows indicate phases which were confirmed by EDS analysis (as shown in subsection E.2). The black arrows point to TiC particles, the orange arrow to a (subsurface) MgO particle, the blue arrows to SiO_2 particles (residue from vibration polishing) and the yellow arrows point to Mn precipitates. It may be seen that TiC particles encapsulate the MgO phase in the top, right corner. The area within the dashed box in the upper right corner was examined at higher magnification, shown in Figure 65.

It is observed that the TiC particles are somewhat brighter than the SiO_2 particles. Therefore, it may be assumed that the brighter particles/clusters in Figure 64 are TiC, while the more dim, spherical particles are SiO_2. Particles situated below the sample surface will reflect fewer secondary electrons and thus give a weaker signal, so these may be similar to the SiO_2 particles. For this reason, it may be difficult to distinguish sub-surface TiC from SiO_2, and observing the

relative TiC-amount in the specific area is subsequent to errors. The SiO_2 particles may give an impression that a larger fraction of TiC particles is present in the 5183TiC-CG wire than what is actually the case.

The MgO phase in the top right corner of Figure 64, within the dashed box, is investigated closer in Figure 65. Here, a secondary SEM image is shown in Figure 65a, along with EDS signals (Figure 65b – Figure 65e). It may be seen that the Mg and O signals agglomerate in the dark phase in the centre. Ti signals come from the bright spherical particles surrounding the oxide. It may thus be assumed that the dark particle seen in the centre of Figure 65a is a MgO particle encapsulated by TiC. Due to electron-drift during SEM-imaging, the position of the EDS signals are slightly shifted upwards and to the left, relative to the position of the MgO phase in Figure 65a.
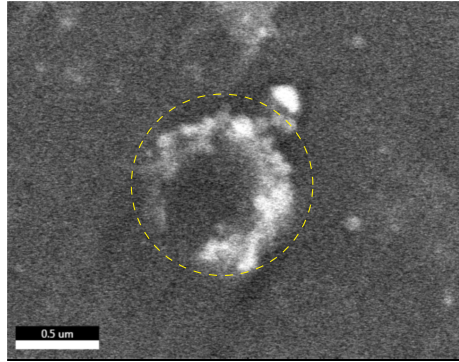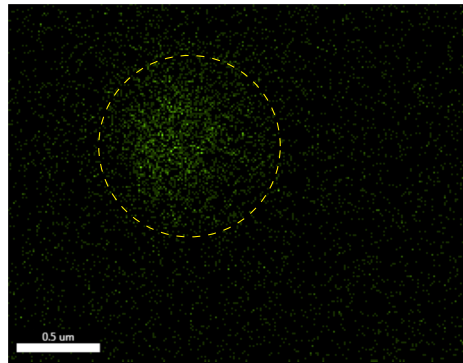
(a) MgO phase.
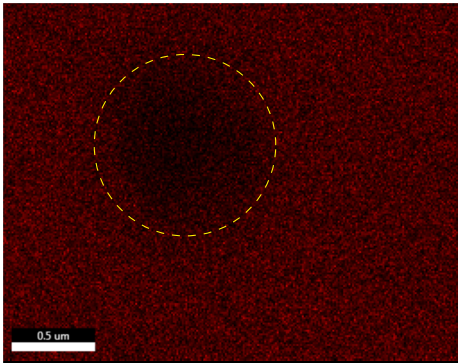
(b) Al EDS signals.
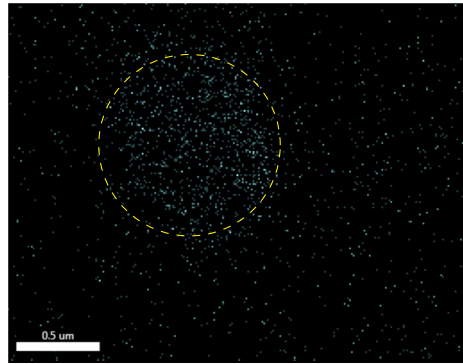
(c) Ti EDS signals.
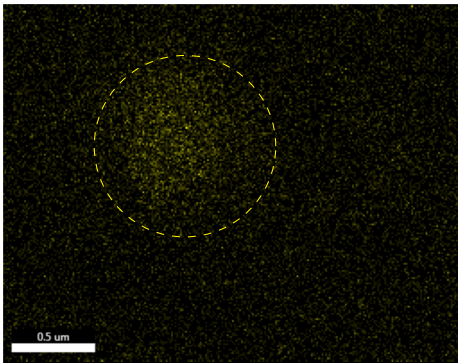
(d) Mg EDS signals.

(e) O EDS signals.

Figure 65: SEM and EDS analysis of MgO phase in the 5183TiC-CG wire. It may be observed that the round MgO phase ($\approx 0.5\,\mu$m in diameter) is encapsulated by bright TiC particles. A yellow, dashed circle has been inserted in the images in order to show the position of the encapsulated oxide.

4.5.3   Comparison of microstructures

For comparison, SEM images of the matrix near the centre in 5183TiC and 5183TiC-CG wires are shown again in Figure 66 and Figure 67.
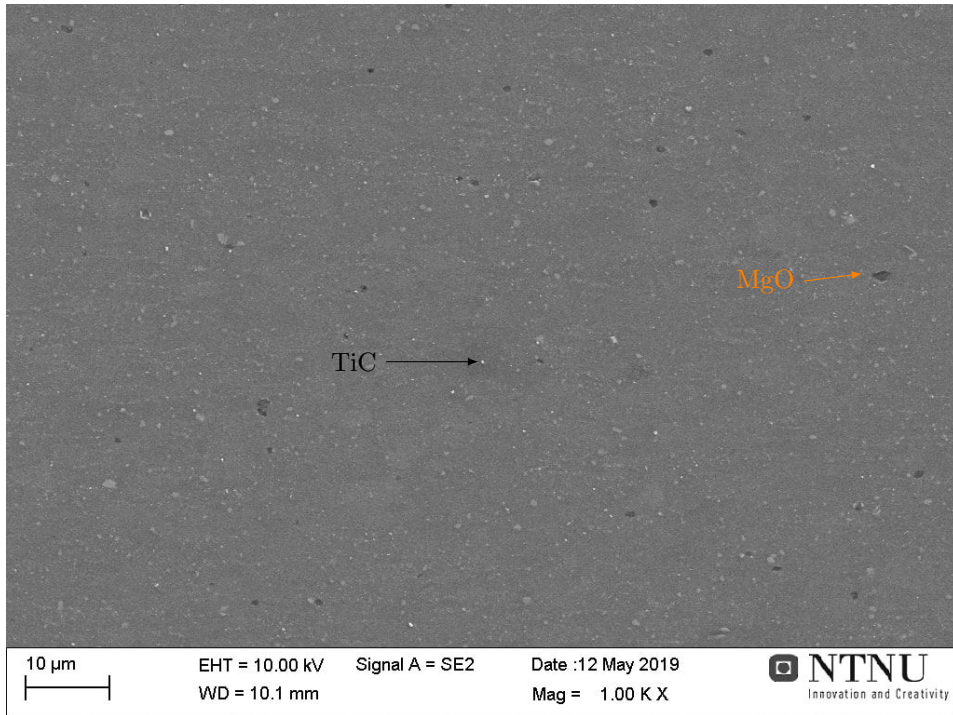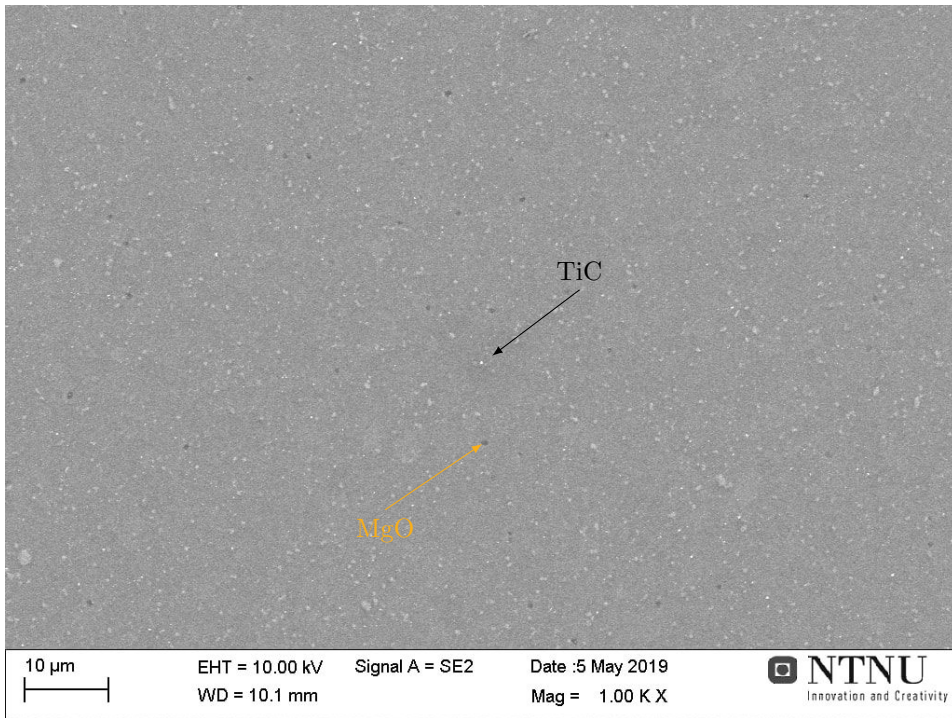

Figure 66: Secondary SEM image of the matrix in the 5183TiC wire. The inserted arrows indicate the phases which were identified using EDS, as seen in subsection E.1 in the appendices. The small, bright particles (bearly visible) are assumed to be TiC nanoparticles. The larger, dark phases are assumed to be Mg-oxides.

Figure 67: Secondary SEM image of the matrix in the 5183TiC-CG wire. The inserted arrows indicate the phases which were identified using EDS, as seen in subsection E.2 in the appendices. Small, bright particles (bearly visible) are assumed to be TiC nanoparticles or SiO_2 particles (residual from vibrational polishing). The dark phases are assumed to be Mg-oxides.

By comparing Figure 66 and Figure 67, it may be seen that the dark Mg-oxide phases in the 5183TiC wire are somewhat larger than the Mg-oxide phases in the 5183TiC-CG wire. To compare the distribution of the TiC nanoparticles in the different composite wires, the central areas in Figure 66 and Figure 67 are shown at higher magnification in Figure 68 and Figure 69, respectively.
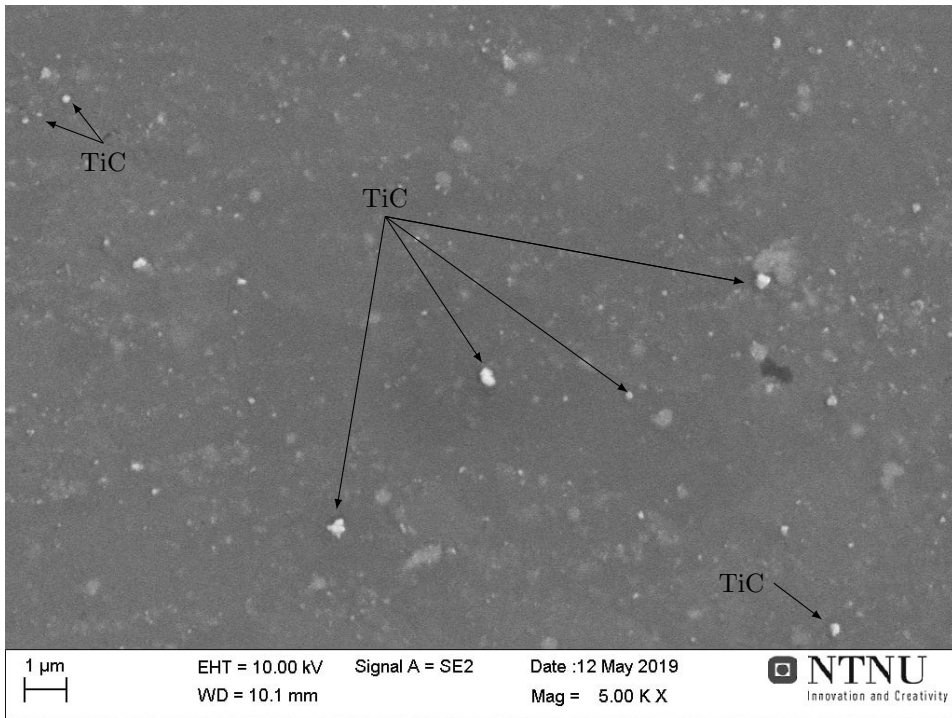
Figure 68: Secondary SEM image of the 5183TiC wire matrix. The black arrows indicate the clusters confirmed to consist of TiC nanoparticles, by using EDS point analysis as shown in subsection E.1 in the appendices. It is observed that the TiC clusters are uniformly distributed in the matrix, though with a rather large interparticle spacing in between. The total amount of TiC particles in the structure is quite low.
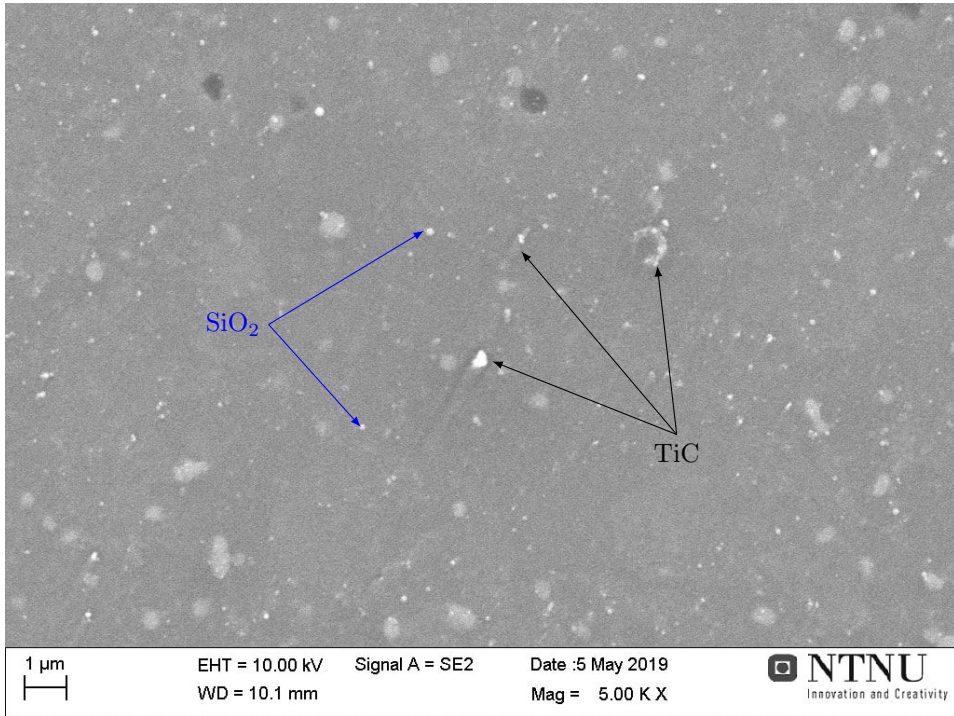
Figure 69: Secondary SEM image of the 5183TiC-CG wire matrix, displaying the same area as in shown Figure 64, but at a lower magnification. The inserted arrows indicate the phases which were identified using EDS, as shown in subsection E.2 in the appendices. Several bright particles, similar to the one in the centre of the image, may be seen throughout the matrix. Thus, it may be concluded that the TiC nanoparticle clusters are uniformly distributed. The interparticle spacing between the TiC clusters is rather large also in this wire. The total amount of TiC particles in the structure is quite low.

From Figure 68 and Figure 69 it may be observed that the TiC nanoparticles mainly appear as small clusters in both wires. These clusters are uniformly distributed throughout the matrix. It may also be noticed that both wires have rather low contents of TiC.

4.6 EBSD analysis

In this section, the results from the EBSD (Electron BackScatter Diffraction) analysis of the 5183-CG and 5183TiC-CG wires are presented. As mentioned in the experimental procedures (see Figure 30), these wires were produced from granules pre-treated without water-rinsing, and with the use of CO_2 acting as a shielding gas during MCSE. The temperature at which the 5183TiC-CG and 5183-CG wire samples were extruded should be similar, as indicated in Figure 51. The only difference between these wires should be the presence of TiC in the 5183TiC-CG wire. Comparing these wires will therefore illustrate the effect of TiC nanoparticles on the grain structure in the extruded wires. The EBSD grain orientation maps (hereon referred to as orientation maps), inverse pole figures (IPFs) and image quality (IQ) maps in this section were all obtained from the centre region of the wires. The orientation maps have dimensions 99.6 X 99.6 µm and indicate the crystallographic orientation and size of the grains in the different wires. Extrusion direction (ED) is from right to left in all orientation maps.

An orientation map of the 5183-CG wire is shown in Figure 70, along with an IPF assigning different colours corresponding to the different crystallographic directions of the grains in the wire, relative to the extrusion direction (ED).
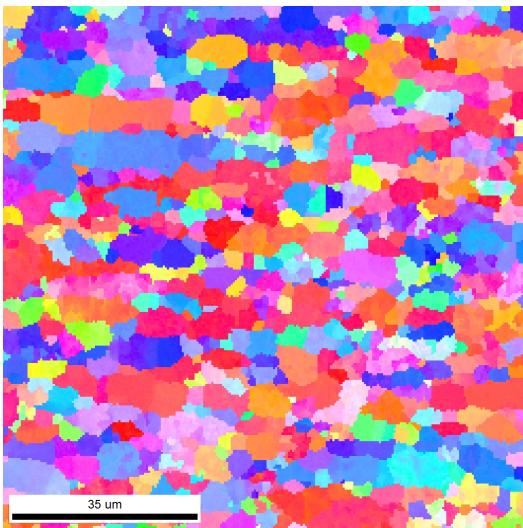
(a) Orientation map.

(b) Inverse pole figure, relative to ED.

Figure 70: Orientation map of the longitudinal cross-section of the 5183-CG wire. The different colours of the grains shows their crystallographic directions, as indicated by the inverse pole figure. The extrusion direction is from right to left in the image. Subgrains, observable as adjacent grains with small colour differences, may be seen in multiple locations in the orientation map. The abbreviations used in the direction designation are: ED=Extrusion Direction and TD=Transversal direction.

An orientation map of a similar area (i.e. of the same size, and also from the centre section of the wire) in the 5183TiC-CG wire is shown in Figure 71.
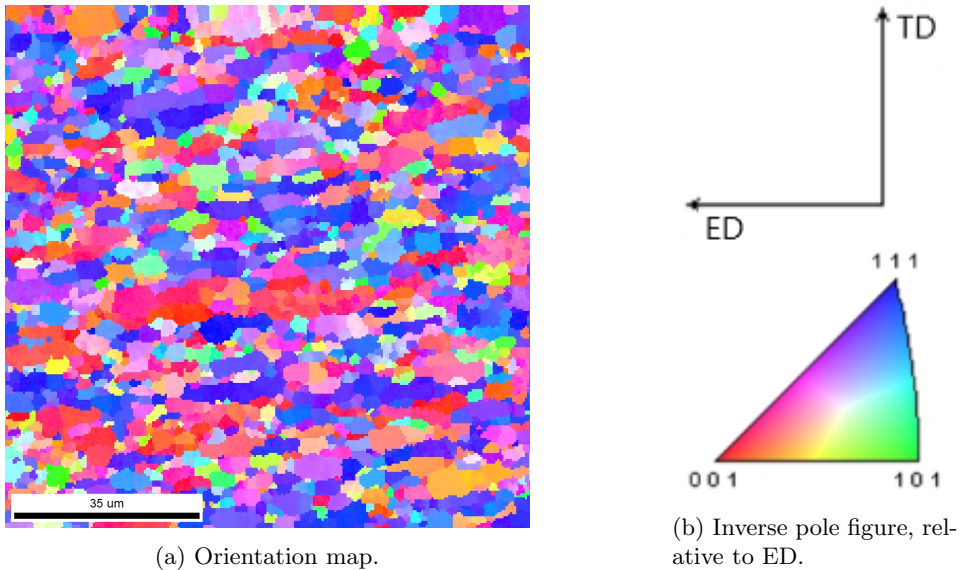

(a) Orientation map.

(b) Inverse pole figure, relative to ED.

Figure 71: Orientation map of the longitudinal cross-section of the 5183TiC-CG wire. The different colours of the grains shows their crystallographic directions, as indicated by the inverse pole figure. Extrusion direction is from right to left in the image. Subgrains, observable as adjacent grains with small colour differences, may be seen in multiple locations in the orientation map. The abbreviations used in the direction designation are: ED=Extrusion Direction and TD=Transversal direction.

Both orientation maps (Figure 70 and Figure 71) indicate elongation of the grains in the extrusion direction (ED), perhaps to a slightly larger degree in the 5183TiC-CG wire. The total number of grains identified in each of the orientation maps above is presented in Table 6. The area of both orientation maps is the same, $99.6\,\mu m$ X $99.6\,\mu m$.

Table 6: Number of identified grains in the inverse pole figures of the 5183-CG and 5183TiC-CG wires, over a $99.6\,\mu m$ X $99.6\,\mu m$ area.

Wire	Number of grains	Grains per micro meter
5183-CG	973	0.098
5183TiC-CG	1499	0.151

From Table 6 it may be observed that a significantly higher number of grains were identified in the investigated area in the 5183TiC-CG wire, compared to the area of the same size in 5183-CG wire.

Pole figures of the 5183-CG and the 5183TiC-CG wires, showcasing the grain texture in the extruded wires, are included in Figure 72 and Figure 73, respectively.
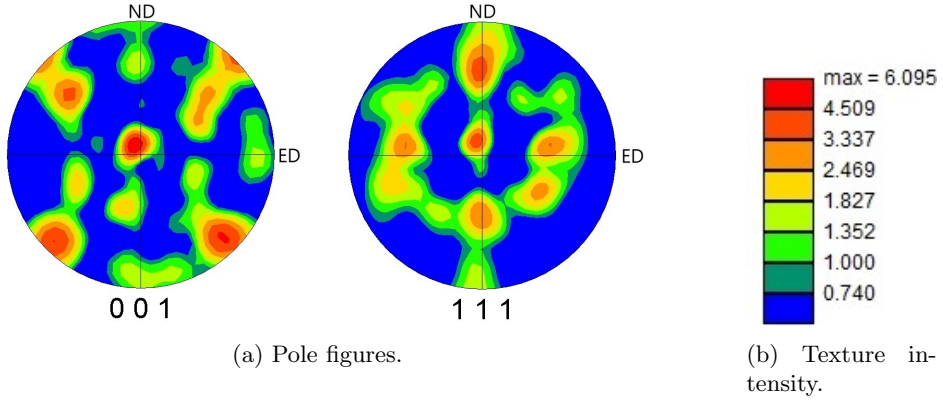

(a) Pole figures.

(b) Texture intensity.

Figure 72: Pole figures of 5183-CG wire in {111} and {001} directions, showing a fiber-like texture in the {111} direction. The texture intensity has the unit "times random".
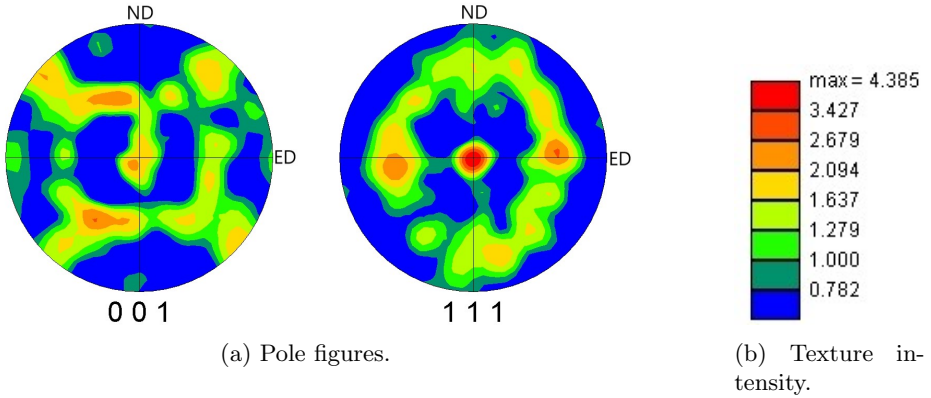

(a) Pole figures.

(b) Texture intensity.

Figure 73: Pole figures of 5183TiC-CG wire in {111} and {001} directions, showing a fiber-like texture in the {111} direction. The texture intensity has the unit "times random".

The {111} pole figures for both wires have weak, fiber-like textures [77]. By comparing the texture intensities, it may be observed that the texture strength in the 5183-CG wire (Figure 72) is only slightly higher than in the 5183-CG wire (Figure 73). The small difference in texture strength is considered to be insignificant for the material properties.

Bar charts showing the grain diameter distribution in the areas examined in Figure 70 and Figure 71 are shown in Figure 74a and Figure 74b, respectively.
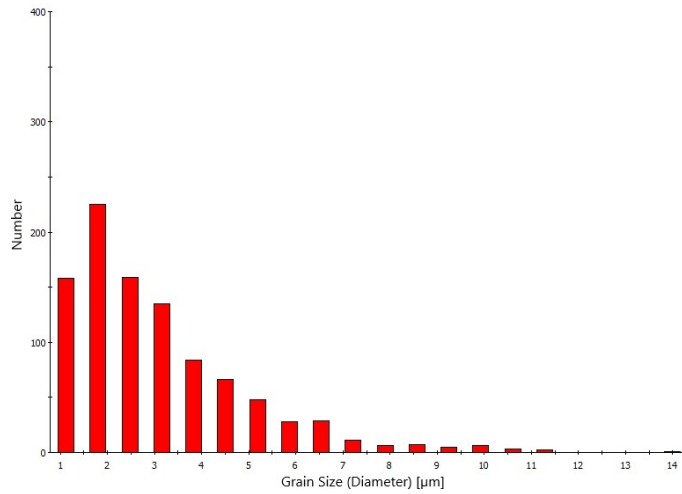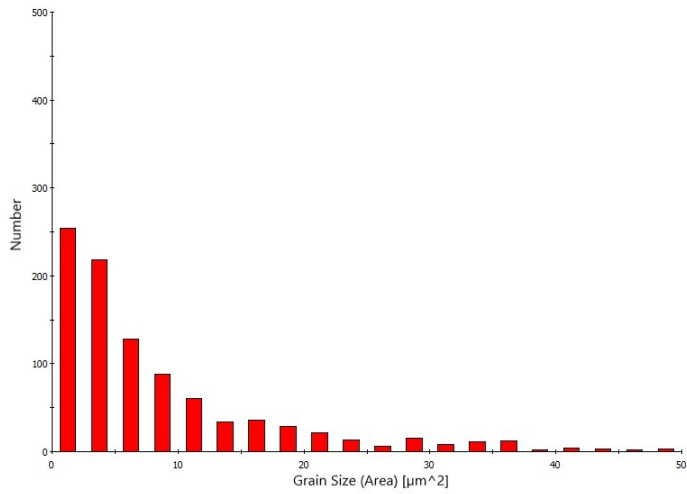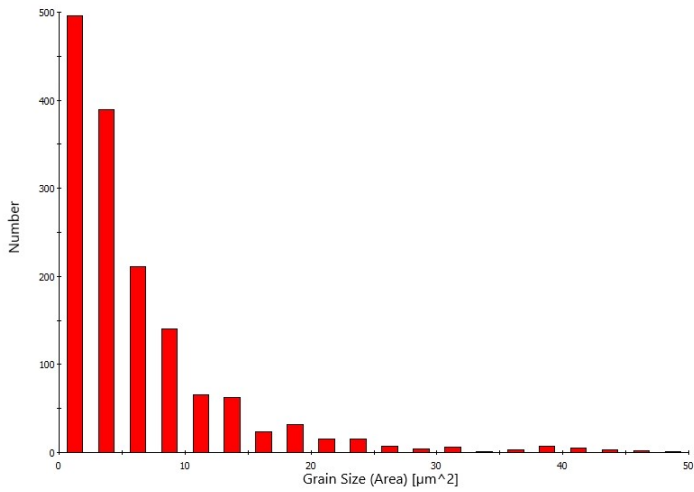
(a) 5183-CG.
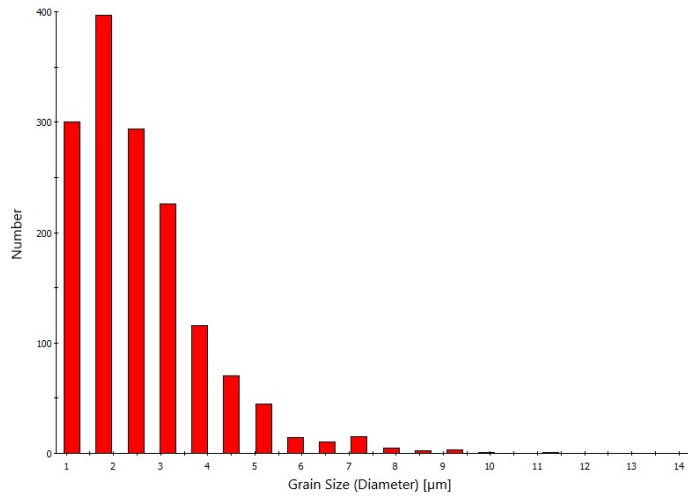
(b) 5183TiC-CG.

Figure 74: Bar charts showing the grain diameter distribution in the wires which were extruded in a CO_2 rich atmosphere. Obtained from EBSD analysis.

From the bar charts in Figure 74, it may be seen that the grain diameter distribution in the 5183TiC-CG wire is more skewed to the left than the distribution for the 5183-CG wire. That is, the grains in the wire containing TiC particles have, on average, a lower diameter than the grains in the monolithic alloys.

As the grains are elongated in the extrusion direction (leftwards in Figure 70 and Figure 71), the grain diameter is for most grains larger in the extrusion direction than in the transversal direction. Thus, the diameter may be a fallacious measure for determining the grain size in the wires. For that purpose, a grain area distribution is more suited. Bar charts showing the grain area distribution for grains with an area less than $50\,\mu m^2$ are included in Figure 75.

(a) 5183-CG.

(b) 5183TiC-CG.

Figure 75: Bar charts showing the grain area distribution in the wires which were extruded in a CO_2 rich atmosphere. Obtained from EBSD analysis.

As seen from the bar charts in Figure 75, the grain area distribution is clearly skewed towards lower areas for the 5183TiC-CG wire, compared with the 5183-CG wire.

The measured average grain diameter and grain area from the EBSD analysis of the areas shown in Figure 70 and Figure 71 are included in Table 7.

Table 7: Average grain size (both in terms of diameter and area) from EBSD analysis of the longitudinal cross section of wires extruded in CO_2 atmosphere.

Wire	Grain diameter [µm]	Grain area [µm^2]
5183-CG	3.07	10.15
5183TiC-CG	2.56	6.59

Table 7 shows that the 5183TiC-CG wire contains the smallest grains, both in terms of grain diameter and grain area.

The misorientation angle between the subgrains seen in the orientation maps (Figure 70a and Figure 71a), was also investigated. A low misorientation angle between the subgrains indicates that recrystallisation has not occured, since the grains are still oriented with their {111} direction along the extrusion direction, and thus have low misorientation angles.

Image quality (IQ) maps, with superimposed colour designations of the misorientation angles between the grains in the monolithic (5183-CG) and composite wires (5183TiC-CG), are included in Figure 76a and Figure 76c, respectively. The IQ maps show same areas as imaged in the orientation maps in Figure 70a and Figure 71a.
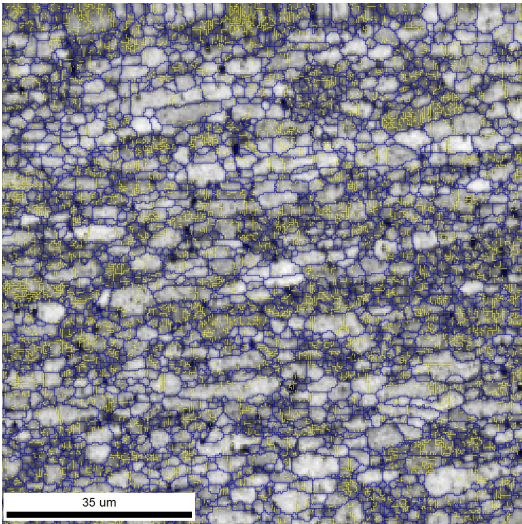
Bar charts showing the distribution of the misorientation angles below 5° in the 5183-CG and 5183TiC-CG wires are shown in Figure 77. It is likely that these low misorientation angles originate from subgrains in the wires, which are indicated by the yellow lines within the grey grains in the IQ maps.
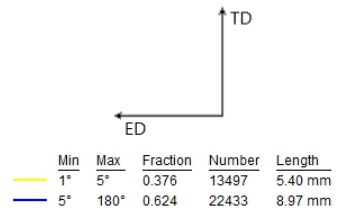
(a) 5183-CG.

	Min	Max	Fraction	Number	Length
	1°	5°	0.483	17227	6.89 mm
	5°	180°	0.517	18440	7.38 mm
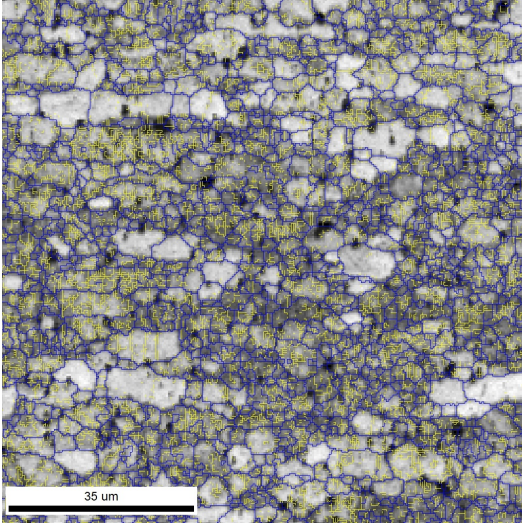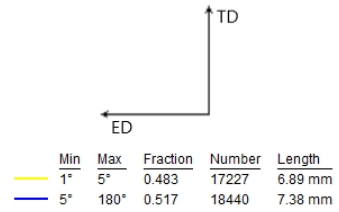
(b) Direction and grain boundary designation, and numerical results.

(c) 5183TiC-CG.

|	Min	Max	Fraction	Number	Length
	1°	5°	0.376	13497	5.40 mm
	5°	180°	0.624	22433	8.97 mm

(d) Direction and grain boundary designation, and numerical results.

Figure 76: IQ maps, with highlighted high and low angle grain boundaries. The yellow lines, accumulated within dark-coloured grains in the IQ maps above, indicate the presence of subgrains with low misorientation angles. (b) and (d) also indicate the total length of grain boundaries and number fractions for low misorientation angles (1–5°) and high misorientation angles (5–180°).
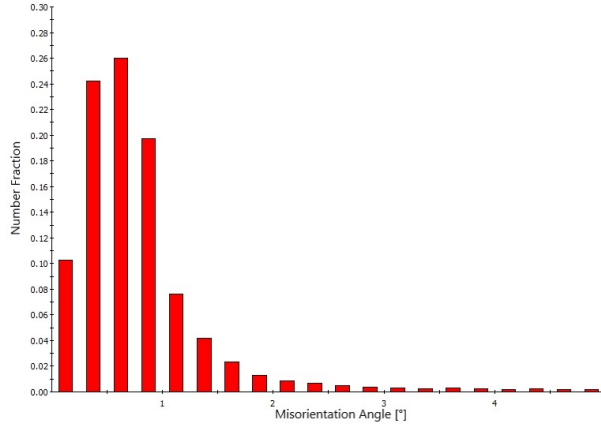
(a) 5183-CG.
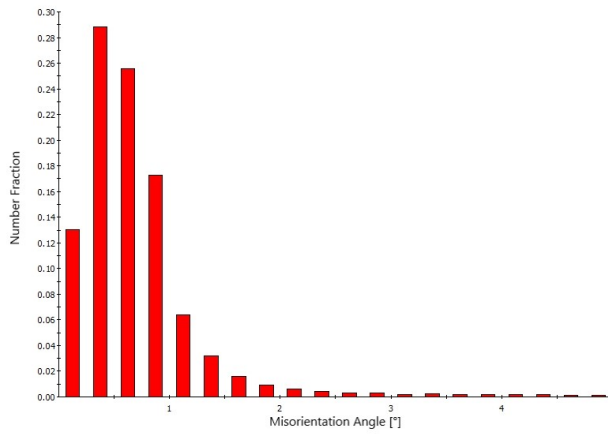
(b) 5183TiC-CG.

Figure 77: Misorientation angle distributions in the wires extruded in CO_2-rich atmosphere. The angles measured are below 5°, and may be assumed to originate from the grain boundaries between subgrains in the structures.

From Figure 77 it may be observed that the misorientation angle distribution is slightly more skewed towards small angles (less than 1°) for the 5183TiC-CG wire. The total number fractions of grain boundaries, having misorientation angles below certain values are presented in Table 8.

Table 8: Total number fractions of grain boundaries below certain misorientation angles in the wires extruded in CO_2 rich atmospheres.

Below:	Number fraction	
	5183-CG	5183TiC-CG
0.125°	0.11	0.13
0.375°	0.34	0.42
0.625°	0.60	0.67
0.875°	0.80	0.85
1.125°	0.88	0.91

Table 8 shows that the 5183TiC-CG wire has larger accumulated number fractions of small angle grain boundaries than the 5183-CG wire. This implies that a larger fraction of the grain boundaries between subgrains in the 5183TiC-CG wire have close to no misorientation between them, which further indicates that recrystallisation in this wire has been hindered to some extent.

4.7 Mechanical properties

In this section, the mechanical properties of the DF (double flight) screw extruded wires are included. The same results for the SF screw extruded wires (4043 and 4043+5183TiC) may be found in section C in the appendices. All the presented strength and elongation measurements are made on wire samples deemed to be representative. Representative samples showed similar mechanical properties as the other samples of the same material, and fractured within the extensiometer gage length. A more scientific determination of the mechanical properties would be achieved if the average values of multiple samples were used. Unfortunately, the strain during tensile testing was measured accurately for only some of the investigated samples, thus calculating average values for the yield strength and elongation was not possible. Therefore, representative values were used in the following analysis.

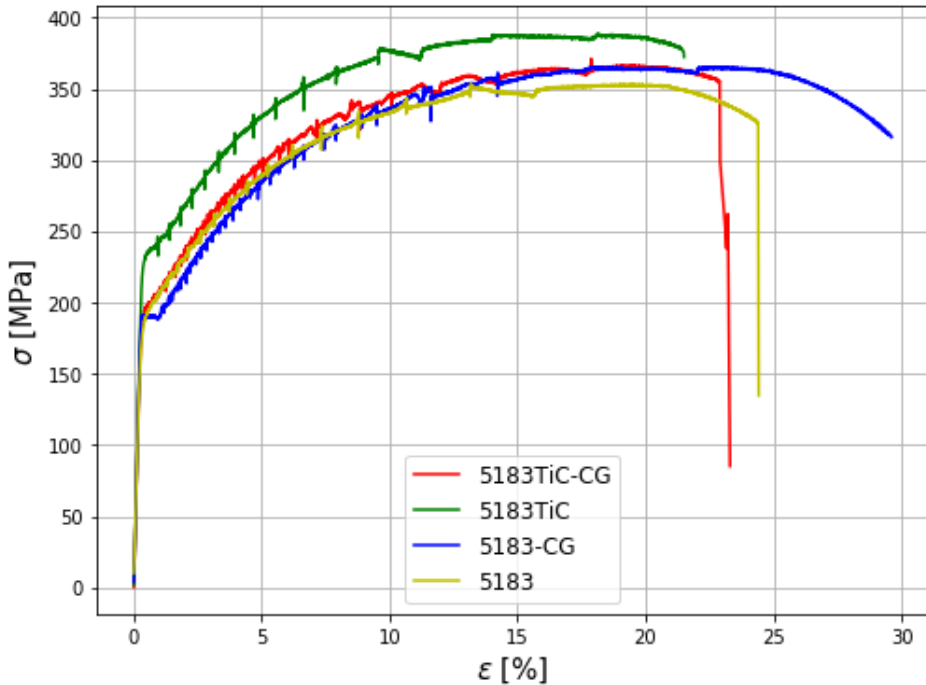Representative stress-strain curves for the four double flight screw extruded 5183 wires are presented in Figure 78.

Figure 78: Engineering stress-strain curves from the tensile test of representative double flight screw extruded wire samples.

The yield strength (σ_Y) was estimated by applying the 0.2 % strain offset method on the tensile curves shown in Figure 78. Ultimate tensile strength (σ_{UTS}) is the maximum engineering stress (σ) value of each curve. EL is the elongation at fracture for each sample. The values for σ_Y, σ_{UTS} and EL for the different wires are presented in Table 9.

Table 9: Yield strength (σ_Y), ultimate tensile strength (σ_{UTS}) and elongation at fracture (EL) for the double screw extruded 5183 wires.

Wire	σ_Y [MPa]	σ_{UTS} [MPa]	EL [%]
5183TiC-CG	198	374	23
5183TiC	233	386	22
5183-CG	190	366	30
5183	191	354	24

From Table 9 and Figure 78 it is clear that the 5183TiC wire exhibits the highest ultimate tensile strength (σ_{UTS}), followed by 5183TiC-CG, 5183-CG and lastly 5183. When it comes to yield strength (σ_Y), the trend is the same, except that the 5183 and 5183-CG wires have almost identical yield strength. From Figure 78 it may also be observed that the 5183-CG and 5183TiC-CG wires, which presumably contain fewer oxides, are more ductile than the wires extruded without the addition of CO_2; 5183 and 5183TiC. These wires are expected to contain more brittle oxides, since no attempts to minimise oxidation was made.

The results of the Vickers microhardness (HV [$HV_{0.1}$]) measurements of the DF extruded wires are presented in Table 10.

Table 10: Microhardness measurements of double flight screw extruded composite and monolithic wires.

Wire	HV $\pm$ Standard devation [$HV_{0.1}$]
5183TiC-CG	94.7 $\pm$ 2.7
5183TiC	103.1 $\pm$ 3.5
5183-CG	86.3 $\pm$ 2.6
5183	87.8 $\pm$ 2.4

The results from microhardness (HV) analysis follows a trend similar to the results from tensile testing; 5183TiC is hardest, followed by 5183TiC-CG. 5183 and 5183-CG exhibit similar microhardness values.

The increase in yield strength, ultimate tensile strength and microhardness due to the addition of TiC nanoparticles to each wire (i.e. calculated by comparing values for 5183-TiC vs. 5183 and 5183TiC-CG vs. 5183-CG), as well as the decrease in ductility, is presented in Table 11.

Table 11: Increase in yield strength, ultimate tensile strength and microhardness, and decrease in ductility attributed to the presence of TiC nanoparticles in the AMC wires.

Wire	$\Delta\sigma_Y$ [MPa]	$\Delta\sigma_{UTS}$ [MPa]	ΔHV $\pm$ STD [HV$_{0.1}$]	ΔEL [%]
5183TiC-CG	8	8	8.4 ± 3.7	-7
5183TiC	42	32	15.3 ± 4.2	-1

It may be observed that the increase in strength (both yield and ultimate tensile strength) due to the addition of TiC is significantly higher in the 5183TiC wire than in the 5183TiC-CG wire.

5 Discussion

5.1 Temperature conditions during MCSE

In this section, the cause and some possible consequences of the temperature evolution during metal continuous screw extrusion (MCSE) of the different wires are discussed. The temperature plots referred to are included in subsection 4.1.

The initial increase in temperature in the plots in Figure 50 and Figure 51 is driven by the external heating from the induction coil. As the induction coil is placed in front of the screw extruder die, T1 will rise at first, since the T1 thermocouple wire is situated in the die and is closest to the induction coil. The heat from the induction coil will over time propagate backwards along the screw and the barrel walls by conduction, so the other thermocouples (T2 – T6) will experience increased temperatures. When granules are added (starting at T1≈ 100°C), the friction and deformation heat arising from the compounding and kneading of the granules by the rotating screw, will also contribute to increase the temperatures in the system.

The rising temperatures lead to a decrease in the viscosity of the screw-plug, i.e. the material situated in front of the screw. When the temperature has reached a sufficient level, the decrease in viscosity allows the continuously fed material to push the plug forward from behind, so that an extruded profile escapes through the die. In all temperature plots it may be observed that extrusion of each wire initiates at T1≈ 450°C, thus this is the required temperature to achieve extrusion.

When T1 reaches 500°C, the extrusion temperatures in the frontal section (T1–T4) are stabilised for all the different wires. Stable temperatures are achieved through balancing the effect of the induction coil with the amount of fed granules (which will reduce temperatures in the system). The alternating spikes in temperatures are attributed to the varying granule feeding rate. Cooling by flushing compressed air through ribs within the screw extruder module also decreased the temperatures.

In Figure 51, it may be seen that applying cooling by compressed air in the extrusion of the ”-CG” wires (indicated by blue, dotted vertical lines in Figure 51) gives an immediate decrease of the temperatures in the system, in particular near the screw stem and the rear of the screw channel, i.e. temperatures T5 and T6. These temperatures should be kept low (under 280°C) to avoid heating the material in the rear of the screw extruder chamber which may ”stick” to the screw. Sticking of the material will impose excessive loads on the electrical engine [6].

When extrusion starts, indicated with red, dashed lines in Figure 50 and Figure 51, the temperatures in the frontal part of the screw chamber (i.e. T1–T4) exceed 240°C. According to the phase diagram for Al-Mg alloys in Figure 2, the system is at this point situated within the one-phase α-Al region. The frontal temperatures remain above 240°C for all the extruded wires. Thus, the wires should be homogenised during screw extrusion, according to the phase diagram in Figure 2.

The phase diagram in Figure 2 is, as all phase diagrams, valid only for a system at thermodynamic equilibrium and at atmospheric pressure. It does not consider the effect of kinetics, but only shows which phases are more thermodynamically

stable. Due to the large plastic deformation and pressures during the screw extrusion, it is likely that the system is not at thermodynamic equilibrium. Additionally, the local temperatures in areas were the material experiences excessive plastic deformation, e.g. near the screw tip or between the screw flights and barrel walls, may exceed the measured temperatures in Figure 50 and Figure 51 [6]. Thus, phase diagrams may only give rough indications on which phases that are stable during screw extrusion.

No β (Al_3Mg_2) phases or remains of corroded β phases were observed along grain boundaries in the OM and SEM analyses, although all extruded wire were slowly cooled in air after screw extrusion. Slow cooling facilitates for the formation of β along the grain boundaries, as this gives the time for the system to reach equilibrium conditions and for β to precipitate. [14]. When the temperature is below $\approx$ 240°C, the precipitation of β should occur in an Al-4.6wt%Mg alloy, according the phase diagram in Figure 2. The absence of observed β phases might indicate that precipitation was avoided, possibly due to the fairly low Mg content in the produced wires. The frontal temperatures stabilise near 450°C, where the solubility of Mg in Al has its maximum at 18.9wt%. Thus, it may be assumed that most of the Mg present in the extruded wires is dissolved in solid solution with the Al-matrix. A large concentration of Mg in solid solution results in increased solid solution and strain hardening strengthening contributions [14] [23].

Some β phase may be initially present in the feedstock-granules before screw extrusion. If this is the case, these will melt according to the Al-Mg phase diagram in Figure 2, when the temperatures are above 450°C in the extruder chamber. This local melting might have resulted in the formation of pores and holes in the extruded wire.

The frontal temperatures T1–T4 in the screw extruder are all kept well above 400°C for extended periods (longer than 20 mins) in all extrusion runs. This facilitates for oxidation of the solid Al-Mg material during screw extrusion, creating MgO and $MgAl_2O_4$ on the granule surfaces exposed to air within the screw extruder chamber, as well as on the wire surface itself after extrusion [32][33]. CO_2 gas was used to inhibit the oxidation of the Al-Mg alloy. It should be noted that the oxidation is not completely avoided by applying CO_2 cover gas, only inhibited. MgO is also expected to be initially present on the feedstock granules, so some MgO will inevitably be found in examined material. When oxidation is inhibited, the content of Mg in solid solution is expected to increase.

As seen from the horizontal time axes in Figure 50 and Figure 51, the duration of each screw extrusion session varied, from approximately 100 min producing the 5183-CG wire to approximately 200 min manufacturing the 5183TiC-CG wire. The duration of a screw extrusion session depends on the amount of extrudate desired, amount of raw material available, temperature conditions, etc. It is believed that when steady-state extrusion is achieved, extrusion may continue for extended time periods. Continuous extrusion requires that cooling is applied to keep the rear temperatures T5 and T6 low, below 280°C, in order to avoid sticking. Stable, continuous extrusion was achieved between 100 min and 200 min during extrusion of the 5183TiC-CG wire, as shown in Figure 51b. The limiting factor for all extrusion

runs in this work was the amount of available feed stock. If more feed stock material was available, it is believed that extrusion may have continued for many more hours.

A sudden temperature peak may be observed at $\approx$ 200 min in Figure 51b. This peak is due to an intentional increase in screw rotation speed, in order to remove as much material as possible from the screw chamber before disassembly was initiated.

5.2 Porosity and cracks in the extruded wires

In this section, the occurrence and possible causes for the observed cracks near the surfaces of the DF screw extruded wires are discussed. First, the optical microscopy images in subsection 4.2 are examined.

As seen in Figure 52, all wires have an irregular, close to elliptical shape in their transversal planes. This abnormal shape is caused by the damages inflicted to the die opening during earlier screw extrusion experiments. The damaged die is imaged in Figure 36. Ideally, the die and the wires should be circular to avoid anisotropic strain conditions during extrusion. The uneven shape of the die also introduces surface defects, such as the "needle" shape seen on the right hand side of the 5183TiC wire in Figure 52b and sharp edges, as seen in the lower left quadrant of all wires.

It is believed that the large, dark crack in the top right quadrant of the 5183-CG wire (indicated with a yellow dashed circle in Figure 54a) is an indication of insufficient compaction of the granules. This assumption is based on its large size and elongated shape along the typical spiralling material flow (as shown in Figure 24). Pores and holes from entrapped gas or corrosion are expected to be significantly smaller than this crack.

From the optical microscopy images in Figure 53, Figure 54 and Figure 55, it is clear that the wires produced with the CO_2 cover gas have fewer and somewhat smaller pores near the surface. It is assumed that the presence of CO_2 gas is the main reason for the reduction in pores, but the use of a pre-treatment procedure without water and/or the temperature of the thermal-rinsing may also have affected the surface appearance.

Though the CO_2 concentrations in the screw extrusion chamber were most likely low for the 5183-CG and 5183TiC-CG wires, due to the somewhat primitive gas-feeding procedure (seen in Figure 39), a significant effect on the porosity was still observed in the optical micrographs in Figure 53 and Figure 55. This supports the conclusions by Smith et. al [37], that even small amounts of CO_2 to air (5%, in terms of partial pressures) have significant inhibiting effects on the oxidation of Mg in the Al-Mg alloy.

The presence of CO_2 gas will only inhibit, and not fully prevent oxidation. Thus, some MgO will inevitably be formed during MCSE of all wires. It is expected that MgO present in the wires may react with water during sample preparation and form magnesium hydroxide ($Mg(OH)_2$) through the following reaction:

$$MgO(s) + H_2O(l) \longrightarrow Mg(OH)_2(s) \tag{19}$$

$Mg(OH)_2$ is water-soluble, though to a small degree (0.0012g/100g water [78]).

This porosity difference between the wires, illustrated in Figure 53, Figure 54 and Figure 55, may be explained by assuming that less MgO is formed during screw extrusion in the presence of a CO_2 cover gas due to the oxidation inhibiting effects of CO_2. Thus, less material will dissolve through Equation 19 in the 5183-CG and 5183TiC-CG wires compared with the 5183 and 5183TiC wires, and fewer pores will be formed. Another plausible cause for the formation of pores is that hard MgO phases may detach during grinding/polishing procedures.

Cracks and pores in the TiC-wires were examined at higher magnifications in the SEM images in subsection 4.3.

Cracks seen in Figure 56 and Figure 57a (found near the surfaces of the wires) are assumed to be formed as a result of insufficient compaction of the granule feedstock during MCSE, based on their large size and depth. It is observed that the cracks in Figure 56 elongate along the extrusion direction, which might indicate that the crack is formed when granules situated parallel to each other during compaction are not fully packed together. Large cracks were not found in the central parts of the wires (shown in Figure 60 and Figure 63), which suggests that the granules near the centre of the wire were more densely packed.

The shallow pore seen in Figure 57b (in the 5183TiC wire) contains significant amounts of TiC particles, as shown by Figure 58c. Some traces of a residual (presumably Mg) oxide phase is seen in its lower left parts. The pore may have formed due to local melting of a large β phase at temperatures above 450°C. The molten β phase may further have absorbed large amounts of TiC nanoparticles during its spiralling flow through the screw extruder. When the wire is cooled after extrusion, the β phase solidifies, shrinks and further detaches from the matrix by brittle fracture. This leaves behind the pore (or fracture surface) seen in Figure 57b, filled with TiC nanoparticles. The detected oxide phase suggest that the β particle has oxidised to form MgO. MgO may further have reacted by Equation 19 to form $Mg(OH)_2$, which dissolves in water.

Another oxide phase was detected near the surface of the 5183TiC-CG wire, as shown in Figure 59. Comparing the EDS maps, it may be seen that this phase is likely MgO as no characteristic Al signals are emitted from the oxide. Figure 59c shows that TiC particles have also agglomerated around this phase. It is believed that this oxide phase has formed as a consequence of the TiC coating process. It is assumed that Mg-oxides are initially present on the 5183 welding wire used to produce the granule feedstock, as it is likely that this wire has experienced elevated temperatures (i.e. above 300°C) during manufacturing. Literature supporting this assumption is reviewed in subsection 2.3. Thus, when granules are coated with TiC nanoparticles, some of the reactive nanoparticles attach to the Mg-oxide particles already present on the surface.

The intended final use for the extruded wire is as a welding wire in a WAAM (Wire Arc Additive Manufacturing) procedure. To ensure that the wire surface is smooth enough for the welding applications, an additional rolling and drawing procedure is needed. Welding wires are typically 1.2 mm in diameter or thinner [79]. Therefore, a drawing procedure is also necessary to make the extruded approximately 9.8 mm diameter wires suitable for welding. Another requirement is

that the amount of pores, oxides and hydroxides in the wire should be kept to a minimum. Thus, the best candidate material for welding is the 5183TiC-CG wire, since this has fewer pores (than the 5183TiC wire, as seen by comparing Figure 53 with Figure 54) presumably contains less Mg-oxides, and was not rinsed in water (see Figure 30 in section 3). The absence of water in the cleaning procedure of the feedstock granules is expected to minimise the amount of hydroxides in the extruded wire, though this was not verified in this work.

5.3 Distribution of TiC Nanoparticles

In this section, SEM images in subsection 4.5 are discussed.

All SEM images of the matrix in the composite wires (shown in Figure 60 through Figure 69) indicate that a uniform distribution of the reinforcing TiC nanoparticles was achieved through MCSE. The distribution is easiest to observe in the 5183TiC wire, shown in Figure 60 and Figure 61, as this was free of SiO_2 particles. It is reasonable to believe that all visible bright particles in these images are TiC, and that no degrading reactions (e.g. Equation 15 in subsection 2.9) have occurred since no traces of Al_4C_3 or $TiAl_3$ were observed in their vicinity. This is further supported by the extended EDS analysis shown in subsection E.1 in the appendix. Thus, it may be assumed that the temperatures during MCSE were low enough (i.e. below 600°C [5]) to avoid forming these unwanted reaction products.

Some SiO_2 residual particles are seen in the SEM images of the 5183TiC-CG wire in Figure 63 and Figure 64. These particles may be difficult to distinguish from TiC particles, but some difference in their brightness may be seen in Figure 64. Assuming that all the brighter particles are TiC nanoparticles, it is seen that they are uniformly distributed also in this wire.

A uniform distribution is crucial as it gives structural integrity and isotropic mechanical properties in the produced composite, as well as a fine grain structure when the wire is melted in the future WAAM-welding procedure, as the TiC nanoparticles will likely act as inoculants for heterogenous nucleation when the weld is cooled [42][43][44][55]. Unfortunately, a large interparticle spacing was observed, on the order of several micrometers, as seen for both TiC-wires in Figure 68 and Figure 69. A large interparticle spacing will lead to increased grain sizes after welding, since the grains will start to grow farther apart [44]. This will in turn will result in a smaller Hall-Petch strengthening contribution in the solidified weld, as according to the Equation 2.

Large interparticle spacing between the TiC nanoparticles will also lead to decreased contribution from Orowan strengthening [53]. The strengthening contribution from Orowan strengthening is inversely proportional with the interparticle spacing, as seen in Equation 8. Instead of producing many, closely spaced dislocation loops which act as barriers towards the propagation of other dislocations, and thus increases strength, the TiC nanoparticles will form dislocation loops spread far apart, which will not effectively hinder the movement of dislocations.

From Figure 61, the clustering behaviour of the TiC-nanoparticles may be observed. The TiC nanoparticle manufacturer (**US Research Nanomaterials Inc.**) reported an initial diameter of around 50 nm for the single particles, which was con-

firmed in section B in the appendix. The SEM image of a TiC-coated feedstock granule surface in Figure 79 shows that the TiC particles are somewhat clustered before they are screw extruded.
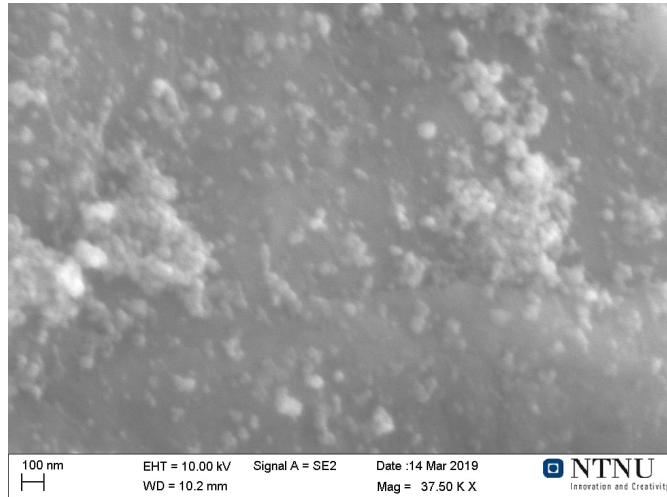

Figure 79: SEM image of the surface of a TiC coated 5183 granule, used as feedstock for the MCSE manufacturing of AMC-wires. Bright TiC clusters may be seen. The diameter of a single nanoparticles is around 50 nm. The EDS spectra confirming that the bright particles are TiC nanoparticles and diameter measurements may be found in section B in the appendix.

It is believed that these particles may remain clustered throughout the screw extrusion, resulting in the small, irregular shapes seen in Figure 61 and Figure 62. It is assumed that the particles remain clustered due to their high surface/volume ratio, which results in increased reactivity. Clustering is likely to reduce the achieved strength in the TiC-reinforced wires [57]. Agglomeration of the TiC-nanoparticles results in a larger effective reinforcement particle size. This decreases the effect of the different strengthening contributions, as illustrated in Figure 12. Small scale clustering of the TiC nanoparticles will also likely decrease their grain refining effect during solidification through heterogeneous nucleation [44].

From the SEM images in subsubsection 4.5.1 and subsubsection 4.5.2 it is also observed that the area fraction of TiC particles present in the structure is quite low, most likely well below 3wt% which was the initial weight fraction during the coating of the 5183-granules. This indicates a significant loss of TiC particles during coating, storing and screw extrusion. An exact estimate on the weight or volume fraction TiC achieved in the composite wires is difficult to obtain. A possible method is to measure the area fraction covered by TiC in the SEM images, but this would be time-consuming and prone to significant error sources.

It is believed that the MgO particle shown in Figure 65 originates from the surfaces of the 5183-granules used to produce the wire. The TiC nanoparticles

may have attached to the MgO particle on the granule surface during coating, encapsulating it. As apparent from Figure 65, this TiC-encapsulated MgO particle is not affected by the screw extrusion, the TiC particles are not broken off, resulting in a agglomeration of TiC particles. Ideally, this cluster of TiC should be broken up, so that the nanoparticles are distributed in the martix.

In summary, a uniform distribution was obtained, which is promising for the further use of MCSE for the production of AMC. But large interparticle spacing and a low fraction of TiC was observed, which will decrease their strengthening effects. Therefore, a new TiC-feeding procedure should be implemented, in order to decrease particle spacing and avoid attachment of TiC to the Mg-oxides initially present on the Al-Mg granules.

5.4   Oxidation inhibition

For simplicity reasons, the products from the oxidation of Mg in the Al-Mg alloys are in this section referred to as only MgO, although $MgAl_2O_4$ might have also been formed. The focus in this discussion is on whether or not oxidation has occurred during screw extrusion, and to which extent. The exact stoichoimetry of the oxidation product is thus in this case of secondary importance.

By considering the difference in the appearance of the dark MgO phases found in the matrix of the 5183TiC and 5183TiC-CG wires (shown in Figure 66 and Figure 67, respectively), it is apparent that the dark MgO phases are on average larger in the 5183TiC wire than in the 5183TiC-CG wire. However, the number of MgO phases is roughly equal in both wires. It is assumed that the size difference between the MgO phases is a consequence of the oxidation inhibiting properties of CO_2.

A mechanism for the oxidation inhibition achieved when using CO_2 cover gas during screw extrusion is proposed below, building on the findings of Wefers [32] and the suggested mechanism by Smith et al. [37]:

1. When CO_2 gas is flushed into the screw extruded chamber through the feeding hole, CO_2 molecules are rapidly absorbed onto the MgO surface layer on the TiC-coated 5183 granules. As seen in Figure 79, the TiC nanoparticles do not cover the entire granule surface, exposing plenty of MgO surface which will interact with CO_2 from the atmosphere.

2. The oxide layer grows around the absorbed CO_2 as the temperatures in the screw extruder rise. An Mg-C-O phase is formed on the granule surface, from a reaction between absorbed CO_2 and the MgO layer, due to a decreased oxygen partial pressure.

3. The Mg-C-O phase acts as a protective cap, hindering further out-diffusion and oxidation of Mg in each granule. This will increase the fraction of Mg present in solid solution in the 5183-CG and 5183TiC-CG wires, compared with 5183 and 5183TiC, and decrease the amount of MgO phases present.

Each feedstock granule is assumed to initially have an MgO layer on its surface, formed during production of the delivered 5183 welding wires, which has likely included elevated temperatures. This facilitates for the oxidation of the solid Al-Mg wire [33]. During thermal rinsing at 350°C (of the 5183 and 5183TiC wire granules), the oxide layer has most likely grown further, depleting more Mg from the bulk material in the granules. According to the literature (reviewed in subsection 2.3), the thermal rinsing at 130°C does not involve temperatures high enough for oxidation.

During screw extrusion, the temperatures exceed 300°C (as seen in Figure 50 and Figure 51), facilitating for another instance of oxidation. When CO_2 gas is flushed to the screw extruder chamber (in the rear, see Figure 39), the atmosphere surrounding each granule becomes CO_2 enriched. The CO_2 gas will inhibit oxidation by the above mentioned mechanism, reducing the amount of MgO formed on the granule surfaces significantly.

When the granules are compacted and the wire is screw extruded, the MgO phases are further distributed in the wire. The MgO phases present on the granule surfaces are assumed to merge together under the severe deformation forces during screw extrusion, producing larger MgO phases. Since the number of MgO particles on the 5183TiC granules is larger than on the 5183TiC-CG granules, the MgO phases in the 5183TiC wire will be larger than in the 5183TiC-CG after the deformation during screw extrusion (as seen in Figure 66 and Figure 67). A sketch illustrating the suggested mechanism for the difference in MgO-size is included in Figure 80.

Ambient atmosphere CO_2-rich atmosphere

$\bullet$ = CO_2
$\bullet$ = MgO

Granule surface
$\blacksquare$ = Al-Mg

Mg   Mg

Screw | extrusion

Wire

$c_{Mg,Air}$ c_{Mg,CO_2}

$$c_{Mg,Air} < c_{Mg,CO_2}$$
$$c_{MgO,Air} > c_{MgO,CO_2}$$
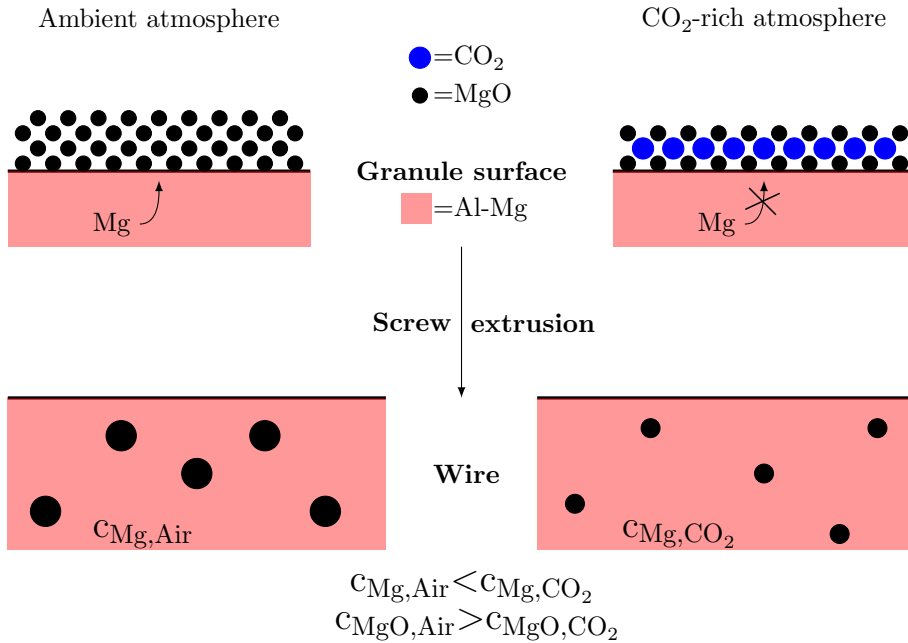
Figure 80: Sketch illustrating the suggested mechanism for oxidation inhibition during screw extrusion, and the compaction and distribution of MgO particles. It is assumed that the small MgO particles on the granule surfaces are merged together due to the large deformation forces during screw extrusion to form the larger MgO phases seen in the SEM images. The resulting concentration of Mg in solid solution in the wire which is screw extruded in CO_2-rich atmosphere (c_{Mg,CO_2}) will be larger than the Mg concentration in the wire which is screw extruded in air ($c_{Mg,Air}$), and vice versa for the concentration of MgO in the different wires. The dimensions in this sketch are not to scale.

As shown in Figure 80, it is expected that the amount of Mg in solid solution in the extruded wires (c_{Mg}) is increased when using CO_2 cover gas during extrusion, as less MgO is produced.

Drawing a certain conclusion on the mechanism for the formation and distribution of the Mg-oxides, illustrated in Figure 80, from just the two images in Figure 66 and Figure 67 is dubious. It might also be that the reason for the larger MgO phases is the difference in thermal pre-treatment of the granules (seen in Figure 30). To further test the suggested mechanism, more research is needed. Another possible reason for the comparably larger MgO phases in Figure 60 is that this wire was vibrational polished in destilled water for 1 hour and rinsed in ethanol for 30 min in an effort to remove residual SiO_2 particles from the surface. During this exposure to water, further the MgO phases may have reacted with water through Equation 19 and dissolved, making the MgO phases appear larger. The additional SiO_2-removal procedure was not done for the 5183TiC-CG wire sample shown in

Figure 63, thus this sample was not exposed to water for prolonged periods.

5.5 Grain structure investigation - EBSD

When comparing the orientation maps in Figure 70 and Figure 71, it may be seen that the both wires show a deformed grain structure. The 5183TiC-CG grains are slightly more elongated in the extrusion direction compared to the 5183-CG grains. This might indicate that TiC has hindered recrystallisation to a small degree, keeping the deformed grains in the TiC-reinforced wire from re-orienting and growing into more equiaxed grains, as are seen in the 5183-CG wire.

Table 7 shows that the number of identified grains in the 5183TiC-CG wire is significantly larger than in the 5183-CG wire. For the same areas of 99.6 X 99.6 µm^2, 526 more grains were observed in the 5183TiC-CG wire than in the 5183-CG wire. This indicates that the grain size is reduced in the TiC containing wire, which is further supported by comparing the grain diameter distributions for the 5183-CG and 5183TiC-CG wire in Figure 74a and Figure 74b, and the grain area distributions in Figure 75a and Figure 75b. The grain size difference may be explained by assuming that the TiC nanoparticles has pinned the grain boundaries through *Zener Pinning*, hindering grain growth at elevated temperatures [54].

Repeated instances of deformation and recrystallisation occur throughout the screw extrusion. When the wire is extruded through the die opening, the material recrystallises for the last time, before cooling in ambient air atmosphere [80]. It is believed that this final recrystallisation step during extrusion is inhibited to a larger extent in the TiC-reinforced wire, due to Zener pinning.

The PFs (pole figures) in Figure 72 and Figure 73 indicate a weak {111} fiber texture in both wires [77]. The texture orientation direction is coinciding with the {111} slip plane in the fcc crystal structure of Al [11]. Both wires showed fairly low texture intensities, with maximum at 6.095 times random for the 5183-CG wire, and at 4.385 times random for the 5183TiC-CG wire. The difference in texture intensities/strength was assumed to be insignificant.

From the bar charts in Figure 77 and Table 8 it is apparent that the introduction of TiC to the 5183 alloy increases the fraction of grains with misorientation angle below 1°.

Figure 77a shows that a significant higher fraction of the grains in the 5183-CG wire have recrystallised to achieve a low misorientation angle, compared with the 5183TiC-CG wire, which has a more deformed structure. This might also indicate that TiC hinders the recrystallisation of the deformed grains in the 5183TIC-CG wire at the elevated temperatures experienced during MCSE, through Zener pinning.

In summary, the EBSD analysis indicated that the structure in the extruded
"-CG" wires was highly deformed, with smaller grain sizes in the 5183TiC-CG wire
due to *Zener pinning*, exerted by the TiC nanoparticles on the grain boundaries.
A weak {111} fiber texture was observed, with no significant difference in texture
strength between the wires.

5.6   Mechanical properties

In this section, the mechanical properties of the 5183, 5183-CG, 5183TiC-CG and
5183TiC wires are evaluated and discussed. It is assumed that the determining
factor for the mechanical properties of these wire is the presence of TiC and/or
Mg-oxides, since all other parameters should be constant. The stress-strain curves
in Figure 78 all show clear serrations, indicating PLC (Portevin-Le Châtelier) be-
haviour for all tested wires. Thus, it may be assumed that the addition of TiC
nanoparticles had no significant effect on the dynamic strain ageing responsible for
the serrated stress-strain behaviour.

From the stress strain curve in Figure 78 and the numerical results in Table 9,
it may be seen that the 5183TiC wire (extruded without CO_2 cover gas shielding)
exhibits the highest strength, both in terms of yield strength and ultimate tensile
strength. Compared with the monolithic 5183 wire, it is clear from Figure 78 and
Table 11 that the presence of TiC increases both yield strength and ultimate tensile
strength significantly. It is believed that the increase in strength is mainly due to
the EM (elastic modulus) mismatch between the stiff TiC nanoparticles and the
soft Al matrix.

The effect from Hall-Petch strengthening is likely to be small, as the difference in
grain diameter is in the order of 0.1 µm (see Table 7) and the Hall-Petch coefficient
for Al is low (=0.04 MPa$\sqrt{m}$) [47].

The SEM images in subsection 4.5 revealed that the distance between TiC
clusters/particles in the 5183TiC and 5183TiC-CG wires is fairly large (order of
micrometers). Therefore, it is assumed that strengthening contribution from the
Orowan mechanism is insignificant, as indicated by Equation 8 [51].

Since the wire was left to slowly cool at ambient temperatures after extrusion,
it is believed that the dislocation density in the vicinity of the TiC particles will be
annihilated. Thus, no strengthening through CTE (Coefficient of Thermal Expan-
sion) mismatch will take place. CTE mismatch strengthening is more apparent in
composites manufactured through a liquid state processing route (MCSE is a fully
solid state manufacturing process). However, if the TiC-wires are used as weld
filler wires, CTE is expected to give a large strengthening effect, as reported by
Fattahi et al. [55].

A similar increase in yield and tensile strength as seen for the 5183TiC wire
was not observed for the 5183TiC-CG wire, as revealed by the numerical results
in Table 11. The increase in yield strength in the 5183TiC-CG wire is less than
20% of the increase for the 5183TiC wire, while the increase in tensile strength
is 25% of that in the 5183TiC wire. From the tensile curve in Figure 78 and
the numerical results in Table 9 and Table 10, it is seen that the 5183 and the
5183-CG wires exhibit similar mechanical properties. It is therefore expected that

the mechanical properties should improve equally in both the 5183TiC and the 5183TiC-CG wires, with the addition of TiC. Since this is not the case, it is assumed that a lower fraction of TiC reinforcement particles were added to the 5183TiC-CG wire than the 5183TiC wire. This might be explained by looking at the presumably only differing factor between the two wires, namely the supplying of CO_2 gas to avoid oxidation. As the CO_2 was flushed to the screw chamber through a tube connected to the granule funnel (see Figure 39), it might have blown some of the TiC nanoparticles off the granules and out of the chamber. This will result in a lower fraction of TiC nanoparticles in the 5183TiC-CG wire compared to the 5183TiC wire.

When comparing the ductility of the 5183 and 5183-CG wires, the effect of the CO_2 gas is apparent as the elongation increases when the formation of Mg-oxides is reduced by CO_2 gas shielding. From Table 9 it may be seen that the ductility increases with 6 percentage points when MgO is "removed" from the 5183 wire. It is likely that presence of larger, brittle Mg-oxides in the matrix of the 5183 and 5183TiC wires decreases ductility. The ductility of the 5183TiC-CG wire is slightly (1 percentage point) larger than for the 5183TiC, supporting this assumption. The smaller increase of the ductility in the TiC-reinforced wires may be attributed to the fact that the TiC particles themselves will decrease the ductility of the material, by acting as local stress raisers.

For its intended purpose as a welding wire in a WAAM procedure, the mechanical properties are not the most crucial (no special requirements for strength etc.). The main requirement is an uniform distribution of reinforcement particles, which was achieved. But for the necessary drawing procedure it is an advantage if the wire is ductile, therefore the 5183TiC-CG wire is the most promising candidate for further processing. In addition, a strong strain hardening behaviour is desired, as this will also facilitate for easier drawing since the risk of premature fracture is reduced. The strain hardening behaviour of the different wires is investigated in the following subsection.

5.6.1 Strain hardening investigations

The strain hardening properties of the double flight (DF) screw extruded wires are investigated in this section, based on the data obtained in the tensile testing.

By assuming that no volume change occurs during deformation, true stress and true strain during the tensile testing may be estimated by the following relations [11]:

$$\sigma_T = \sigma(1 + \epsilon) \tag{20}$$

$$\epsilon_T = \log(1 + \epsilon) \tag{21}$$

Where log is the natural logarithm, σ_T is true stress, σ is engineering stress, ϵ is the engineering strain and ϵ_T is the true strain. The relationship between true stress and true strain may be approximated by Hollomon's equation [11]:

$$\sigma_T = K\epsilon_T^n \tag{22}$$

where K and n are material and condition dependent constants. K is known as the *strength coefficient* and n as the *strain-hardening exponent* [11]. Hollomon's equation is only valid for the true stress-strain relationship after the onset of plastic deformation, and before necking occurs. Therefore, an evaluation interval from $\epsilon = 1\%$ to $\epsilon = 10\%$ in the tensile curve in Figure 78 was chosen for the strain hardening investigation. The engineering stress-strain curve for this interval is shown in Figure 81a. The corresponding true stress-strain curve, calculated using Equation 20 and Equation 21, is shown in Figure 81b.
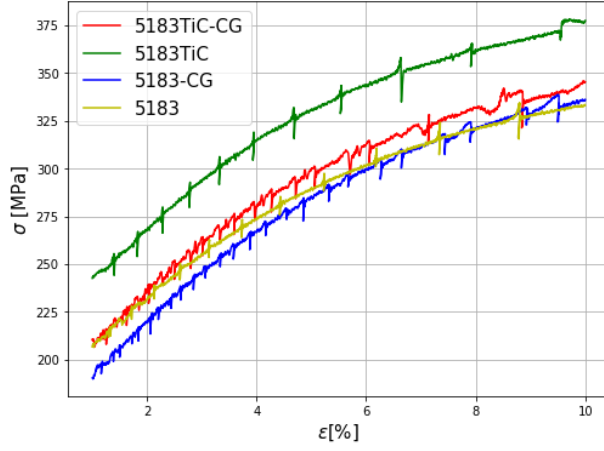
(a) Engineering stress-strain curve.
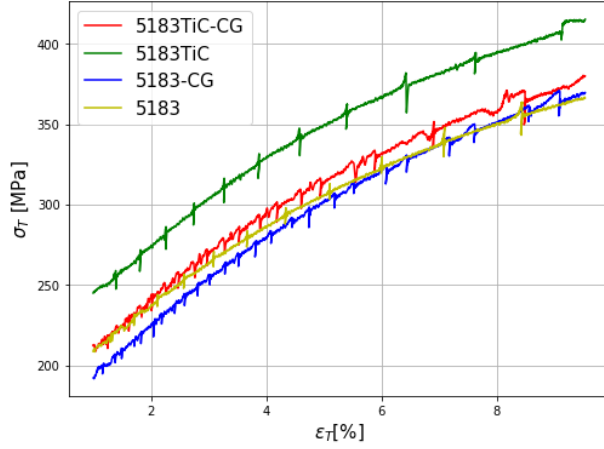
(b) True stress-strain curve.

Figure 81: Stress strain curves under uniform plastic deformation during tensile testing of the representative DF screw extruded wire samples.

By rearranging Equation 22, a linear expression for true stress versus true strain is obtained:

$$\ln(\sigma_T) = n\ln(\epsilon_T) + \ln(K) \tag{23}$$

A plot of $\ln(\sigma_T)$ versus $\ln(\epsilon_T)$, with inserted linear regression lines, is shown in Figure 82. The linear regression lines were estimated using values for within the chosen strain interval for the representative DF wire samples.
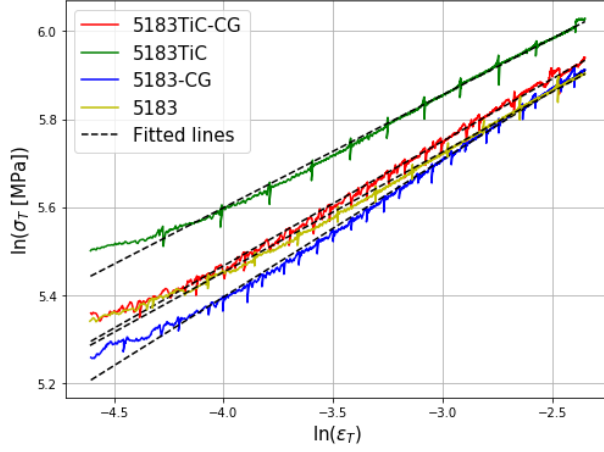
Figure 82: Plot of logarithmic true stress versus logarithmic true strain, used to obtain the strength coefficient K and the strain hardening coefficient n for each sample. The fitted linear regression lines are inserted as dashed, black lines.

The values for the strain hardening coefficient n and strength coefficient (K) of each DF screw extruded wire were obtained from the linear regression approximation lines in Figure 82. The estimated strain hardening n and strength coefficients K are included in Table 12, along with the standard error for the approximation of n (SE_n).

Table 12: Estimated strain hardening exponents (n) and strength coefficients (K) for the DF wires, from a strain interval of $\epsilon = 1\%$ to 10%.

Wire	n	K [MPa]	SE_n
5183TiC-CG	0.283	740	$4.2 \cdot 10^{-4}$
5183TiC	0.256	748	$4.0 \cdot 10^{-4}$
5183-CG	0.312	768	$4.4 \cdot 10^{-4}$
5183	0.273	695	$4.1 \cdot 10^{-4}$

The estimated values in Table 12 were inserted into Hollomon's equation (Equation 22) to obtain a smoothed true stress-strain curve for each sample. These smoothed curves are shown in Figure 83a. The smoothed curve was further numerically derivated (by a central finite difference scheme) to acquire a curve showcasing the *strain hardening rate* ($d\sigma_t/d\epsilon_t$) evolution for the different wire materials, with increasing uniform true strain. This curve presented in Figure 83b.
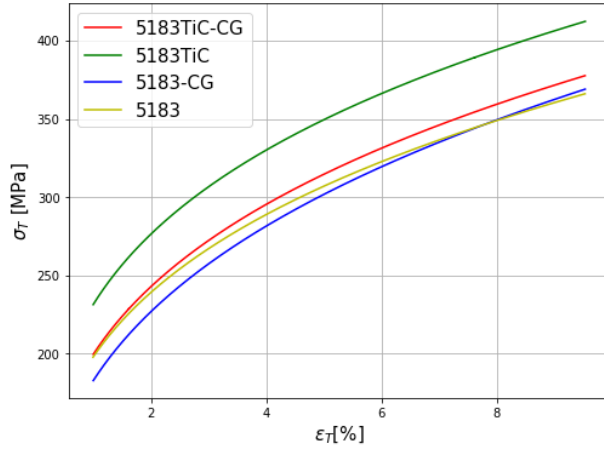
(a) Smoothed true stress-strain plot, approximated by Hollomon's equation.

(b) Strain hardening rate versus true strain. Obtained by numerical derivation of the smoothed curve in Figure 83a.

Figure 83: Smoothed and derivated curves for the uniforming strain region of the tensile curve for the DF screw extruded wire samples. The curves illustrate the strain hardening behaviour as the true strain increases.

High strain hardening rates are desired in the material as it may prolong the onset of localised deformation (necking) under tensile stress [81].

The curves in Figure 83b show that the strain hardening rate behaviour is similar for all wires, though slightly better for the 5183-CG wire. The numerical results in Table 12 indicate that the strain hardening exponent is larger for the wires extruded in CO_2-enriched atmosphere, 5183-CG and 5183TiC-CG. The enhanced strain hardening behaviour of the 5183-CG wire (versus 5183) may be explained by considering the mechanism illustrated in Figure 80 once more. When CO_2 gas is applied during screw extrusion, the formation of Mg-oxides is hindered, increasing the Mg content in solid solution. As shown by Ryen et al. [23], the strain hardening rate ($d\sigma_t/d\epsilon_t$) in Al-Mg alloys increase with the Mg content in solid solution. Thus, it may be assumed that the strain hardening rate increases for the 5183-CG wire due to the oxidation inhibition properties of the CO_2 cover gas. The same mechanism is believed to be responsible for the higher strain hardening coefficient, n in Table 12, of the 5183TiC-CG wire, compared with 5183TiC.

It may also be noticed from Table 12 that the strain hardening exponent n decreases with the addition of TiC nanoparticles. This might be attributed to the large interparticle spacing between the TiC nanoparticles. From e.g. Figure 61, it may be seen that the interparticle spacing is on the order of µm. It is suggested that the TiC nanoparticles act as *Frank-Read* sources [82], generating dislocations under tensile load. As a result of the large interparticle spacing, the dislocations responsible for strain hardening are formed far apart and will thus not hinder the propagation of other dislocations, but decrease the strength of the wire. Thus, the strain hardening properties of the wires are reduced with the addition of TiC nanoparticles.

5.7   Main effects of TiC nanoparticles

The main effects of adding TiC nanoparticles to the 5183 Al-Mg matrix may be summarised as follows:

- Yield strength and ultimate tensile strength is increased. This is attributed mainly to EM mismatch strengthening. The other strengthening mechanisms will have a larger effect after the TiC-reinforced wire is used for welding.

- Ductility decreases with the addition of TiC nanoparticles. This is likely a consequence of the brittle nature of the TiC.

- The grain size is reduced. The TiC nanoparticles have likely reduced the grain growth in the wires during the recrystallisation stages when the wire was screw extruded, through *Zener pinning*.

- Strain hardening properties are reduced. It is assumed that the decreasing effect on strain hardening is caused by the TiC nanoparticles acting as *Frank-Read* sources, generating dislocations which are spread too far apart to induce strain hardening under tensile loads.

6 Conclusions

Metal continuous screw extrusion (MCSE) is a solid state manufacturing method, operated at relatively low temperatures, with a wide range of different processable feedstock materials. In this thesis, MCSE was used to produce two different TiC reinforced aluminium matrix composite wires were manufactured. The key findings in this thesis are summarised below:

- An aluminium matrix composite wire reinforced with TiC nanoparticles was successfully manufactured through metal continuous screw extrusion (MCSE), introducing reinforcement particles to the matrix and forming the wire in a single step. MCSE is a solid state process, operated at relatively low temperatures. The reinforcement particles were uniformly distributed, in the composite wires, but present in rather low amounts. Both clusters and isolated TiC nanoparticles were found, with rather large interparticle spacing in the order of micrometers. To fully exploit the strengthening potential of the TiC nanoparticles in further applications, the fraction of particles should be increased and interparticle spacing reduced.

- Evidence of TiC agglomeration around Mg-oxide particles was found. This implies that TiC has attached to the Mg-oxides initially present on the feedstock granules during coating.

- The EBSD analysis showed that the grains in the TiC-containing wire were on average smaller than in the corresponding monolithic wire. This suggest that Zener pinning due to the presence of TiC nanoparticles has occured to some extent. The EBSD analysis also indicated that the grains were elongated in the extrusion direction, and that both wires had a weak {111} fiber texture.

- By introducing CO_2 gas to the screw extruder chamber, the porosity close to the wire edges was substantially reduced. It is believed that this effect may be attributed to the oxidation inhibiting properties of the CO_2 cover gas. CO_2 hinders the formation of Mg-oxides so that fewer Mg-hydroxides, and thus fewer pores, are formed in the wire.

- The mechanical properties was found to increase with the incorporation of TiC, although to a varying degree for the two different AMC wires extruded. It is assumed that the discrepancy in strengthening is caused by an unintentional reduction in the fraction of introduced TiC nanoparticles in the weaker wire.

- The strain hardening properties of the extruded wires increased with the addition of CO_2 gas during extrusion. It is believed that an enriched CO_2 atmosphere during screw extrusion inhibits oxidation of Mg in the Al-Mg alloy. Thus, the Mg content in solid solution in the Al-Mg matrix is increased. A higher Mg content in solid solution improves strain hardening of the wire during the tensile tests.

7 Further work

MCSE is a novel manufacturing technique, with multiple promising features. The continuous, low-temperature conditions facilitate for further safe and environmentally friendly development of new materials. In this work, it was shown that MCSE may successfully produce materials with a uniform distribution of reinforcement particles, a crucial requirement for aluminium matrix composite (AMC) manufacturing. Some challenges regarding the production of AMCs by MCSE still remain to be solved. A list including suggestions on further research work follows below:

- First, the 5183TiC-CG wire produced in this work should be drawn in order to reduce the diameter of the wire to a suitable size for welding applications. Further, it is believed that using this wire for Wire Arc Additive Manufacturing may yield stronger structures (due to the presence of TiC-nanoparticles), compared to a structure produced using a corresponding monolithic 5183 wire.

- Accurate mapping of pressure and strain (in addition to temperature) during MCSE to gain further knowledge on how the processing conditions affect the final product.

- Different alloy/reinforcement combinations may be explored to produce new, novel AMC materials. In particular, it is believed that the weldability of some Al alloys (e.g. in the 6xxx or 7xxx series) may be significantly enhanced through the introduction of TiC nanoparticles.

- A method to precisely determine the weight or volume fraction of the reinforcement particles is needed. Optical emission spark analysis (OES), which was used to analyse the chemical composition of the feedstock granules might prove useful for this. Quantitative analysis through X-ray diffraction analysis might also be used to determine the reinforcement particle content.

- To further improve the production of the 5183 matrix and TiC reinforcement system, a new TiC nanoparticle introduction procedure should be implemented to avoid clustering of TiC particles around surface oxides and to increase the TiC content in the extruded wires.

- The effect and mechanism of the CO_2 gas inhibition on Al-Mg solids should be verified through more tailored and accurate experiments.

References

[1] M. K. Surappa. 'Aluminium matrix composites: Challenges and opportunities'. In: *Sadhana* 28.1-2 (2003), pp. 319–334. ISSN: 0256-2499. DOI: `10.1007/BF02717141`.

[2] R. Casati and M. Vedani. 'Metal Matrix Composites Reinforced by Nano-Particles—A Review'. In: *Metals* 4.1 (2014), pp. 65–83. ISSN: 2075-4701. DOI: `10.3390/met4010065`.

[3] A. Contreras, E. Bedolla and R. Pérez. 'Interfacial phenomena in wettability of TiC by Al-Mg alloys'. In: *Acta Materialia* 52.4 (2004), pp. 985–994. ISSN: 13596454. DOI: `10.1016/j.actamat.2003.10.034`.

[4] W. Liu, C. Cao, J. Xu, X. Wang and X. Li. 'Molten salt assisted solidification nanoprocessing of Al-TiC nanocomposites'. In: *Materials Letters* 185 (Dec. 2016), pp. 392–395. ISSN: 0167577X. DOI: `10.1016/j.matlet.2016.09.023`.

[5] A.R. Kennedy, D.P. Weston and M.I. Jones. 'Reaction in Al–TiC metal matrix composites'. In: *Materials Science and Engineering: A* 316.1-2 (2001), pp. 32–38. ISSN: 09215093. DOI: `10.1016/S0921-5093(01)01228-X`.

[6] K. G. Skorpen. *Screw extrusion of light metals : development of materials, characterization and process analysis*. PhD Thesis 2018:218. NTNU Trondheim, 2018. URL: `http://hdl.handle.net/11250/2565656`.

[7] T. Stedje. *Characterization of Screw Extruded Rapid Solidified AA6061*. Master's Thesis. DMSE, NTNU Trondheim, 2014. URL: `http://hdl.handle.net/11250/249577`.

[8] T. Berulfsen. *Screw Extrusion from various Binary Al-XMg Feed Materials*. Master's thesis. DMSE, NTNU Trondheim, 2016. URL: `http://hdl.handle.net/11250/2409945`.

[9] K. S. Derekar. 'A review of wire arc additive manufacturing and advances in wire arc additive manufacturing of aluminium'. In: *Materials Science and Technology* 34.8 (2018), pp. 895–916. ISSN: 17432847. DOI: `10.1080/02670836.2018.1455012`.

[10] J. H. Martin, B. D. Yahata, J. M Hundley, J. A. Mayer, T. A. Schaedler and Tresa M. Pollock. '3D printing of high-strength aluminium alloys'. In: *Nature* 549.7672 (2017), pp. 365–369. ISSN: 0028-0836. DOI: `10.1038/nature23894`.

[11] W. D. Callister Jr. and D. G. Rethwisch. *Materials Science and Engineering, SI Version*. 9th ed. ISBN: 9781118319222.

[12] K. B. Oldham, J. C. Myland and A. M. Bond. *Electrochemical Science and Technology: Fundamentals and Applications*. John Wiley & Sons, 2013, pp. 71–73. ISBN: 978-0-470-71084-5.

[13] International Aluminium Institute. *Primary Aluminium Production*. Last visited: 09.05.2019. URL: `http://www.world-aluminium.org/statistics/#map`.

[14] J. K. Solberg. *Teknologiske metaller og legeringer*. Tapir Forlag, 2017.

[15] G. D. Totten and D. MacKenzie. *Handbook of Aluminum: Vol. 1: Physical Metallurgy and Processes*. Vol. 1. CRC press, 2003.

[16] J. R. Davis. *Aluminum and aluminum alloys*. ASM international, 1993. URL: http://hdl.handle.net/11115/173.

[17] F. Mazzolani. *Aluminium alloy structures*. CRC Press, 1994, pp. 8–9. ISBN: 0419177701.

[18] L. Becker. *Chemical elements by market price*. Last visited: 13.03.2019. URL: http://www.leonland.de/elements_by_price/en/list.

[19] T. C. Schulthess, P. E. A. Turchi, A. Gonis and T. G. Nieh. 'Systematic study of stacking fault energies of random Al-based alloys'. In: *Acta Materialia* 46.6 (1998), pp. 2215–2221. ISSN: 13596454. DOI: 10.1016/S1359-6454(97)00432-1.

[20] J. L. Murray. 'The Al-Mg (Aluminum-Magnesium) system'. In: *Journal of Phase Equilibria* 3.1 (1982), p. 60. ISSN: 1054-9714. DOI: 10.1007/BF02873413.

[21] E. L. Huskins, B. Cao and K.T. Ramesh. 'Strengthening mechanisms in an Al–Mg alloy'. In: *Materials Science and Engineering: A* 527.6 (2010), pp. 1292–1298. ISSN: 09215093. DOI: 10.1016/j.msea.2009.11.056.

[22] Ø. Ryen, H. I. Laukli, B. Holmedal and E. Nes. 'Large strain work hardening of aluminum alloys and the effect of mg in solid solution'. In: *Metallurgical and Materials Transactions A* 37.6 (2006), pp. 2007–2013. ISSN: 1073-5623. DOI: 10.1007/s11661-006-0143-6.

[23] Ø. Ryen, B. Holmedal, O. Nijs, E. Nes, E. Sjölander and H. E. Ekström. 'Strengthening mechanisms in solid solution aluminum alloys'. In: *Metallurgical and Materials Transactions A* 37.6 (2006), pp. 1999–2006. ISSN: 1073-5623. DOI: 10.1007/s11661-006-0142-7.

[24] A. H. Cottrell. 'LXXXVI. A note on the Portevin-Le Chatelier effect'. In: *The London, Edinburgh, and Dublin Philosophical Magazine and Journal of Science* 44.355 (1953), pp. 829–832. DOI: 10.1080/14786440808520347.

[25] A. Portevin and F. Le Chatelier. 'Sur un phénomène observé lors de l'essai de traction d'alliages en cours de transformation'. In: *Comptes Rendus de l'Académie des Sciences Paris* 176 (1923), pp. 507–510.

[26] A. Yilmaz. 'The Portevin-Le Chatelier effect: A review of experimental findings'. In: *Science and Technology of Advanced Materials* 12.6 (2011). ISSN: 14686996. DOI: 10.1088/1468-6996/12/6/063001.

[27] A. Van Den Beukel. 'Theory of the effect of dynamic strain aging on mechanical properties'. In: *Physica Status Solidi (a)* 30.1 (1975), pp. 197–206. ISSN: 00318965. DOI: 10.1002/pssa.2210300120.

[28] A. Yilmaz. 'Temperature and surface potential correlations with serrated flow of low carbon steel'. In: *Journal of Materials Science* 46.11 (2011), pp. 3766–3776. ISSN: 00222461. DOI: 10.1007/s10853-011-5290-5.

[29] S. Serajzadeh and H. Sheikh. 'Investigation into occurring dynamic strain aging in hot rolling of AA5083 using finite elements and stream function method'. In: *Materials Science and Engineering: A* 486.1-2 (2008), pp. 138–145. ISSN: 09215093. DOI: 10.1016/j.msea.2007.09.021.

[30] K. Wefers. 'Properties and characterization of surface oxides on aluminium alloys'. In: Leoben and Vienna: 7th International Light Metals Congress, 1981.

[31] N. Smith. *Methods of oxidation inhibition for Al-Mg alloys*. PhD Thesis 2019:29. NTNU Trondheim, 2019.

[32] K. Wefers and C. Misra. *Oxides and Hydroxides of Aluminum*. Pittsburgh, PA: Alcoa Laboratories, 1987, p. 65. URL: http://epsc511.wustl.edu/Aluminum_Oxides_Alcoa1987.pdf.

[33] C. Lea and J. Ball. 'The oxidation of rolled and heat treated Al-Mg alloys'. In: *Applications of Surface Science* 17.3 (1984), pp. 344–362. ISSN: 03785963. DOI: 10.1016/0378-5963(84)90023-0.

[34] D. R. Gaskell. *Introduction to the thermodynamics of materials*. 4th ed. New York: Taylor & Francis, 2003. ISBN: 1560329920.

[35] Department of Health and Human Services Agency for Toxic Substances and Disease Registry. *Beryllium Toxicity: Patient Education Care Instruction Sheet*. Last visited: 29.04.2019. URL: https://www.atsdr.cdc.gov/csem/csem.asp?csem=5&po=15..

[36] C. N. Cochran, D. L. Belitskus and D. L. Kinosz. 'Oxidation of aluminum-magnesium melts in air, oxygen, flue gas, and carbon dioxide'. In: *Metallurgical Transactions B* 8.1 (1977), pp. 323–332. ISSN: 0360-2141. DOI: 10.1007/BF02657663.

[37] N. Smith, B. Gleeson, W. A. Saidi, A. Kvithyld and G. Tranell. 'Mechanism behind the Inhibiting Effect of CO 2 on the Oxidation of Al–Mg Alloys'. In: *Industrial & Engineering Chemistry Research* 58.3 (2019), pp. 1434–1442. ISSN: 0888-5885. DOI: 10.1021/acs.iecr.8b04691.

[38] M. Manoharan and M. Gupta. 'Effect of silicon carbide volume fraction on the work hardening behaviour of thermomechanically processed aluminium-based metal–matrix composites'. In: *Composites Part B: Engineering* 30.1 (1999), pp. 107–112. ISSN: 13598368. DOI: 10.1016/S1359-8368(98)00041-9.

[39] N. Chawla and Y. Shen. 'Mechanical Behavior of Particle Reinforced Metal Matrix Composites'. In: *Advanced Engineering Materials* 6 (2001), pp. 357–370. ISSN: 14381656. DOI: 10.1002/1527-2648(200106)3:6{\%}3C357::AID-ADEM357{\%}3E3.0.CO;2-I.

[40] T. E. Quested. 'Understanding mechanisms of grain refinement of aluminium alloys by inoculation'. In: *Materials Science and Technology* 20.11 (Nov. 2004), pp. 1357–1369. ISSN: 0267-0836. DOI: 10.1179/026708304225022359.

[41] D. K. Das, P. C. Mishra, S. Singh and R. K. Thakur. 'Properties of ceramic-reinforced aluminium matrix composites - a review'. In: *International Journal of Mechanical and Materials Engineering* 9.1 (2014), p. 12. ISSN: 1823-0334. DOI: 10.1186/s40712-014-0012-9.

[42] Hülya Kaftelen, Necip Ünlü, Gültekin Göller, M. Lütfi Öveçoğlu and Hani Henein. 'Comparative processing-structure–property studies of Al–Cu matrix composites reinforced with TiC particulates'. In: *Composites Part A: Applied Science and Manufacturing* 42.7 (2011), pp. 812–824. ISSN: 1359835X. DOI: 10.1016/j.compositesa.2011.03.016.

[43] A. E. Karantzalis, A. Lekatou, E. Georgatis, V. Poulas and H. Mavros. 'Microstructural observations in a cast Al-Si-Cu/TiC composite'. In: *Journal of Materials Engineering and Performance* 19.4 (2010), pp. 585–590. ISSN: 10599495. DOI: 10.1007/s11665-009-9505-8.

[44] A. R. Kennedy, A. E. Karantzalis and S. M. Wyatt. 'The microstructure and mechanical properties of Al-Si-B4C metal matrix composites'. In: *Journal of Materials Science* 34.2 (1999), pp. 933–940. ISSN: 00222461. DOI: 10.1023/A: 1013600328599.

[45] P. A. Manohar, M. Ferry and T. Chandra. 'Five Decades of the Zener Equation.' In: *ISIJ International* 38.9 (1998), pp. 913–924. ISSN: 0915-1559. DOI: 10.2355/isijinternational.38.913.

[46] A. Sanaty-Zadeh. 'Comparison between current models for the strength of particulate-reinforced metal matrix nanocomposites with emphasis on consideration of Hall–Petch effect'. In: *Materials Science and Engineering: A* 531 (2012), pp. 112–118. ISSN: 09215093. DOI: 10.1016/j.msea.2011.10.043.

[47] M. Fattahi, V. Noei Aghaei, A. R. Dabiri, S. Amirkhanlou, S. Akhavan and Y. Fattahi. 'Novel manufacturing process of nanoparticle/Al composite filler metals of tungsten inert gas welding by accumulative roll bonding'. In: *Materials Science and Engineering A* 648 (2015), pp. 47–50. ISSN: 09215093. DOI: 10.1016/j.msea.2015.09.053.

[48] J. W. Luster, M. Thumann and R. Baumann. 'Mechanical properties of aluminium alloy 6061–Al2O3 composites'. In: *Materials Science and Technology* 9.10 (1993), pp. 853–862. ISSN: 0267-0836. DOI: 10.1179/mst.1993.9.10. 853.

[49] D. Hull and D. J. Bacon. 'Chapter 7 - Jogs and the Intersection of Dislocations'. In: *Introduction to Dislocations.* 5. edition. Oxford: Butterworth-Heinemann, 2011, pp. 137–155. ISBN: 978-0-08-096672-4. DOI: 10.1016/B978-0-08-096672-4.00007-4.

[50] Z. Zhang and D. L. Chen. 'Consideration of Orowan strengthening effect in particulate-reinforced metal matrix nanocomposites: A model for predicting their yield strength'. In: *Scripta Materialia* 54.7 (2006), pp. 1321–1326. ISSN: 13596462. DOI: 10.1016/j.scriptamat.2005.12.017.

[51] J. Moon, S. Kim, J. Jang, J. Lee and C. Lee. 'Orowan strengthening effect on the nanoindentation hardness of the ferrite matrix in microalloyed steels'. In: *Materials Science and Engineering: A* 487.1-2 (2008), pp. 552–557. ISSN: 09215093. DOI: 10.1016/j.msea.2007.10.046.

[52] R. M. Aikin and L. Christodoulou. 'The role of equiaxed particles on the yield stress of composites'. In: *Scripta Metallurgica et Materiala* 25.1 (1991), pp. 9–14. ISSN: 0956716X. DOI: 10.1016/0956-716X(91)90345-2.

[53] Z. Zhang and D.L. Chen. 'Contribution of Orowan strengthening effect in particulate-reinforced metal matrix nanocomposites'. In: *Materials Science and Engineering: A* 483-484.1-2 C (2008), pp. 148–152. ISSN: 09215093. DOI: 10.1016/j.msea.2006.10.184.

[54] F. Mirza and D. Chen. 'A Unified Model for the Prediction of Yield Strength in Particulate-Reinforced Metal Matrix Nanocomposites'. In: *Materials* 8.8 (Aug. 2015), pp. 5138–5153. ISSN: 1996-1944. DOI: 10.3390/ma8085138.

[55] M. Fattahi, M. Mohammady, N. Sajjadi, M. Honarmand, Y. Fattahi and S. Akhavan. 'Effect of TiC nanoparticles on the microstructure and mechanical properties of gas tungsten arc welded aluminum joints'. In: *Journal of Materials Processing Technology* 217 (2015), pp. 21–29. ISSN: 09240136. DOI: 10.1016/j.jmatprotec.2014.10.023.

[56] A.J. Knowles, X. Jiang, M. Galano and F. Audebert. 'Microstructure and mechanical properties of 6061 Al alloy based composites with SiC nanoparticles'. In: *Journal of Alloys and Compounds* 615.S1 (2014), S401–S405. ISSN: 09258388. DOI: 10.1016/j.jallcom.2014.01.134.

[57] S.J. Hong, H.M. Kim, D. Huh and C. Suryanarayana. 'Effect of clustering on the mechanical properties of SiC particulate-reinforced aluminum alloy 2024 metal matrix composites'. In: *Materials Science and Engineering A* 347 (2003), pp. 198–204. DOI: 10.1016/S0921-5093(02)00593-2.

[58] V. V. Bhanu Prasad, B. V.R. Bhat, Y. R. Mahajan and P. Ramakrishnan. 'Structure-property correlation in discontinuously reinforced aluminium matrix composites as a function of relative particle size ratio'. In: *Materials Science and Engineering A* 337.1-2 (2002), pp. 179–186. ISSN: 09215093. DOI: 10.1016/S0921-5093(02)00024-2.

[59] Q. F. Li and D. G. McCartney. 'Nucleation of an Al alloy in a fibre reinforced Al alloy metal-matrix composite (MMC)'. In: *Journal of Materials Processing Technology* 51.1-4 (1995), pp. 235–243. ISSN: 09240136. DOI: 10.1016/0924-0136(94)01592-0.

[60] D. G. McCartney. 'Grain refining of aluminium and its alloys using inoculants'. In: *International Materials Reviews* 34.1 (1989), pp. 247–260. ISSN: 0950-6608. DOI: 10.1179/imr.1989.34.1.247.

[61] A. Contreras, C. Angeles-Chávez, O. Flores and R. Perez. 'Structural, morphological and interfacial characterization of Al-Mg/TiC composites'. In: *Materials Characterization* 58 (2007), pp. 685–693. ISSN: 10445803. DOI: 10.1016/j.matchar.2006.11.031.

[62] A. Contreras, A. Albiter, E. Bedolla and R. Pérez. 'Processing and characterization of Al-Cu and Al-Mg base composites reinforced with TiC'. In: *Advanced Engineering Materials* 6.9 (2004), pp. 767–775. ISSN: 14381656. DOI: `10.1002/adem.200400102`.

[63] K. B. Lee, H. S. Sim and H. Kwon. 'Reaction products of Al/TiC composites fabricated by the pressureless infiltration technique'. In: *Metallurgical and Materials Transactions A* 36.9 (2005), pp. 2517–2527. ISSN: 1073-5623. DOI: `10.1007/s11661-005-0125-0`.

[64] T. Sakai. 'Screw extrusion technology — past , present and future'. In: *Polimery* 58.11-12 (2013), pp. 847–857. URL: `http://en.www.ichp.pl/attach.php?id=2121`.

[65] F. Widerøe and T. Welo. 'Using contrast material techniques to determine metal flow in screw extrusion of aluminium'. In: *Journal of Materials Processing Technology* 213.7 (2013), pp. 1007–1018. ISSN: 09240136. DOI: `10.1016/j.jmatprotec.2012.11.013`.

[66] C. I. Chung. *Physical Description of Single-Screw Extrusion.* 2. edition. Munich: Hanser Publishers, 2000. ISBN: 9781569904596.

[67] J. Werenskiold, L. Auran, H. J. Roven, N. Ryum and O. Reiso. *Screw extruder for continous extrusion of materials with high viscosity.* International patent number: EP2086697B1 WO2008 06307. Patent reference: JP-A-2004 035 961, US-A-2 787 022.

[68] J. Cui. *Solid state recycling of aluminium scrap and dross characterization.* PhD Thesis 2011:325. NTNU Trondheim, 2011. URL: `http://hdl.handle.net/11250/2464964`.

[69] J. R. Duflou, A. Tekkaya, M. Haase, T. Welo, K. Vanmeensel, K. Kellens, W. Dewulf and D. Paraskevas. 'Environmental assessment of solid state recycling routes for aluminium alloys: Can solid state processes significantly reduce the environmental impact of aluminium recycling?' In: *CIRP Annals - Manufacturing Technology* 64.1 (2015), pp. 37–40. ISSN: 17260604. DOI: `10.1016/j.cirp.2015.04.051`.

[70] M. Sokoluk, C. Cao, S. Pan and X. Li. 'Nanoparticle-enabled phase control for arc welding of unweldable aluminum alloy 7075'. In: *Nature Communications* 10.1 (2019), p. 98. ISSN: 2041-1723. DOI: `10.1038/s41467-018-07989-y`.

[71] S. Ford and M. Despeisse. 'Additive manufacturing and sustainability: an exploratory study of the advantages and challenges'. In: *Journal of Cleaner Production* 137 (2016), pp. 1573–1587. ISSN: 09596526. DOI: `10.1016/j.jclepro.2016.04.150`.

[72] M. Alamir. *Wire-Arc Additive Manufacturing (WAAM).* Last visited: 12.03.2019, 2018. URL: `https://facadeworld.com/2018/04/28/wire-arc-additive-manufacturing-waam/`.

[73] W. E. Frazier. 'Metal additive manufacturing: A review'. In: *Journal of Materials Engineering and Performance* 23.6 (2014), pp. 1917–1928. ISSN: 15441024. DOI: `10.1007/s11665-014-0958-z`.

[74]   S. W. Williams, F. Martina, A. C. Addison, J. Ding, G. Pardal and P. Colegrove. 'Wire + Arc Additive Manufacturing'. In: *Materials Science and Technology* 32.7 (2016), pp. 641–647. ISSN: 0267-0836. DOI: `10.1179/1743284715Y.0000000073`.

[75]   E.O. Olakanmi, R.F. Cochrane and K.W. Dalgarno. 'A review on selective laser sintering/melting (SLS/SLM) of aluminium alloy powders: Processing, microstructure, and properties'. In: *Progress in Materials Science* 74 (2015), pp. 401–477. ISSN: 00796425. DOI: `10.1016/j.pmatsci.2015.03.002`.

[76]   *Gas Density*. Last visited: 03.06.2019. URL: `http://www.valvias.com/miscellanea-material-properties-gases-density.php`.

[77]   S. Wright. *Texture Analysis - Fibers & Components*. Tech. rep. EDAX-TSL, 2003, pp. 1–11.

[78]   A.G. Blackman, L.R. Gahan, G. Aylward and T. Findlay. *Aylward and Findlay's SI Chemical Data*. Milton, 2014.

[79]   *Wire types and sizes*. Tech. rep. Last visited: 12.06.2019: Hare & Forbes Machinery House. URL: `https://images.machineryhouse.com.au/products/K019A/PDF/Welding-Wire-Diameter-CHART.pdf`.

[80]   G. Langelandsvik. *Optimization of Electrical Conductivity in Screw Extruded Wires*. Master's Thesis. DMSE, NTNU Trondheim, 2017. URL: `http://hdl.handle.net/11250/2454123`.

[81]   M. Li, H. Zhai, Z. Huang, X. Liu, Y. Zhou, S. Li and C. Li. 'Tensile behavior and strengthening mechanism in ultrafine TiC0.5 particle reinforced Cu–Al matrix composites'. In: *Journal of Alloys and Compounds* 628 (Apr. 2015), pp. 186–194. ISSN: 09258388. DOI: `10.1016/j.jallcom.2014.10.123`.

[82]   F. C. Frank and W. T. Read. 'Multiplication Processes for Slow Moving Dislocations'. In: *Phys. Rev.* 79.4 (1950), pp. 722–723. DOI: `10.1103/PhysRev.79.722`.

Appendices

A   5183 Welding Wire Datasheet

Mig Wires Safra 5183.pdf

Aluminium Mig Wires | Safra 5183

Key Facts
- Precision layer wound, double diamond shaved wire
- Excellent feedability and arc control
- Very high quality welds
- Excellent where sea water corrosion resistance is required

Description
Recognised as the highest quality aluminum welding wire. Precision layer wound and double diamond shaved for superior feed ability. Designed to meet the tensile strength requirements of high magnesium alloys. Clearly the professional's choice.

Classifications, Approvals & Conformances
AWS A5.10 ER5183
ABS - American Bureau of Shipping
DNV - Det Norske Veritas
Lloyd's Register of Shipping

Applications
5183 is used where high sea water corrosions resistance is needed.   Applications include construction of ships, storage tanks and in the automotive industry.
- General aluminium fabrication and repairs on boats and ships
- Bullbars and rollbars
- Storage tanks
- Welding of many aluminium alloys where higher strength is required

Recommended Shielding Gas
100% Argon / Helium Mixtures Flow Rate: 30 - 50 CFH

Welding Positions
All positions

Typical Wire Analysis

Cu - Copper	Mn - Manganese	Si - Silicon	Zr - Zirconium
< 0.05	0.60 – 1.0	< 0.25	-
Zn - Zinc	**Ti - Titanium**	**Mg - Magnesium**	**Cr - Chromium**
< 0.25	< 0.15	4.30 – 5.20	0.05 – 0.25
Fe - Iron	**Ai - Aluminium**		
< 0.40	Balance		

Typical Weld Mechanical Properties

0.2% Proof Stress	> 125N/mm^2
Elongation	> 17%
Tensile Strength:	> 275N/mm^2

Packaging & Ordering Information

Size	Packet	Part Number
0.9mm	6kg	200217S
1.0mm	6kg	200218S
1.2mm	6kg	200219S
1.6mm	6kg	200220S

Operational Data

Wire Size	Welding Current Range (A)	Arc Voltage Range *(V)
1.2mm	150 – 250	20 - 27
1.6mm	200 – 350	23 - 30

Disclaimer: The above information is provided as a guide; actual welding current and voltage will depend on the welding machine characteristics, which will vary from model to model. Other variables include run length and size, plate thickness, operator technique and gas type (if used). The user must evaluate the process, application and recommended professional advice. Under no circumstance will Dynaweld or its affiliates be liable for misuse or application of products this is entirely up to the user's ability.

www.safrawelding.com.au
Dynaweld Industrial Supplies Pty Ltd is the official Australian distributor for Safra products | +61 2 9772 1144

B SEM and EDS analysis of TiC-coated granules

The feedstock material used in the screw extrusion of AMCs (5183-TiC) was invest-igated using an electron microscope. The granules were gently rolled on a carbon-tape before being inserted into the vacuum chamber of the *Ultra* LVFESEM, to remove "loose" TiC particles from the granule the avoid contamination of the SEM chamber. A SEM image of the granule surface is included in Figure 84.
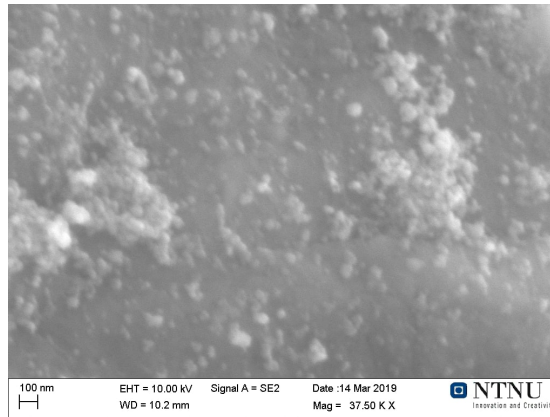
Figure 84: Secondary SEM image of the surface of a TiC-coated Al-granule, used as raw material for the screw extrusion process.

The same area as shown in Figure 84 was analysed using an EDS spot scan to confirm that the white particles are TiC. The spots analysed are indicated in Figure 85.
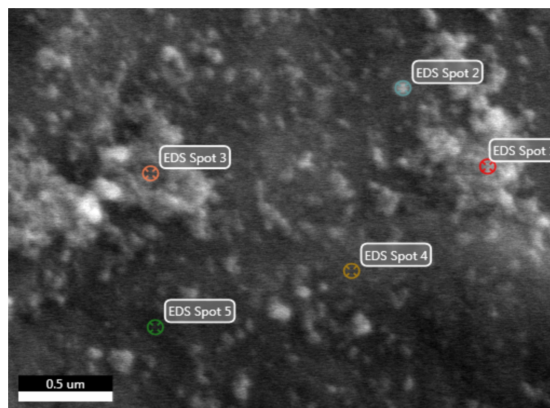
Figure 85: Secondary SEM image of the surface of a TiC-coated Al-granule, used as raw material for the screw extrusion process. Spots 1–4 were analysed using EDS.

The EDS signals from spots 1-4 in Figure 85 are shown in Figure 86. Spot 5 showed the same signals as spot 4, and was thus disregarded.
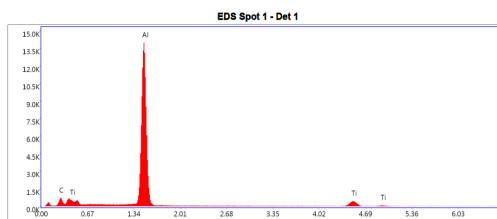
(a) EDS-spectrum for spot 1, indicating TiC.
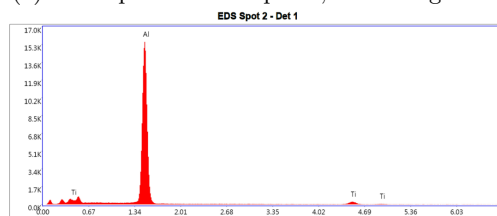
(b) EDS-spectrum for spot 2, indicating TiC.
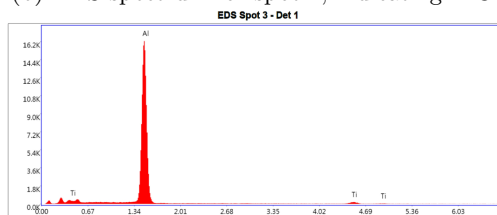
(c) EDS-spectrum for spot 3, indicating TiC.
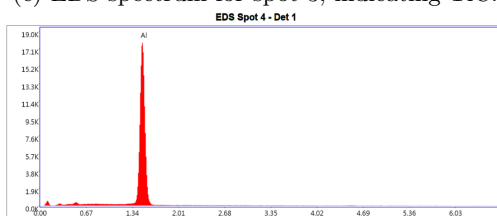
(d) EDS-spectrum for spot 4, indicating that the matrix is Al.

Figure 86: EDS-spectra for the spots in Figure 85.

The results from the EDS analysis in Figure 86 confirms that the bright spheres on the Al-granule surface are TiC particles. The peaks at $\approx 4.5\,\mathrm{keV}$ are characteristic for Ti.

A rough size-estimate of some TiC particles is included in Figure 87. The diameters of the particles were measured using a built-in measuring function in the SEM software.
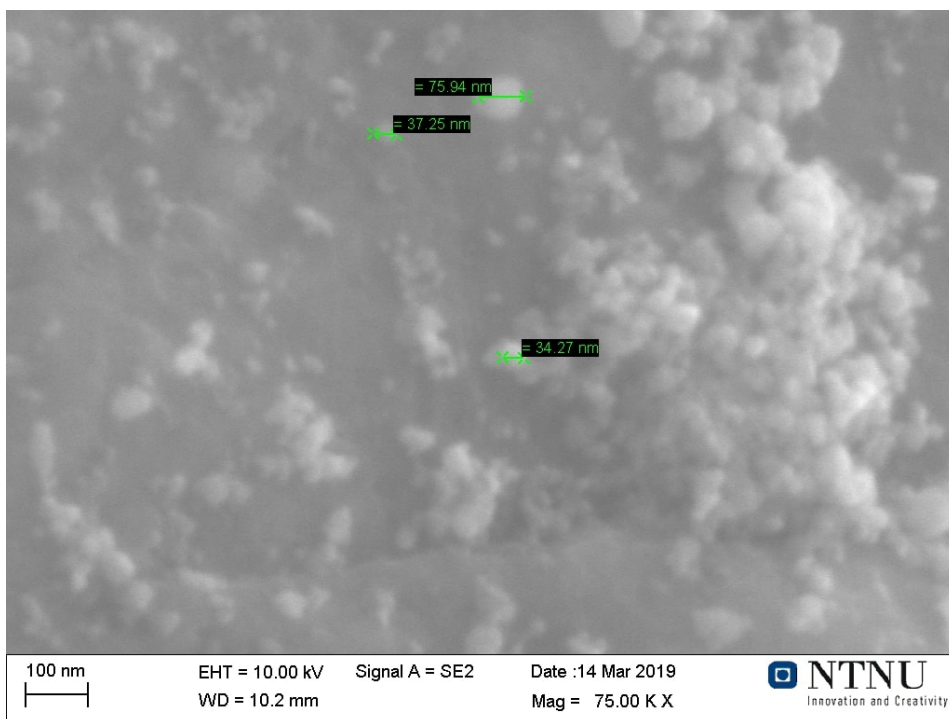
Figure 87: Secondary electron micrograph of the surface of a Al-granule covered with TiC particles, with inserted diameter measurements.

The SEM image above confirms that the size of the TiC particles are in the vicinity of 50 nm (i.e near the SEM resolution limit), as was expected from the specifications from the manufacturer of the TiC particles; **US Research Nanomaterials Inc.**. A precise determination of the size of the particles needs more accurate tools.

C 4043 and 4043+5183TiC wires

In this section, the experimental conditions and results from investigations and testing of the 4043 and 4043+5183TiC wire are presented. Both wires were extruded in the same extrusion session, by first extruding pure 4043, then adding 5183TiC granules to the extruder, so that a mixed 4043+5183TiC wire was produced. The wires were extruded using a single flight (SF) screw. The detailed experimental procedure may be found in Table 4 and Figure 30.

C.1 Temperature evolution

The temperature evolution during the single flight (SF) screw extrusion of the 4043 and 4043+5183TiC wires is shown in Figure 88.
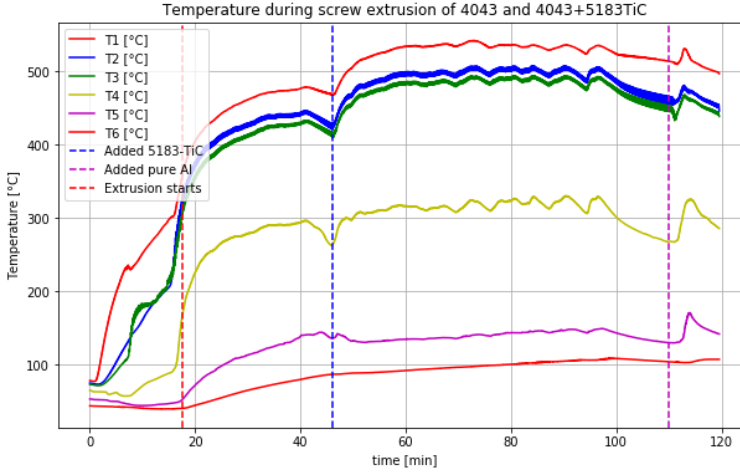
Figure 88: Temperature evolution during screw extrusion of 5183TiC+4043 wire in ambient atmosphere. The placement of the temperature sensors are as follows. T1: Die, T2: Extrusion chamber left, T3: Extrusion chamber right, T4: screw channel front, T5: Screw channel rear, T6: Screw stem.

First, the 4043 granules were added and extruded until ≈ 45 min, when the TiC-coated 5183 granules were added. Thus, before 45 min a 4043 wire was extruded. After 45 min, a wire consisting of mixed 4043 and 5183-TiC was extruded. Later SEM analysis confirmed that the 4043 material remained in the screw channel long after the 5183-TiC granules were added. This shows that it is not possible to extrude to different two different, pure wires in the same MCSE session, as the material which is added first will remain within the screw extruded for extended periods.

C.2 Microstructure

SEM images of the longitudinal cross sectional plane of the 4043+5183TiC wire, showing the presence of both the 5183-TiC (Mg-rich) phase and the 4043 phase, are presented in Figure 89.
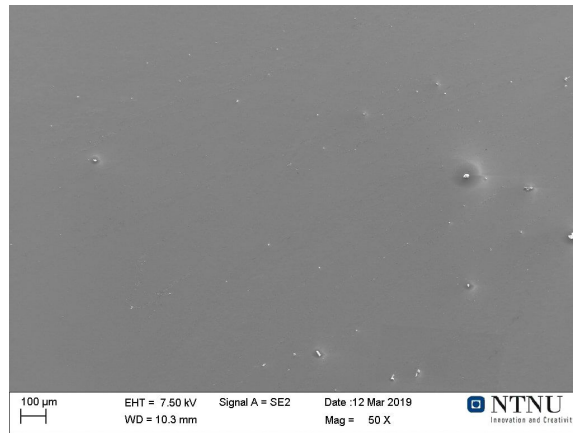
(a) Secondary electron image.
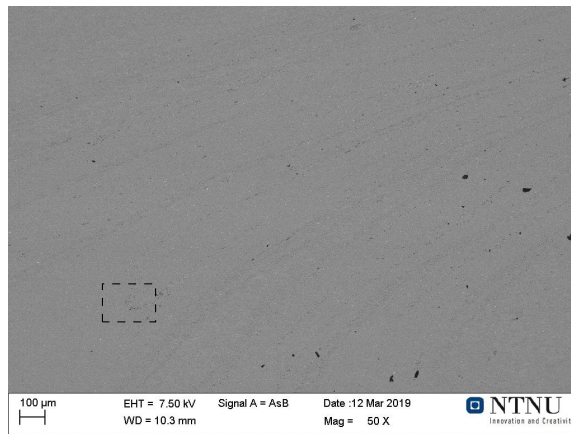
(b) Backscattered electron image. The area within the dashed box was further examined at larger magnifications, as shown in Figure 91a.

Figure 89: SEM micrographs of the longitudinal cross section of the 4043+5183TiC wire.

Since the bright particles in Figure 89 are only visible in the secondary electron image Figure 89a, they may be assumed to be surface impurities.

The area in Figure 89 was EDS-mapped, as shown in Figure 90.
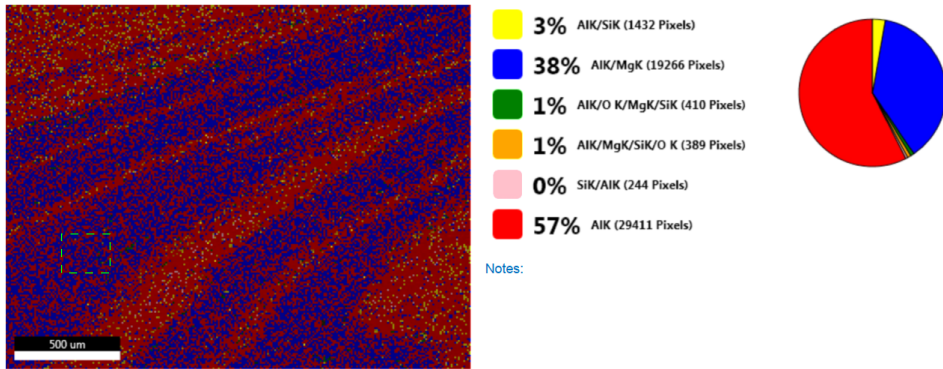
Figure 90: EDS mapping of the 4043+5183TiC wire sample, longitudinal cross section.

Since the 5183-TiC phase contains Mg, and the 4043 phase does not, it is easy to distinguish the two. Figure 90 shows that the sample has an alternating structure of 5183-TiC (blue) and 4043 (red). The area within the dashed box seen in Figure 89b, corresponding to the green box in Figure 90 in the blue 5183-TiC area, was imaged at higher magnification, as shown in Figure 91a. The characteristic Ti x-ray signals from an EDS mapping analysis of this area are presented in Figure 91b.
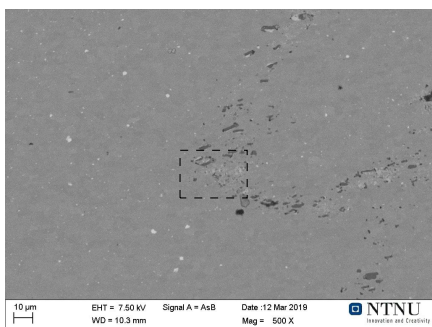
(a) Backscattered electron image.
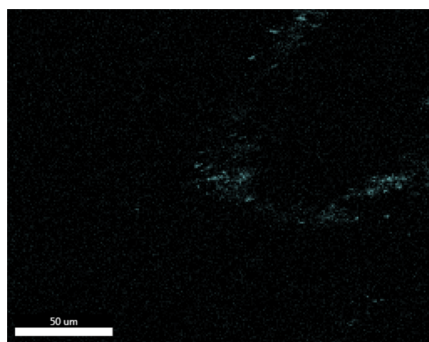
(b) Ti signals from EDS mapping.

Figure 91: SEM and EDS analysis of the longitudinal cross section of the 4043+5183TiC magnification.

Figure 91b shows that Ti-rich particles have agglomerated in the vicinity of the dark phases in Figure 91a. The area indicated by the black box in Figure 91a is further imaged at higher magnification in Figure 92.
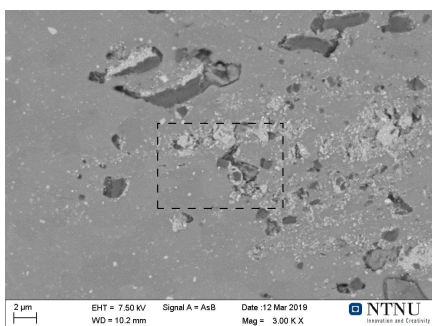
(a) Backscattered electron image.
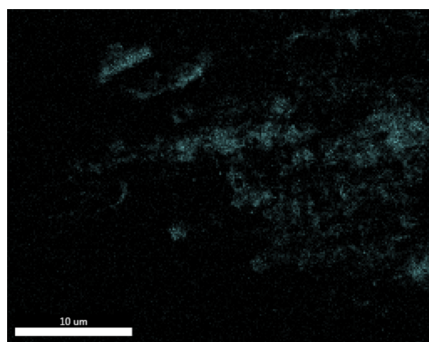
(b) Ti signals from EDS mapping.

Figure 92: SEM and EDS analysis of the longitudinal cross section of the 4043+5183TiC wire at 3000X magnification.

From Figure 92b it is clear that Ti-containing particles have accumulated near the dark phases in Figure 92a. The area inside the inserted box was further analysed at higher magnification in Figure 93.
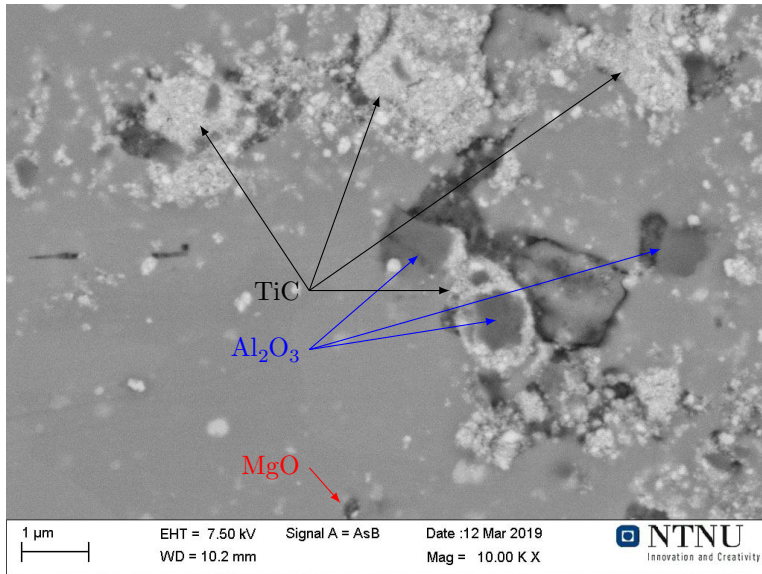
(a) Backscattered electron image.
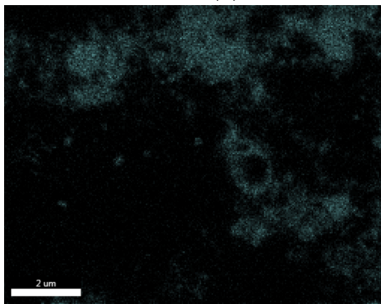
(b) Ti EDS-signals.
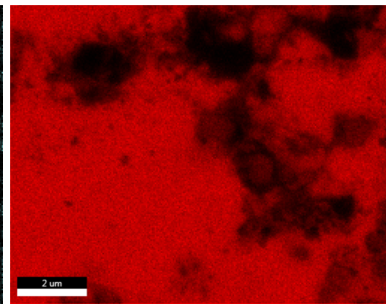
(c) Al EDS-signals.
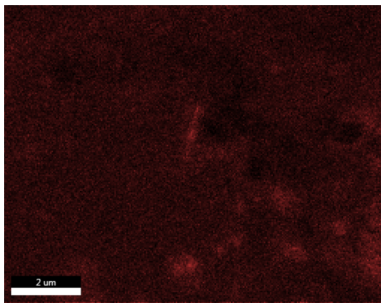
(d) Mg EDS-signals.
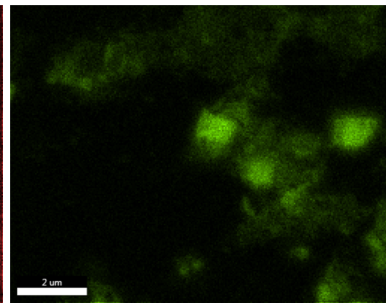
(e) O EDS-signals.

Figure 93: SEM and EDS analysis of the longitudinal cross section of the 4043+5183TiC wire at 10 000X magnification.

C.3 EBSD

An EBSD orientation map, along with the inverse pole figure (relative to the normal direction out of the image plane), from the 4043+5183TiC wire is included in Figure 94. The investigated area shows the interface between the 4043 phase and the 5183TiC phase in a longitudinal 4043+5183TiC sample.
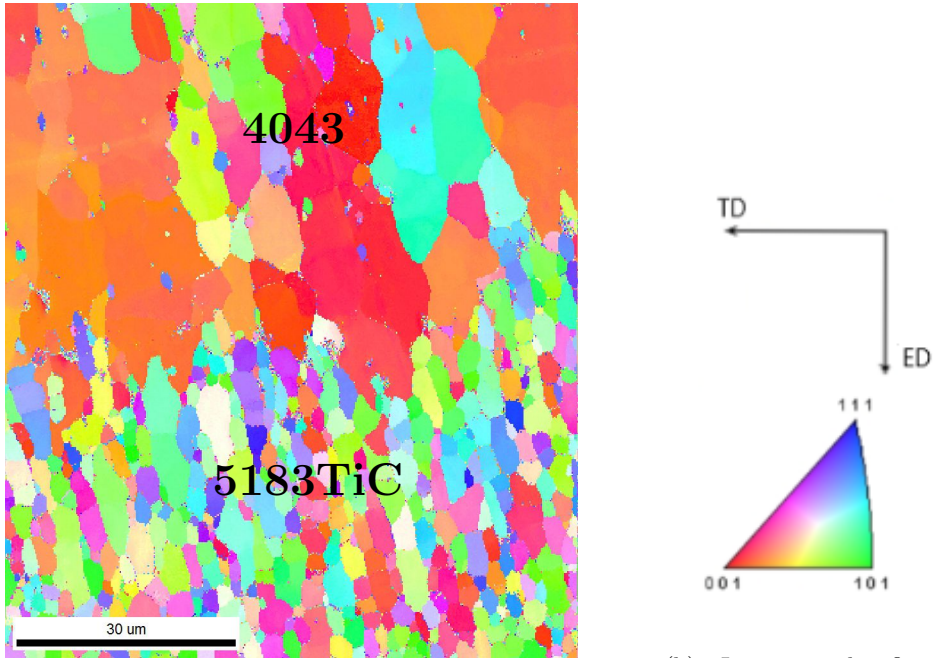
(a) Orientation map. The smalls grains are 5183-TiC, the large ones are 4043.

(b) Inverse pole figure indicating, the crystallographic directions.

Figure 94: Orientation map and inverse pole figure (IPF) acquired by an EBSD analysis of longitudinal cross-section of the 4043+5183TiC wire. Extrusion direction (ED) is downwards in the image. The crystallographic directions in the IPF are relative to the image plane normal.

Figure 94 indicates a distinct size difference between the 5183-TiC grains and the 4043 grains. Some of this difference may be attributed to the Zener pinning of the TiC nanoparticles, which will restrict grain growth during the recrystallisation that occurs after extrusion.

An image quality map, with superimposed low (yellow) and high (blue) angle grain boundaries is included in Figure 95
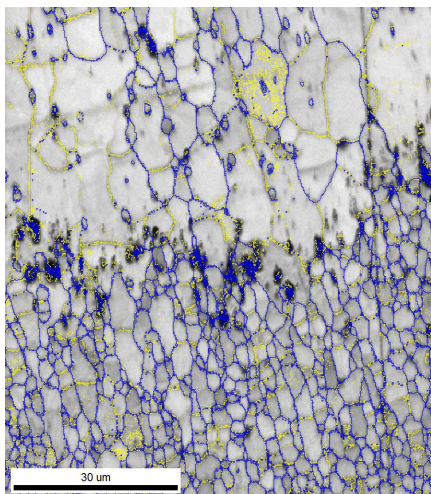
(a) Misorientation of grain boundaries in 4043+5183TiC wire.
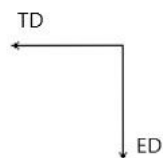
(b) Designation of low-angle and high-angle grain boundaries.

Figure 95: Investigation of grain boundaries in a 4043+5183TiC longtiudinal sample.

C.4 Mechanical properties

The results from tensile testing of the representative single flight wire samples are shown in Figure 96.
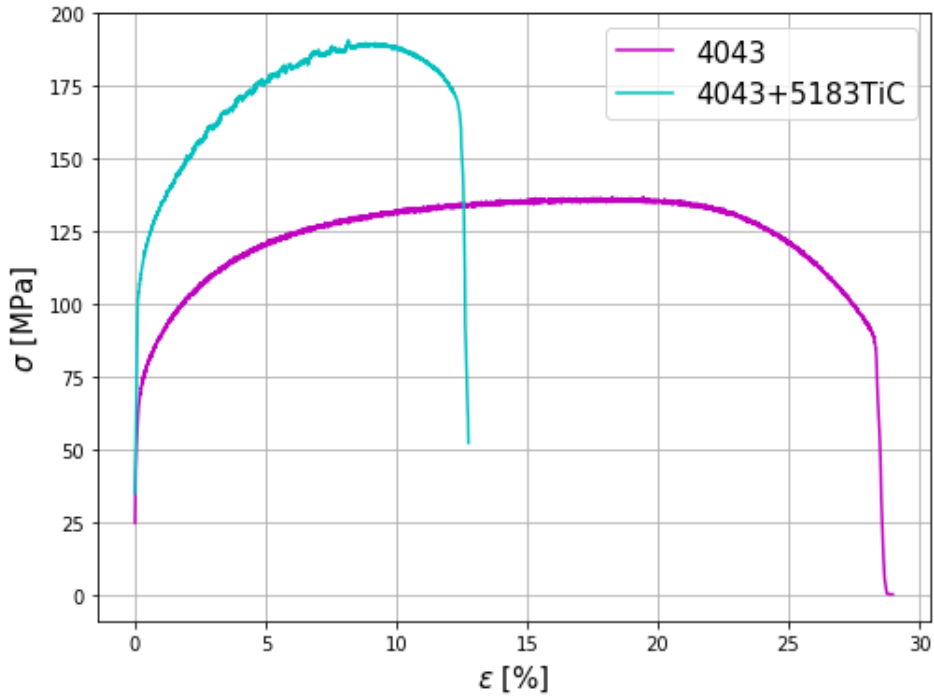
Figure 96: Engineering stress-strain curves from the tensile test of representative SF-screw wire samples.

The measured yield strength (σ_Y), ultimate tensile strength (σ_{UTS}) and elongation (EL) at fracture for the samples above are included in Table 13.

Table 13: Yield strength (σ_Y), ultimate tensile strength (σ_{UTS}) and elongation (EL) at fracture for the SF screw extruded wires.

Wire	σ_Y [MPa]	σ_{UTS} [MPa]	EL [%]
4043	81	137	29
4043+5183TiC	120	191	13

The Vickers microhardness ($HV_{0.1}$) was measured along the diameter of the wires, as shown in Figure 97. The measured hardness values for each indent along the diagonal is superimposed on the image. An additional 7 indents measuring the hardness of the 5183TiC-phase in the 4043+5183TiC wire may be seen within the dashed, green rectangle in Figure 97a.
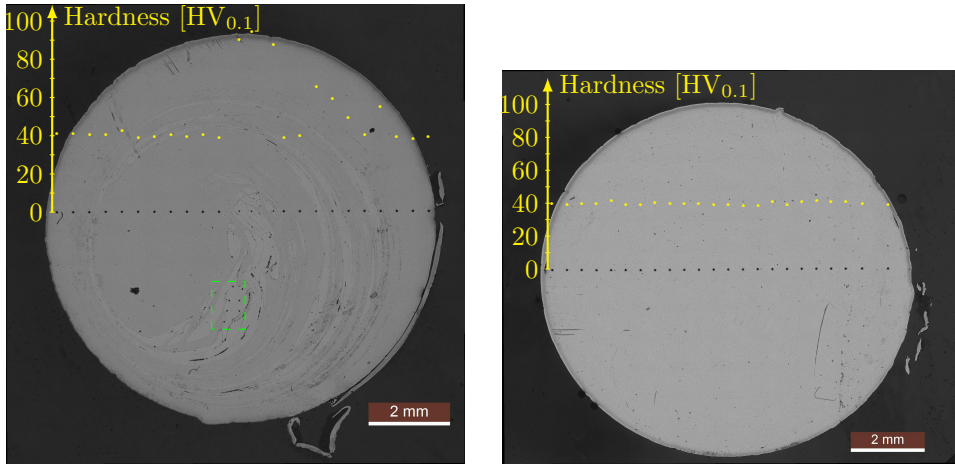
(a) 4043+5183TiC wire.

(b) 4043 wire.

Figure 97: Microhardness indents in transversal cross-section samples of the SF screw extruded wires. The peaks in hardness in (a) indicate the position of the 5183TiC phase, which is slightly brighter than the 4043 phase. The indents seen within the dashed, green rectangle in (a) were used to determine the hardness of the 5183TiC phase.

The estimated microhardness vaues of the 5183TiC and 4043 phases in the 4043+5183TiC wire and 4043 wire, are presented in Table 14.

Material	Microhardness [$HV_{0.1}$]	Standard devation [$HV_{0.1}$]
5183-TiC (in 5183TiC+4043)	91.4	1.5
4043 (in 5183TiC+4043)	40.2	1.1
4043	39.8	0.9

Table 14: Microhardness measurements of 4043 and 4043+5183TiC SF screw extruded wires.

An EDS-map of another transversal cross-section 4043+5183TiC sample, showing the emitted Mg-signals in yellow, is included in Figure 98. The image is taken of a central "swirl" of the 5183TiC material in the wire, similar to the central area in the wire shown in Figure 97a.
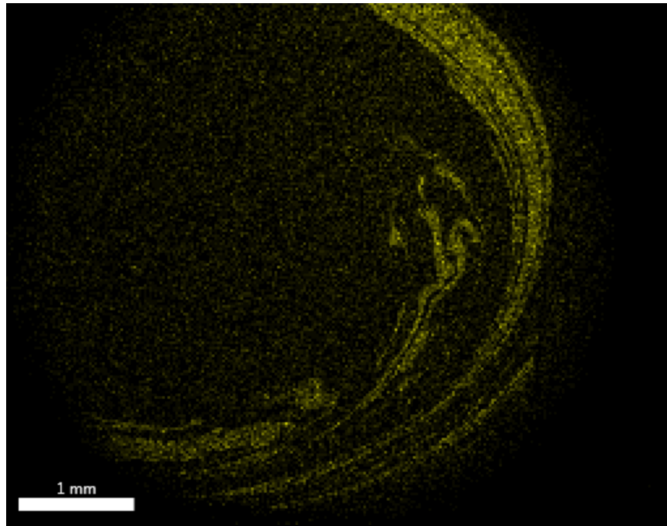
Figure 98: Mg signals from transversal cross sectional plane of 4043+5138TiC wire, retrieved using EDS.

Figure 98 illustrates the spiralling flow of the "new" 5183TiC material added to the screw extruder, as no (yellow) Mg signals are emitted from the "old" 4043 material. The spiral flow is a result of the single flight screw geometry. These results are coinciding with the findings by Widerøe and Welo [65].

D Layered oxide structure in early parts of 5183TiC wire

A wire section 30 cm from the wire beginning, hereon referred to as the early section, is investigated in this section.

An image of the early transversal cross section of the 5183TiC wire is shown in Figure 99a, while a similar image of the cross-section later in the wire is shown in Figure 99b.

(a) Early section.

(b) Late section.
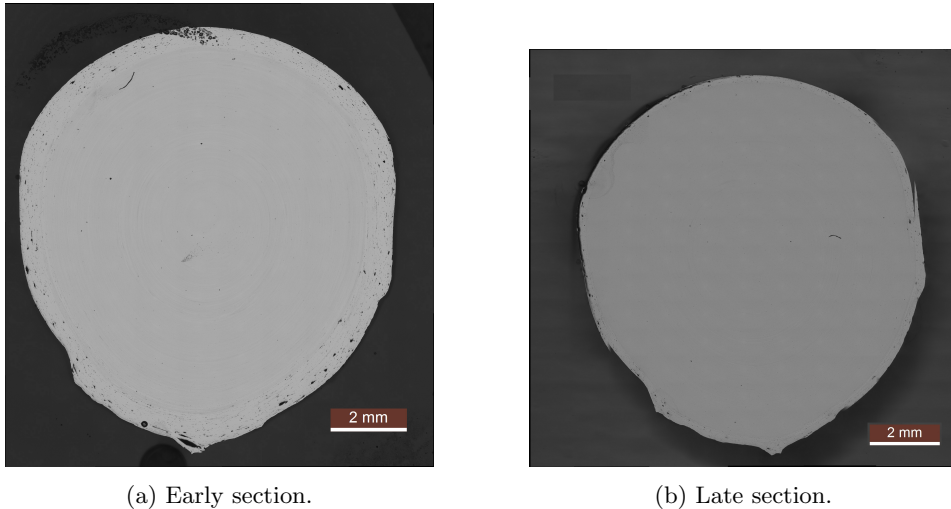
Figure 99: Optical microscopy images of the 5183TiC wire at 10X magnification.

From Figure 99, pores may be seen in the surface of the wires, all around its circumference, though to a larger extent in the early section shown in Figure 99a.

The 5183TiC wire (and all other wires) were deformed to an elliptical-like shape and not circular due to the damages in the extruder die (see Figure 36). The "bottom" of the wire, which is deformed the most, is in the bottom in the picture.

An optical image of the surface in longitudinal cross section of the early section of the 5183TiC wire is included in Figure 100.
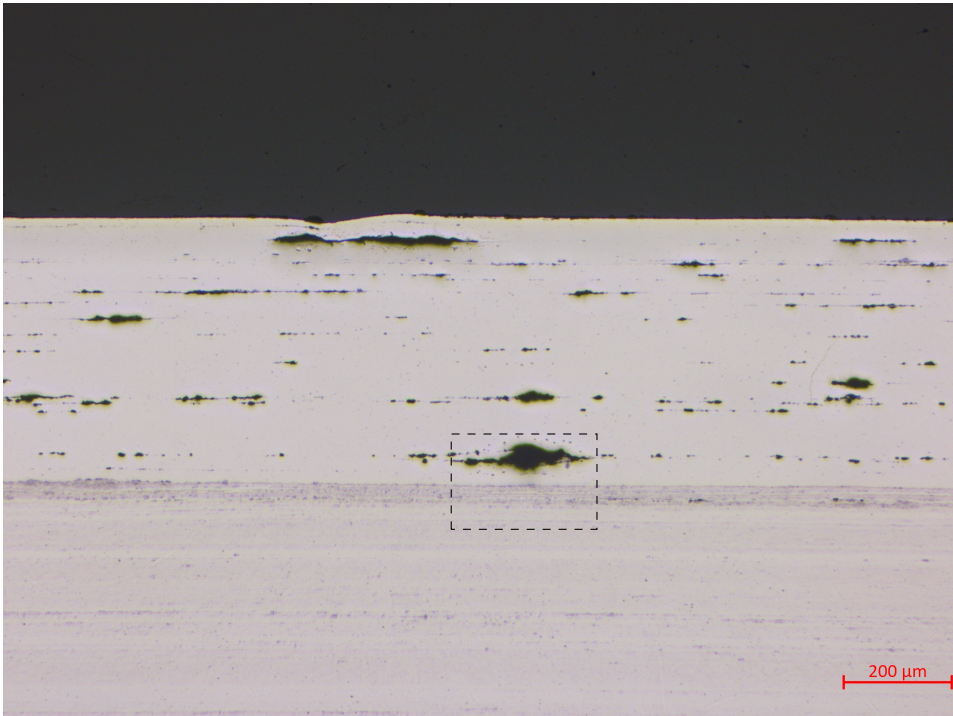
Figure 100: Microscopy image of a longitudinal cross section sample of the 5183TiC wire, taken from the part of the wire that was extruded first. An anisotropic layer-structure is clearly visible.

From Figure 100 above, it is apparent that there is a layer structure near the surface of the 5183TiC wire. To further investigate the interface between these layers, SEM was used to image the area inside the inserted box in Figure 100. The SEM image is presented in Figure 101. The image is mirrored in the SEM, compared to the optical image, as indicated by the different shape of the large crack.
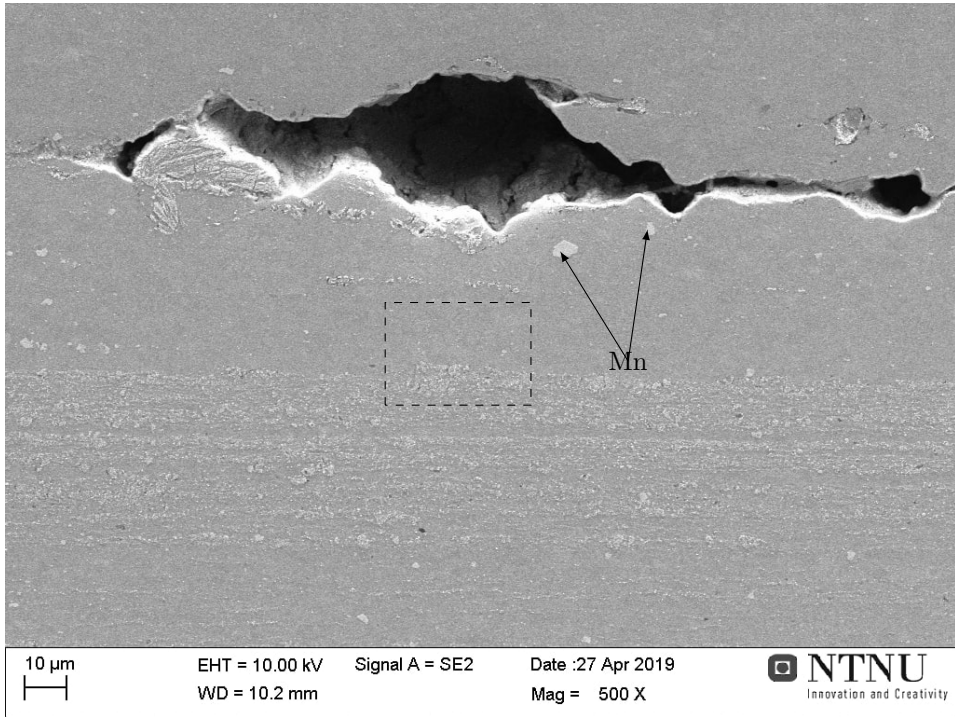
Figure 101: Secondary electron image of pore and layered-structure in the longitudinal cross section of the 5183TiC wire.

A secondary electron image of the area in the inserted box in Figure 101 is imaged at higher magnification in Figure 102a. Results from EDS analysis of the same area are included in Figure 102b – Figure 102e.
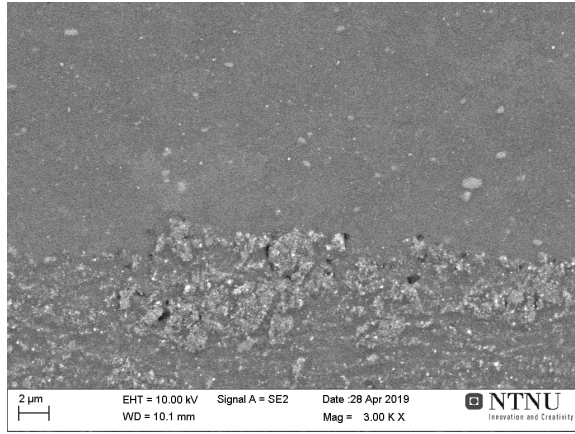
(a) Secondary electron image of pore and layered-structure in the longitudinal cross section of the 5183TiC wire.
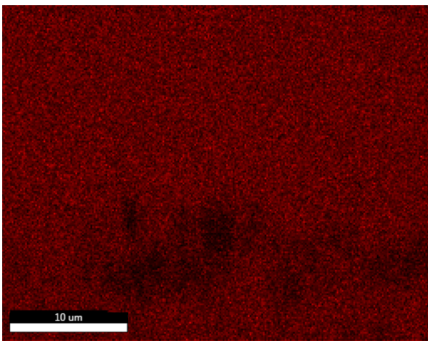
(b) Al EDS signals.
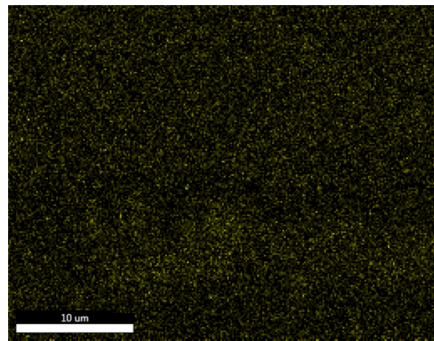
(c) Mg EDS signals.
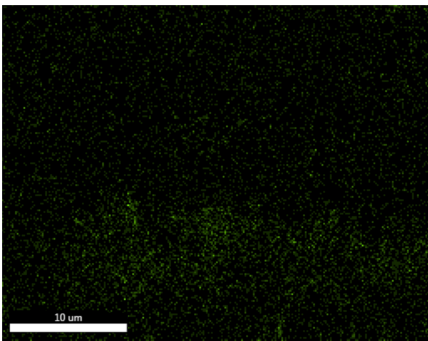
(d) O EDS signals.
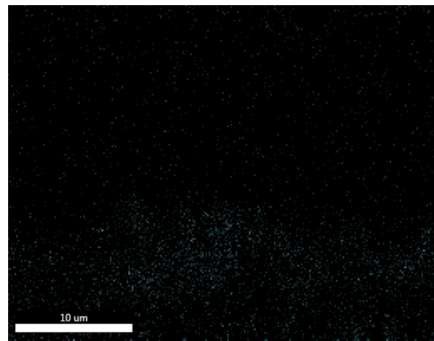
(e) Ti EDS signals.

Figure 102: SEM and EDS analysis of layer structure at 3000 X in the transversal cross-section sample of the 5183TiC wire (beginning of the wire).

The O EDS-signals in Figure 102d indicate that the grey particles in the bottom "layer" might be oxides. Most likely the oxides here are MgO, due to the weak Al signals seen in Figure 102b in the lower area compared with the stronger Mg signals, seen in Figure 102c. Also, the characteristic Ti x-ray signals (Figure 102e) seem to agglomerate in the lower layer.

An optical image from the section further back in the extruder wire in included in Figure 103.
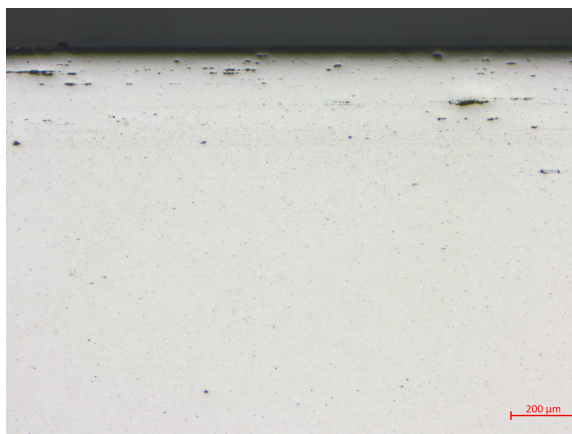
Figure 103: Microscopy image of the later section of the 5183TiC wire.

A distinct oxide-"layer" structure, as seen in the earlier section (Figure 100), was not observed clearly for the later section in Figure 103 above. This indicates that the agglomeration of oxides in a layer structure is a "start-up" issue, which may be related to insufficient mixing.

E   Identification of phases in TiC reinforced wires

The EDS spectra used to identify the phases observed in the screw extruded wires wires are presented in the following subsections, along with arrows or symbols indicating the EDS scanning-position in the SEM images. First the investigation of 5183TiC wire is presented, then the 5183TiC-CG, then 5183, then 5183-CG. Numbers are assigned to the phases/particles visible at low magnification, while letters (or chemical formulas) are used for the ones not visible until larger magnification was applied. All arrow, symbols and numbers are coloured as according to which phase it was discovered to be. The colour designation is shown in Table 15.

Table 15: Color designation of symbols/arrows used in EDS analysis.

Phase	Colour
Mn	Yellow
MgO	Orange
TiC	Black
SiO_2	Blue

SiO_2 was only observed in the 5183TiC-CG wire.

E.1 5183TiC wire

In this subsection, the EDS investigation of the longitudinal cross-section sample of the 5183TiC wire is included. This sample was vibration polished in a destilled water suspension to sucessfully remove the SiO_2 residue from the previous vibrational polishing in SiO_2-suspension. Otherwise, the sample preparation procedure, see subsubsection 3.2.2, was identical to the other wire samples.

The SEM image of the longitudinal cross-section of the 5183TiC wire, previously shown in Figure 60, is presented again in Figure 104, this time with numbers designating the different particles investigated using EDS.
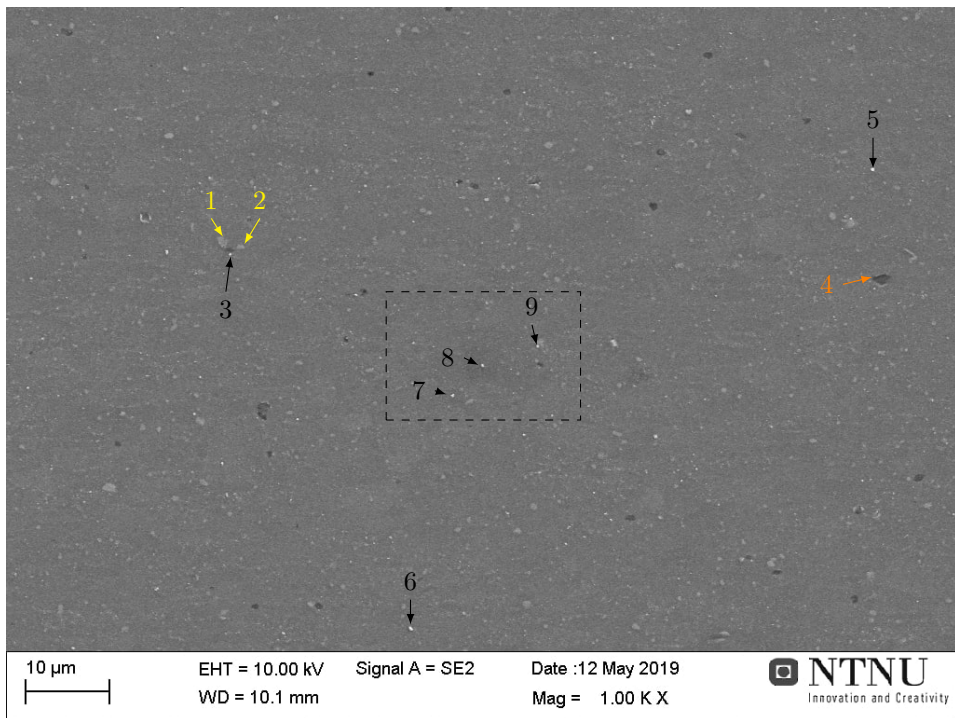
Figure 104: Matrix in longitudinal cross-section sample of 5183TiC wire, with numbered arrows pointing to the particles and phases investigated using EDS.

The area within the dashed box in Figure 104 is imaged at higher magnification in Figure 105.
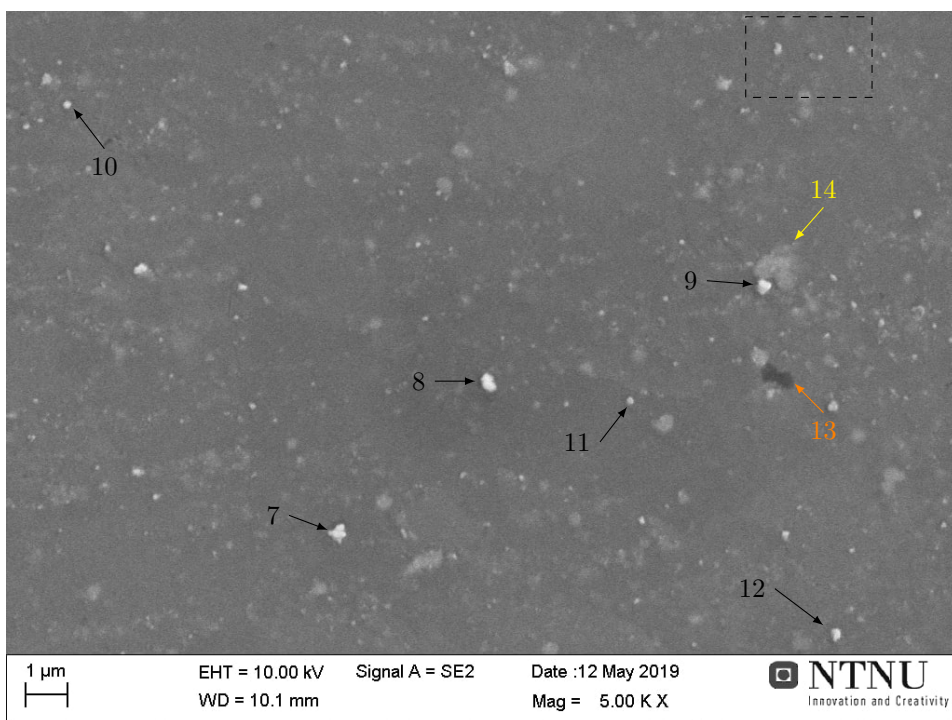
Figure 105: Matrix in longitudinal cross-section sample of 5183TiC wire, with numbered arrows pointing to the particles and phases investigated using EDS.

The area within the dashed box in Figure 105 is imaged at higher magnification in Figure 106.
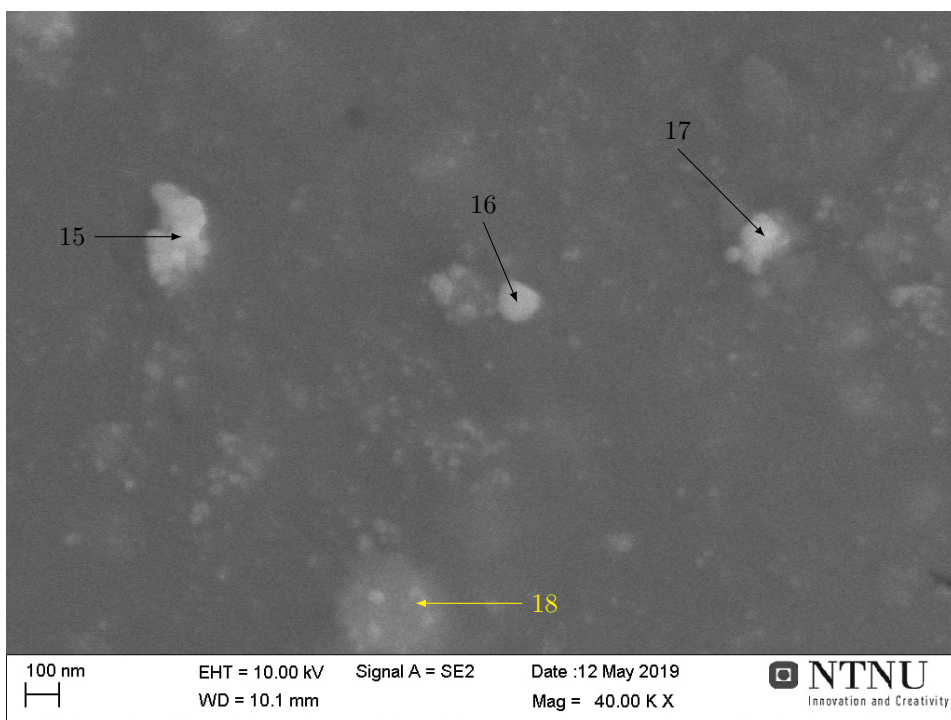
Figure 106: Matrix in longitudinal cross-section sample of 5183TiC wire, with numbered arrows pointing to the particles and phases investigated using EDS. The corresponding EDS spectra to each particle is shown in Figure 107.

The EDS spectra from points 15 to 18 in Figure 106 are included in ?? below.
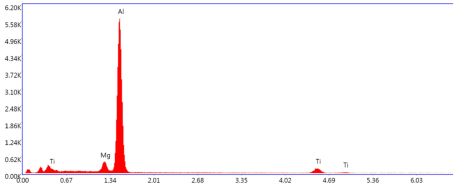
(a) EDS spectrum from spot 15, TiC cluster.
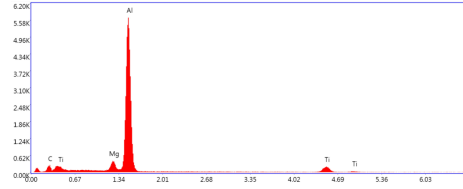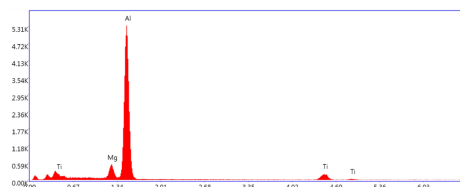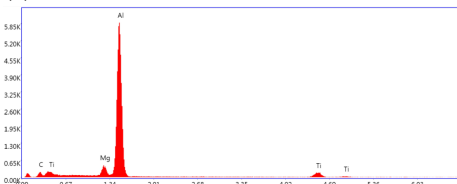

(b) EDS spectrum from spot 16, TiC cluster.
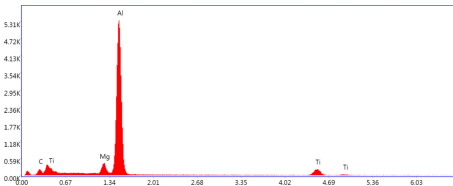
(c) EDS spectrum from spot 17, TiC cluster.
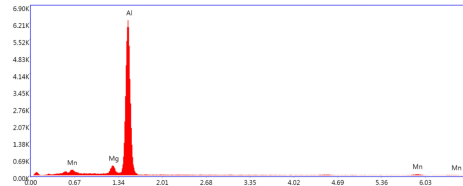
(d) EDS spectrum from spot 18, subsurface Mn phase.
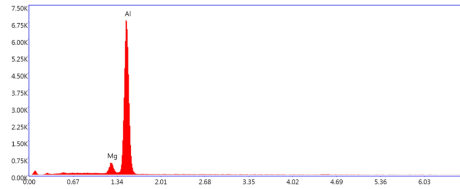
(e) EDS spectrum from matrix.

Figure 107: SEM image and EDS spectra of spots 15–18 in Figure 105, as well as a spectrum from the matrix.

High magnification images of particles/phases 1–14, with corresponding EDS spectra and measurement points, are included in the following figures (Figure 108 to Figure 118).

(a) Secondary SEM image.

(b) EDS spectrum from spot 1, Mn phase.

(c) EDS spectrum from spot 2, Mn phase.
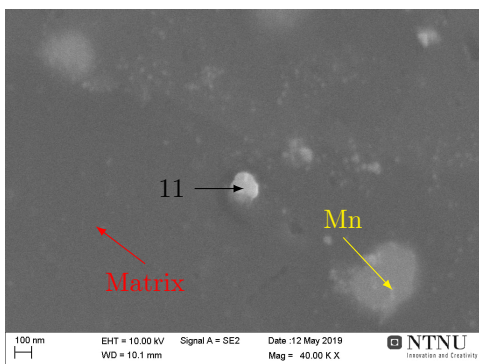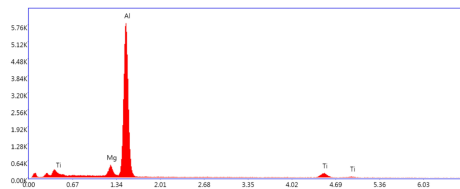
(d) EDS spectrum from spot 3, small TiC cluster.

(e) EDS spectrum from dark MgO phase.

(f) EDS spectrum from matrix.
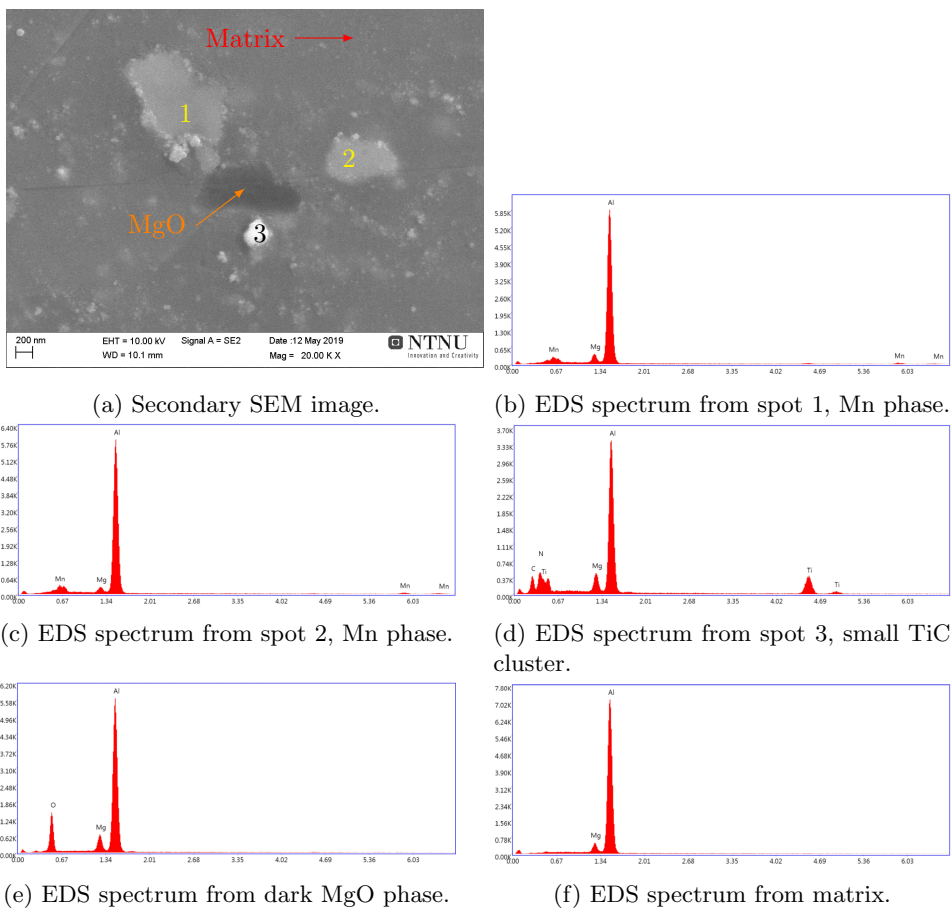
Figure 108: SEM image and EDS spectra of Mn phases and TiC particle, spots 1–3 in Figure 104. Spectra showing the signals from the matrix and the dark MgO phase in the middle of image (a) are also included.
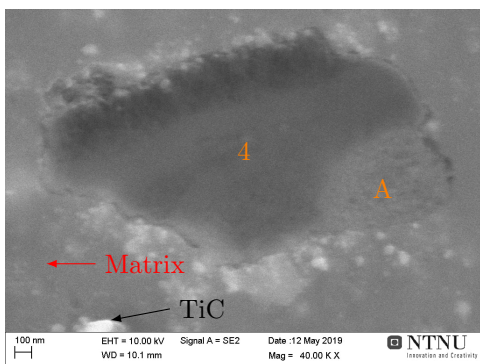
(a) Secondary SEM image.
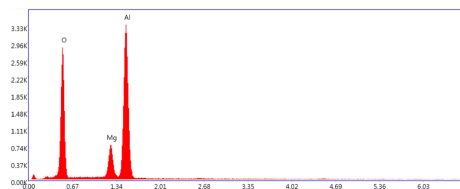
(b) EDS spectrum from spot 4, MgO phase (perhaps also containing some Al_2O_3, due to the higher Al and O content, compared with point 4).

(c) EDS spectrum from spot A, also MgO phase, with a higher content of Mg.
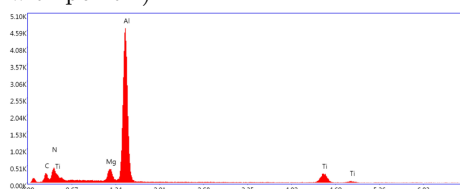
(d) EDS spectra from TiC particle.
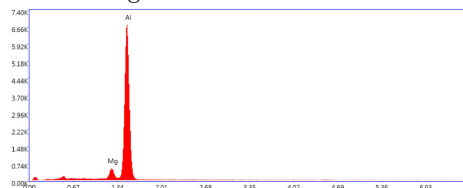
(e) EDS spectra from matrix.

Figure 109: SEM image and EDS spectra of MgO, spot 4 in Figure 104. Spectra showing the signals from a TiC cluster and the matrix is also included.
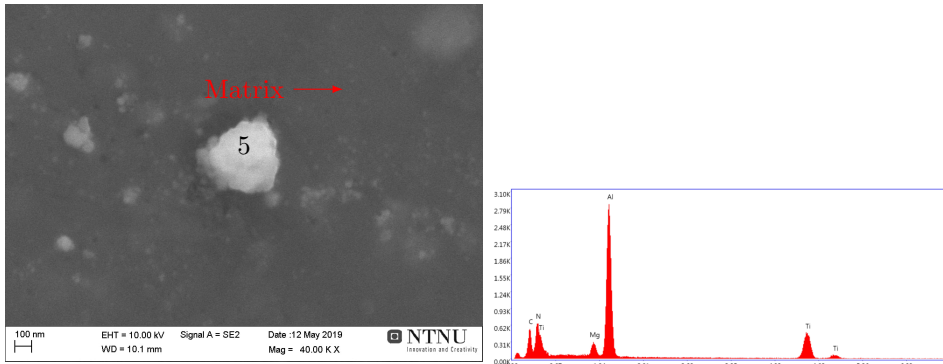
(a) Secondary SEM image.

(b) EDS spectrum from spot 5, TiC cluster.
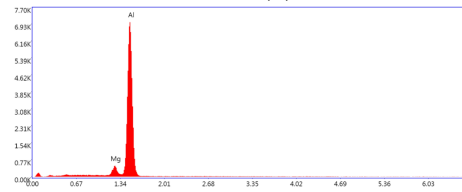
(c) EDS spectra from matrix.
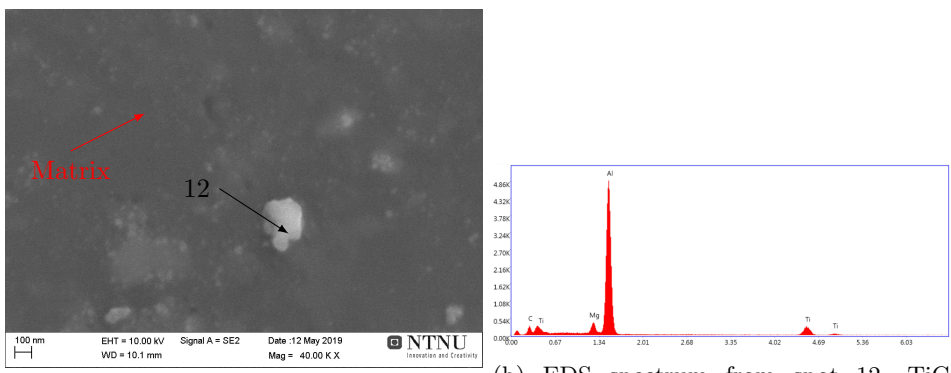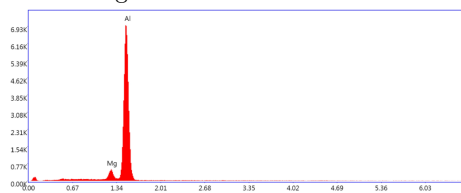
Figure 110: SEM image and EDS spectrum of spot 5 in Figure 104.
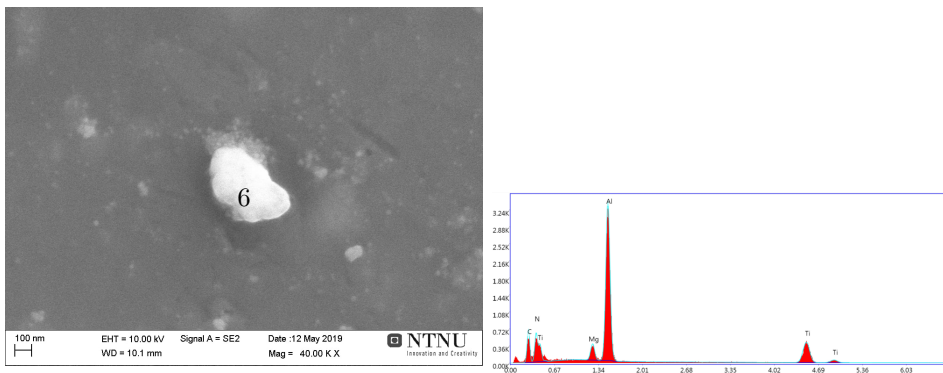
(a) Secondary SEM image.

(b) EDS spectrum from spot 6, TiC cluster.

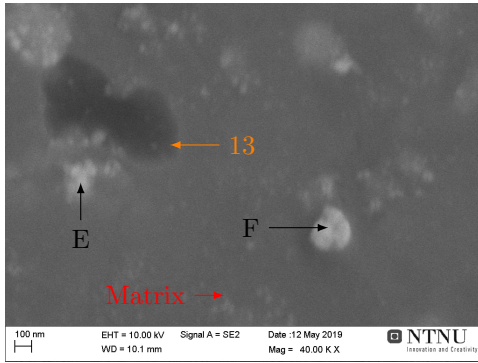Figure 111: SEM image and EDS spectrum of spot 6 in Figure 104.
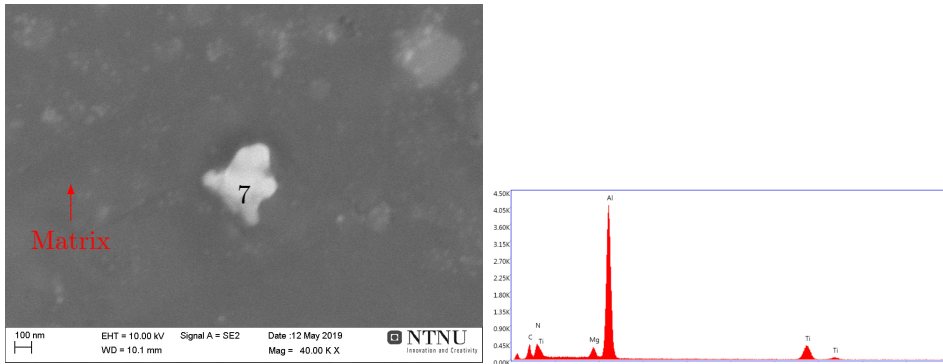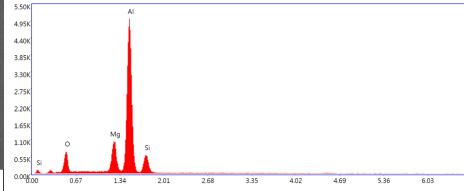
(a) Secondary SEM image.

(b) EDS spectrum from spot 7, TiC cluster.
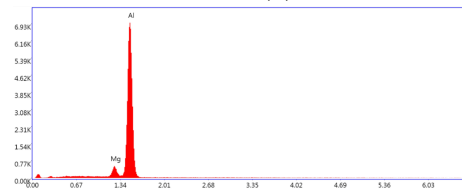
(c) EDS spectra from matrix.

Figure 112: SEM image and EDS spectrum of spot 7 in Figure 104 and Figure 105.
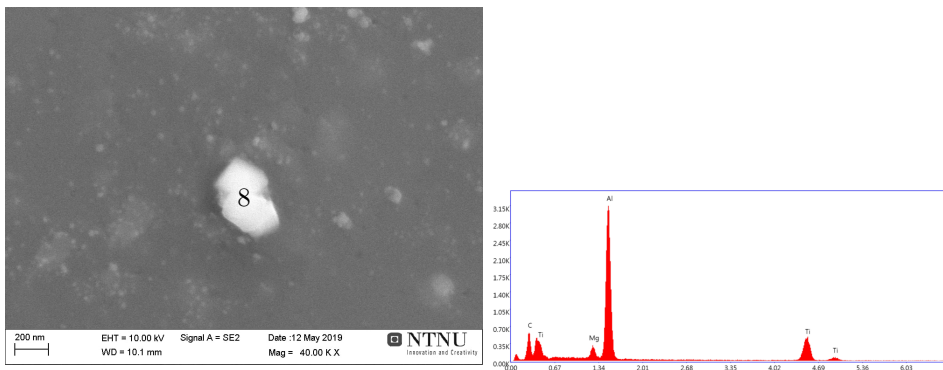
(a) Secondary SEM image.

(b) EDS spectrum from spot 8, TiC cluster.

Figure 113: SEM image and EDS spectrum of spot 8 in Figure 104 and Figure 105.

(a) Secondary SEM image.

(b) EDS spectrum from spot 9, TiC cluster.

(c) EDS spectrum from spot 14, Mn phase.

(d) EDS spectra of small TiC cluster.

(e) EDS spectra from matrix.
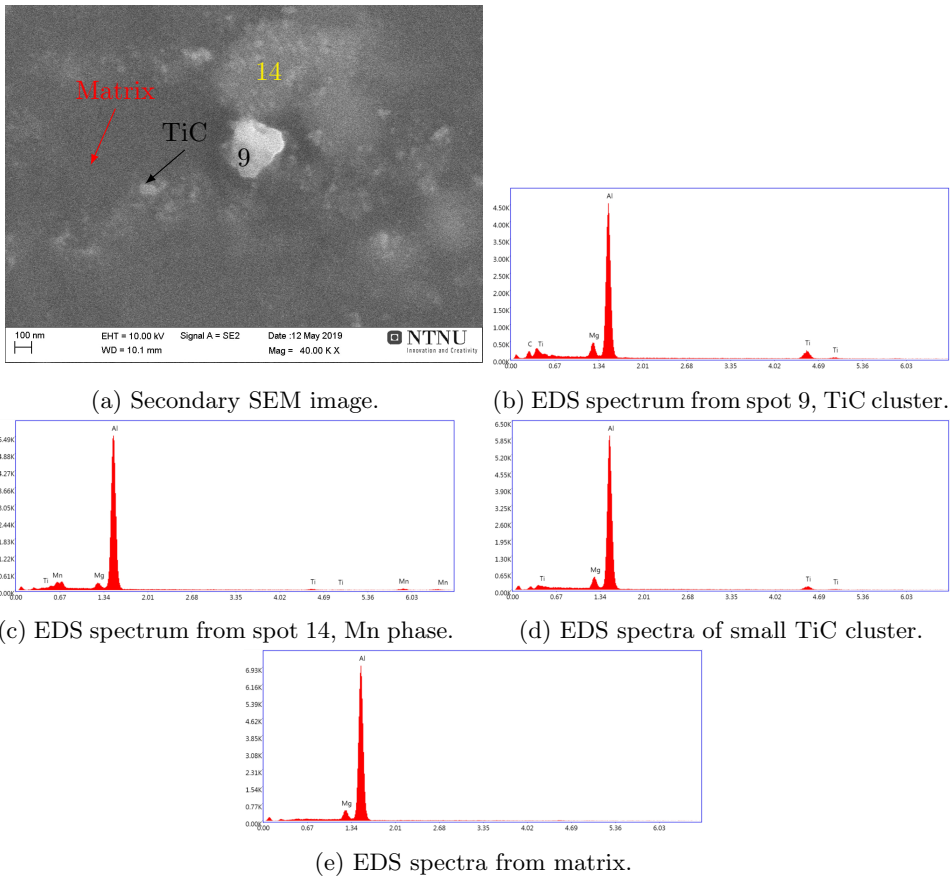
Figure 114: SEM image and EDS spectra of spots 9 and 14 in Figure 104 and Figure 105. Spectra from what seems to be a single TiC particle and the matrix are also included.
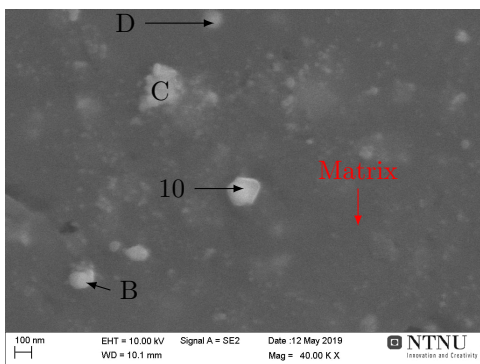
(a) Secondary SEM image.
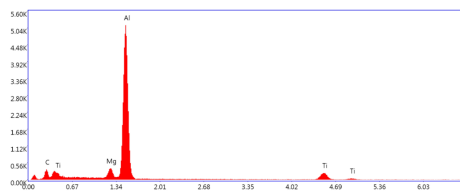
(b) EDS spectrum from spot 10, TiC cluster.
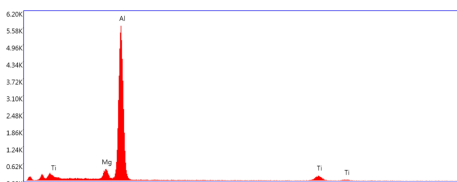
(c) EDS spectrum from spot B, TiC cluster.
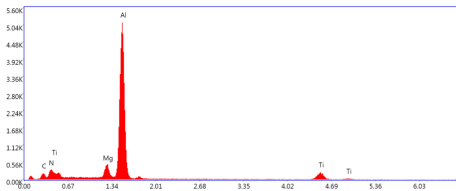
(d) EDS spectrum from spot C, TiC cluster.

(e) EDS spectrum from spot D, TiC cluster.

(f) EDS spectra from matrix.

Figure 115: SEM image and EDS spectrum of spot 10 in Figure 104 and Figure 105. Spectra from the TiC particles in the vicinity and the matrix are also included.

(a) Secondary SEM image.

(b) EDS spectrum from spot 11, TiC cluster.
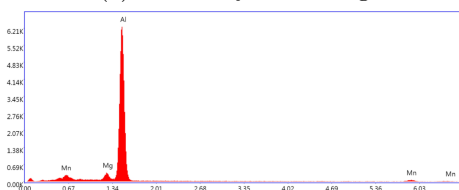
(c) EDS spectra from the Mn phase.
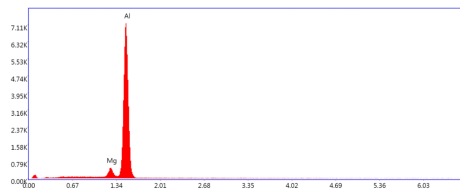
(d) EDS spectra from matrix.

Figure 116: SEM image and EDS spectrum of spot 11 in Figure 104 and Figure 105. Spectra from an Mn phase in the vicinity and the matrix are also included.

(a) Secondary SEM image.

(b) EDS spectrum from spot 12, TiC cluster.

(c) EDS spectra from matrix.

Figure 117: SEM image and EDS spectrum of spot 12 in Figure 104 and Figure 105. An EDS-spectrum from the matrix is also included.

(a) Secondary SEM image.

(b) EDS spectrum from spot 13, MgO phase.

(c) EDS spectrum from spot E.
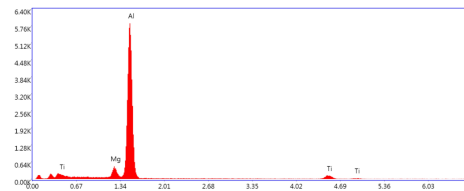
(d) EDS spectrum from spot F.
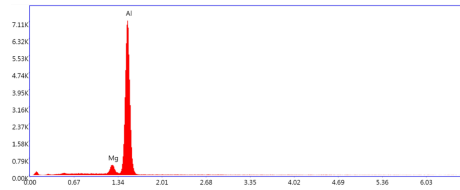
(e) EDS spectra from matrix.

Figure 118: SEM image and EDS spectra of particles/phases around spot 13 in Figure 104 and Figure 105. The spectra from TiC-clusters in the vicinity and the matrix are also included.

E.2 5183TiC-CG wire

The EDS spectra used to identify the different phases in the 5183TiC-CG wire samples are included in this section. This wire was not vibration polished in destilled water, hence some SiO_2 residue is present. The attempts to remove the SiO_2 particles from this wire resulted in copper oxide (CuO) cluster covering the sample surface, most likely occurring due to contamination of the vibrational polishing pad by Cu-rich tap water (not used intentionally, but some may have been transferred to the vibration pad by accident).

A secondary SEM image of the transversal cross-section of the 5183TiC-CG wire, already shown in Figure 64, is shown again in Figure 119 below. The numbers used to designate the different particles/phases are now reset. The colour designation still follows Table 15.
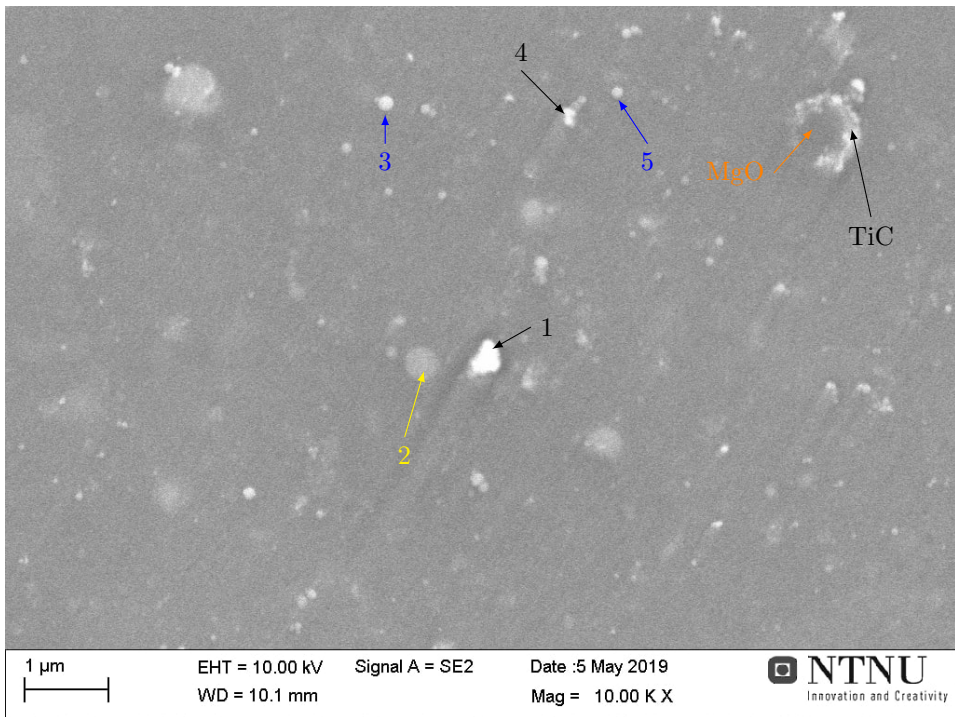

Figure 119: Matrix of transversal cross-section sample of wire 5183TiC-CG, with numbers pointing to particles/phases investigated using EDS.

The area around the MgO phase in the upper, right corner of Figure 119 (surrounded by bright TiC particles) is investigated in Figure 65a in section **??**. The EDS spectra, and high magnification images of the numbered spots in Figure 119, are shown in the following figures.
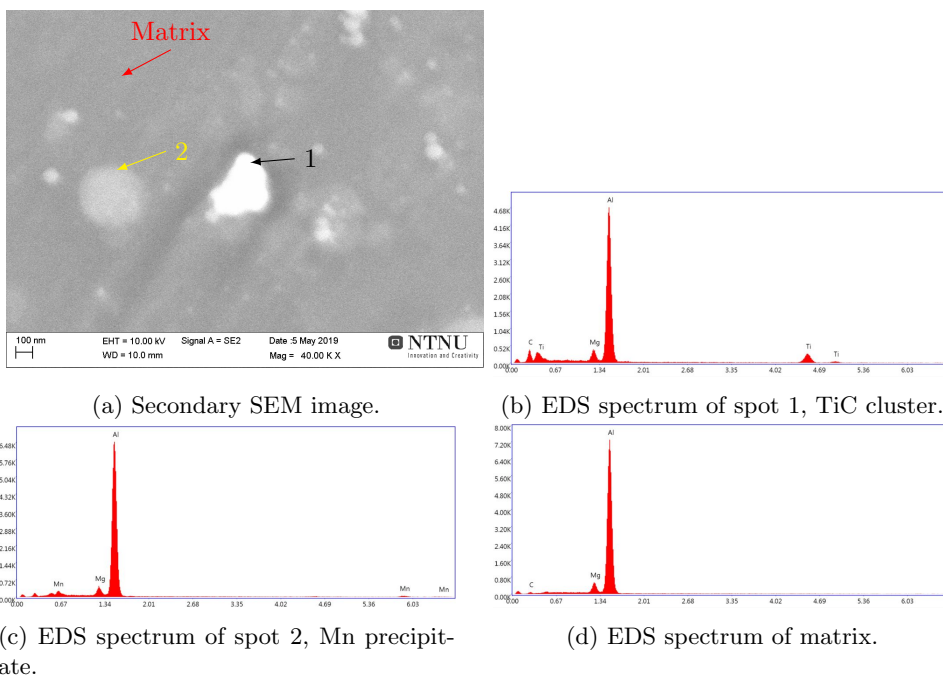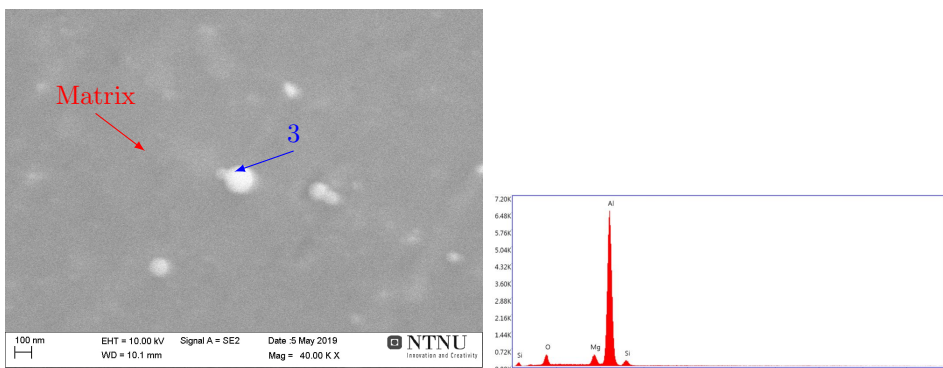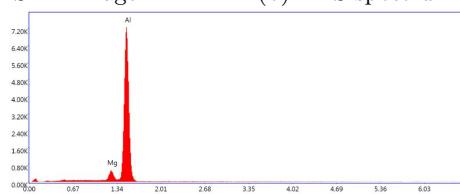

(a) Secondary SEM image.

(b) EDS spectrum of spot 1, TiC cluster.

(c) EDS spectrum of spot 2, Mn precipitate.

(d) EDS spectrum of matrix.

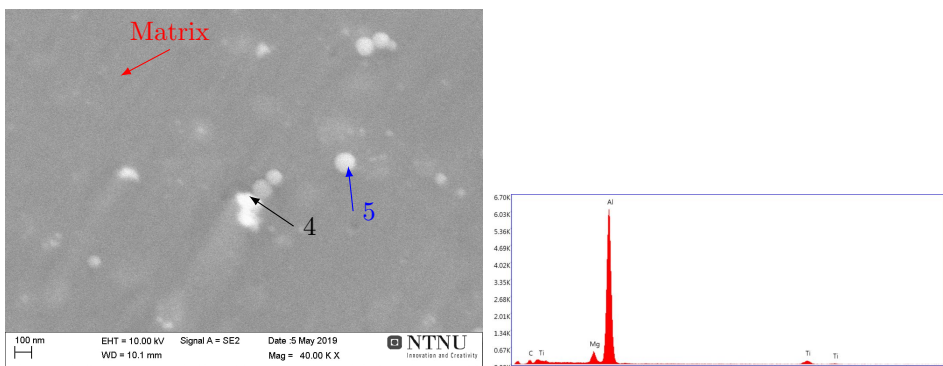Figure 120: SEM and EDS investigation of spot 1 and 2 in Figure 119, and surrounding matrix.

(a) Secondary SEM image.

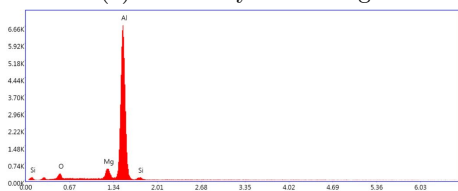(b) EDS spectrum of spot 3, SiO_2 particle.

(c) EDS spectrum of matrix.

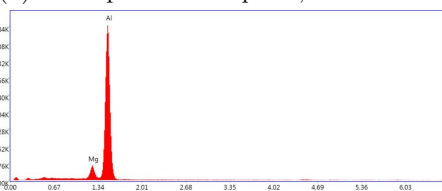Figure 121: SEM and EDS investigation of spot 3 in Figure 119, and surrounding matrix.

(a) Secondary SEM image.

(b) EDS spectrum of spot 4, TiC cluster.

(c) EDS spectrum of spot 5, SiO$_2$ particle.

(d) EDS spectrum of matrix.

Figure 122: SEM and EDS investigation of spot 4 and 5 in Figure 119, and surrounding matrix.